AIAA Graduate Team Missile Systems Design Competition

Team HFB-WEB

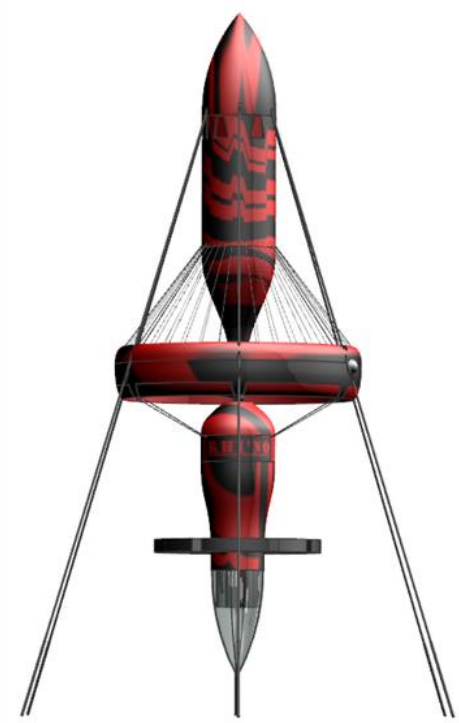

Jack Barkei
AIAA # 985213

Robert Bowes
AIAA # 985210

Christopher Eavenson
AIAA # 998650

Samantha Friess
AIAA # 985211

Brian Von Holtz
AIAA # 998642

Alex Welicky
AIAA # 920668

Faculty Advisor: Dr. Ronald Barrett

AIAA # 022393

THE UNIVERSITY OF KANSAS

Department of Aerospace Engineering

Acknowledgements

We would like to thank Brody Gatza for his assistance and contributions to this project.

Table of Contents **Page #**

List of Figures iii

List of Tables vi

List of Symbols vii

1. Mission Specification and Profile 1

2. Historical Review and Competition in the Market 2

2.1 Jamming Devices 2

2.2 Launched Projectiles 3

2.3 Airborne Platforms 5

3. Introduction of Design 6

4. Initial Design Considerations 8

4.1 Design Optimization Function 8

4.2 Configuration Down-Selection 9

4.3 Hovering Missile Engagement System Down-Selection 11

5. Systems Design 14

5.1 Stability and Control Sensors 14

5.2 Target Drone Tracking Sensors 14

5.2.1 Acoustic Vector Sensors 15

5.2.2 Electro-Optical Sensors 17

5.3 Ground Station 17

6. Powerplant Design 17

6.1 Propeller Sizing 18

6.2 Battery and Motor Sizing 20

6.3 Doghouse Plot 23

6.4 Noise Compliance 24

7. Structural Design 25

7.1 Rotor Guard Design 25

7.2 Empennage Design 25

7.3 Titanium Armor Sizing 26

7.4 External Structure 27

7.5 Internal Structure 27

7.6 V-n Diagrams 28

7.7 Launch and Recovery System Design 29

8. Design Integration 31

8.1 Layout of Major Systems 31

8.2 Redundancy 33

8.3 Wiring Block Diagram 33

8.4 Electric Load Summaries 34

8.5 General List of Components 36

8.6 Weight and Balance 37

8.7 Center of Gravity Determination 39

8.8 Exploded View 42

8.9 Color Schemes 44

8.10 Packing 45

8.11 Alternate Payload Viability 46

8.11.1 Payload Range-Altitude Diagram 46

8.11.2 Range Testing of Custom Shotgun Shell Solution 47

8.11.3 Pneumatic Net Gun Weight Estimation 48

9. Class I Stability and Control Analysis 48

10. Structural Analysis.....50

11. Aerodynamic Analysis.....52

11.1 Drag Polar Analysis 52

11.2 CFD Analysis.....54

11.2.1 Geometry 54

11.2.2 Mesh Characteristics.....54

11.2.3 Physics Models and Conditions ...55

11.2.4 Verification 56

11.2.5 Results and Analysis 57

12. Antenna Analysis.....60

12.1 Physical Model Creation.....60

12.2 Anecdotic Chamber Experimental Set-up61

12.3 HFSS Model 62

13. Performance Analysis 66

13.1 Performance Overmatch Chart.....67

13.2 Engagement Renderings 68

14. Economics Model 69

15. Compliance Matrix 73

16. HFB-WEB Group Member Contact Information.....73

17. References.....74

List of Figures

Figure 1.1: Mission Profile [2, 3].....1

Figure 2.1: DroneShield Dronegun..... 2

Figure 2.2: Paladyne E1000MP Jamming Device [6] 2

Figure 2.3 Jamming Device CONOPS 3

Figure 2.4 Raytheon FIM-92 Stinger Missile [9] 3

Figure 2.5: SkyWall Net Mechanism [10]..... 3

Figure 2.6: SkyWall Launcher [10] 3

Figure 2.7: SAVAGE Kinetic Missile [11] 4

Figure 2.8: SAVAGE Launcher [11]..... 4

Figure 2.9 Operation of Anti-UAV 50-mm Shell [13] 4

Figure 2.10: Shoulder or Vehicle Launcher CONOPS 4

Figure 2.11: Delft Dynamics 5

Figure 2.12: Airborne Platform CONOPS..... 5

Figure 3.1: RHI*NO Design Features Overview..... 7

Figure 4.1: SkyNet Shotgun Net Shells [17] 11

Figure 4.2: Shotgun Net Capture [3] 11

Figure 4.3: Pneumatic Gun Net Capture [3]..... 11

Figure 4.4: Kevlar Strand Rotor Entanglement [3] 12

Figure 4.5: Piercing Horn Design [3] 13

Figure 4.6: Hardened Shell Design for Kinetic Kill [3] 13

Figure 5.1: AVS Onboard Small UAV [21] 15

Figure 5.2: AVS Wires Across Airflow Channel [21] 15

Figure 5.3: AVS Instrument Scale [22] 15

Figure 5.4: Laminar Flow Sensor Housing [24] 16

Figure 5.5 : AVS Target Tracking During Approach [26] 16
Figure 5.6: AVS Target Tracking During Interception Maneuver [26] 16
Figure 5.7 Wolfwhoop F4SD FC Integrated OSD [27] 17
Figure 5.8: Dedrone RF-160 [28] 17
Figure 5.9: Orqa FPV.One Headset [29] 17
Figure 6.1: Propeller Actuation System 19
Figure 6.2: Dash Configuration Propeller AOA Created with BEMT Code 20
Figure 6.3: Climb Configuration Propeller AOA Created with BEMT Code 20
Figure 6.4 Experimentally Gathered Battery Sizing Data [41] 21
Figure 6.5: Engine Sizing 38% and 55% Takeoff Weight for 8, 12, and 16 lb HMSs 22
Figure 6.6: 12 lb HMS Doghouse Plot 23
Figure 6.7: XQ-138 Experimentally Collected Noise Levels [42] 24
Figure 6.8: Conventional vs MicroStator Noise [43] 24
Figure 7.1: Rotor Guard Clark Y-18 Airfoil [45] ... 25
Figure 7.2: Grid Fin [45] 25
Figure 7.3: RHI*NO Longitudinal X Plot 26
Figure 7.4: Hovering Missile Three-View 27
Figure 7.5: Structural Layout Skeleton 28
Figure 7.6: Ramming Load Pathways 28
Figure 7.7: RHI*NO V-n Diagrams 29
Figure 7.8: Spring-Loaded Telescopic Legs 30
Figure 7.9: Takeoff from Sandy Terrain 30
Figure 7.10: Take-off from Rocky Terrain 30
Figure 7.11: Emergency Parachute Deployment [47] 31
Figure 8.1 Fuselage Structural Layout 31
Figure 8.2: Removable Sensor Cage Empty 32
Figure 8.3: Removable Sensor Cage Filled 32
Figure 8.4 Wiring System Layout 33
Figure 8.5: RHI*NO Wiring Block Diagram 34
Figure 8.6 Internal Layout 39
Figure 8.7: Nose Layout 40
Figure 8.8: 12 lb RHI*NO CG Locations 40
Figure 8.9: C.G. Excursion Plot 40
Figure 8.10: Exploded View and Material Break Down 43
Figure 8.11 Hovering Missile Advanced CAD 44
Figure 8.12 Alternate Color Schemes (Left Side Top to Bottom: Army (Desert), Coast Guard, Air Force), (Right Side Top to Bottom: Army (Olive Drab), Navy, (Night-Operation) 44
Figure 8.13: 12 lb RHI*NO Missile Disassembled in Carrying Case 45
Figure 8.14: 12 lb RHI*NO Missile Carrying Case Size Illustration 45
Figure 8.15: Relative RHI*NO Size Perspective Graphic [2, 63, 64] 45

Figure 8.16 Payload vs Range For 8, 12, and 16 lb. Designs 46
Figure 8.17: Shotgun Testing Setup 47
Figure 8.18 Wad of Kevlar Strands Embedded Within Target 47
Figure 8.19 Burned and Frayed Kevlar Strands 47
Figure 8.20 DJI Inspire 2 [66] 48
Figure 8.21 DJI Matrice 600 Pro [67] 48
Figure 9.1: Lateral Stability Derivatives From AAA 49
Figure 9.2: Stability Derivatives From AAA 49
Figure 9.3: Control Surface Derivatives From AAA 50
Figure 10.1: Impact Force Distribution 51
Figure 11.1: Drag Polars for 12 lb. HMS 53
Figure 11.2 Solid Bodies for CFD Analysis 54
Figure 11.3: Surface and Volume Mesh 55
Figure 11.4: Surface Mesh at Landing Gear Intersection 55
Figure 11.5: Surface Mesh and Prism Layers at Ballute and Grid Fins 55
Figure 11.6: Surface Mesh and Prism Layers at Nosecone 55
Figure 11.7: Volume Mesh Around Vehicle Area .55
Figure 11.8: Total Volume Mesh 55
Figure 11.9 Physics Conditions 56
Figure 11.10 Virtual Disk Propellers 56
Figure 11.11: Wall Y+ Distribution 56
Figure 11.12: Residuals Plot 57
Figure 11.13: Absolute Pressure Distribution 57
Figure 11.14: Absolute Pressure Distribution in Area of Interest 57
Figure 11.15: Absolute Total Air Pressure 58
Figure 11.16: Air Velocity Magnitude 58
Figure 11.17: Air Velocity at Airfoil 58
Figure 11.18: Center of Pressure Location 58
Figure 11.19: NACA Inlet Geometry 59
Figure 11.20: Velocity Vectors Around Inlet Fuselage Section 59
Figure 11.21: Swirl Generated by NACA Inlets 59
Figure 11.22: Velocity Vectors Around Clark Y Airfoil 59
Figure 12.1: Physically Created Dipole For 2.4 GHz Resonance Frequency 60
Figure 12.2: RHI*NO Missile 60
Figure 12.3: Physical Mockup Design 60
Figure 12.4 AUT Integrated onto Mockup Design 60
Figure 12.5 :Modeled Sensors and Electronics with Aluminum Wrapped Foam 61
Figure 12.6: Mounted Turnigy 270KV Motor (Same as Specified for Design) 61
Figure 12.7: Electronic Calibration 61
Figure 12.8: ETS 3117 Double Horn Antenna [2]. 61
Figure 12.9 $S11$ Comparison of All Tested Conditions 62
Figure 12.10 RHI*NO Modeled In HFSS 63

Figure 12.11 Antenna Integrated on Fuselage.....63

Figure 12.12 Arm Length Effect on Resonance Frequency in HFSS with Kevlar-epoxy Material Selection.....64

Figure 12.13 $\boldsymbol{S11}$Plot for Cardboard Material 64

Figure 12.14 Electrical Radiation Plot When $\boldsymbol{\phi = 0°}$ 65

Figure 12.15 Electrical Radiation Plot When $\boldsymbol{\phi = 90°}$ 65

Figure 12.16 Realized Gain Pattern at $\boldsymbol{\phi = 90°}$ 65

Figure 12.17 Antenna Placement Reference 65

Figure 12.18 Electrical Radiation 3D Polar Plot View 1.....66

Figure 12.19 Realized Gain Radiation 3D Polar Plot 66

Figure 13.1: RHI*NO Flight Envelope Performance Overmatch Chart 67

Figure 13.2: RHI*NO Interdiction with DJI Phantom Before (Left) and After Collision (Right) [71].....68

Figure 13.3: RHI*NO Interdiction with DJI Phantom Shotgun Engagement [71].....68

Figure 13.4: RHI*NO Interdiction with MQ-Predator Shotgun Engagement [72].....68

Figure 13.5: XQ-138 Landing [73] 69

Figure 13.6: XQ-138 Flight Video [74] 69

Figure 14.1 Production Cost Projections.....69

Figure 14.2 Cost Per Interception of Various Missile Systems 70

List of Tables

Table 1.1: Mission Specification Given by RFP [1] 1

Table 4.1: System Design and Engagement Method Down-Selection Via the Optimization Function Defined in Chapter 3.1..... 10

Table 5.1: Target Tracking Sensors..... 14

Table 5.2: AVS Drone Identification Accuracy [23] 16

Table 6.1: Salient Characteristics Relationship to Rotor Diameter [31, 32]..... 18

Table 6.2 Salient Propeller Design Characteristics 20

Table 6.3 Electric Motors [34-39] 21

Table 7.1: Titanium Armor Weight 26

Table 7.2: HMS Salient Characteristics..... 28

Table 8.1 Total Energy Load Requirements 35

Table 8.2 Battery Key Characteristics 35

Table 8.3: RHI*NO Electrical Power Summary for Battery Sizing 35

Table 8.4: RHI*NO Electrical Energy Summary for Battery Sizing 36

Table 8.5: General Component List Description [51-60]..... 36

Table 8.6 Weight Fraction Calculations 38

Table 8.7: 12 lb RHI*NO CG Component Breakdown 41

Table 8.8 Range Testing Summary..... 48

Table 9.1: L/D Comparison 49

Table 9.2: Modal Analysis of the RHI*NO 50

Table 10.1: Forward Fuselage Weight Summation 51

Table 11.1: Wetted Area Calculations Verified by CAD Model 53

Table 11.2: Base Size Variations 54

Table 12.1 Resonance Frequency and bandwidth Results for Each Tested Condition 62

Table 12.2 Resonate Frequencies and bandwidth results for HFSS Models 63

Table 14.1: RHI*NO Research and Development Costs.....72

List of Symbols

Symbol	Description	Units
a	acceleration	$\frac{ft}{s^2}$
A	Wing Aspect Ratio	(~)
b	Wingspan	ft
C	Cost	$
C_D	Coefficient of Drag	(~)
C_f	Coefficient of Friction	(~)
C_L	Coefficient of Lift	(~)
CEF	Cost Estimation Factor	(~)
d	Inner Diameter	ft
D	Diameter or Drag	ft or lbf
e	Oswald Efficiency Factor	(~)
E	Bulk Modulus	(~)
f	Parasite Area	ft^2
f	Frequency	Hz
F	Force	lbf
F	Factor	(~)
g	Gravity	$\frac{ft}{s^2}$
h	Altitude	ft
K	End Fixity Coefficient	(~)
l	Length	ft
L	Lift	lbf
m	Mass	lbm
MHR	Man Hours	hr
N	Number	(~)
O	Objective	(~)
P	Power	W
r	Radius	ft
R	Requirement	(~)
S	Wing Area	ft^2
t	Time	sec
u	True Airspeed	knots
v	Velocity	$\frac{ft}{s}$

Greek Symbol	Description	Units
α	Angle of Attack	deg
β	Angle of Side Slip	deg
η	Efficiency	(~)
θ	Angle	deg
λ	Wavelength	ft
σ	Stress	psi

Abbreviations	Description
AAA	advanced aircraft analysis

ADS-B ..... automatic dependent surveillance-broadcast

AGL ..... above ground level

AIAA ..... American Institute of Aeronautics and Astronautics

AOA..... Angle of Attack

ATHENA..... Advanced Test High-Energy Asset

AVS ..... Acoustic Vector Sensor

BEMT ..... blade element momentum theory

CAD..... computer aided drawing

CFD ..... computational fluid dynamics

CG.....center of gravity

CONOPS ..... concepts of operations

COTS ..... consumer off the shelf

CPI..... cost per interception

ESC.....electronic speed controller

EO.....electro-optical

FAA ..... Federal Aviation Administration

FCC.....Federal Communications Commission

FCS ..... flight control system

FM .....figure of merit

FPV.....first-person view

FS.....fuselage station

FWD ..... Forward

GPS..... global positioning system

HFSS..... high frequency structural simulator

HMS..... hovering missile system

IOC ..... initial operational capability

IMU.....inertial measurement unit

IR.....infrared

LE..... leading edge

LS.....launch system

MGC..... mean geometric chord

NACA .....national advisor committee for aeronautics

PEC .....perfect electric conductor

RADAR..... radio detection and ranging

RDT&E ..... research and development

RF..... radio frequency

RFP.....request for proposal

RHI*NO . ramming halo interceptor *net optional

ROC ..... rate of climb

RPM ..... revolutions per minute

SAVAGE .....Smart Anti-Vehicle Aerial Guided Engagement

SAS .....situational awareness system

TD ..... target drone

TRL ..... technology readiness level

UAS..... unmanned aerial system

UAV .....Unmanned Aerial Vehicle

VTOL .....vertical takeoff and landing

Subscripts	**Description**
a	avionics
aedr	airframe engineering and design
c	camera shield

cad.....computer aided design

cg .....center of gravity

dstr ..... development support and design

D0 ..... zero lift drag

e ..... engine

f.....fuselage

fa ..... fin actuator arm

finr ..... finance

ftar..... flight test aircraft

fus .....fuselage

gf..... grid fin

i .....inner

ih ..... incidence of horizontal

k .....kill

l ..... airfoil lift

lg ..... landing gear

l ..... roll

L.....planform lift

m .....microstator

m.....pitch

mat..... material

max ..... maximum

n .....yaw

nc.....nose cone

obs ..... observable

pror .....RDT&E Profit

P ..... power

qC..... quality control

req..... required

rg .....rotor guard

st .....static aircraft

tool ..... tooling

tot ..... total

train ..... training

tsfr .....test and simulation facilities

tw.....twist

T ..... thrust

TS ..... total system

wet.....wetted

1. Mission Specification and Profile

The mission specification requirements, outlined by the American Institute of Aeronautics and Astronautics (AIAA) design request for proposal (RFP) for the 2020-2021 Graduate Team Shoulder-Launched Anti-UAV Missile System Design Competition [1], are listed below in Table 1.1.

Table 1.1: Mission Specification Given by RFP [1]

Weight Specifications	
1 Launcher + 1 Missile	40 pounds
1 Launcher + 10 Missiles	125 pounds
Maximum personnel carrying capacity	50 pounds
Performance Specifications	
Threshold Ceiling	3000 ft AGL
Objective Ceiling	5000 ft AGL
Threshold Range	3.0 nmi
Objective Range	3.5 nmi
Maximum Launch Acceleration	2 g's
Minimum Warhead Arming Distance	200 ft
Maximum Noise within 100 ft of Launch	120 dBA
Capability Specifications	
Minimum Interdiction	10 drones per hour
Storage Length	Up to 10 years with no maintenance

The preliminary mission profile of the design flight plan is shown below in Figure 1.1.

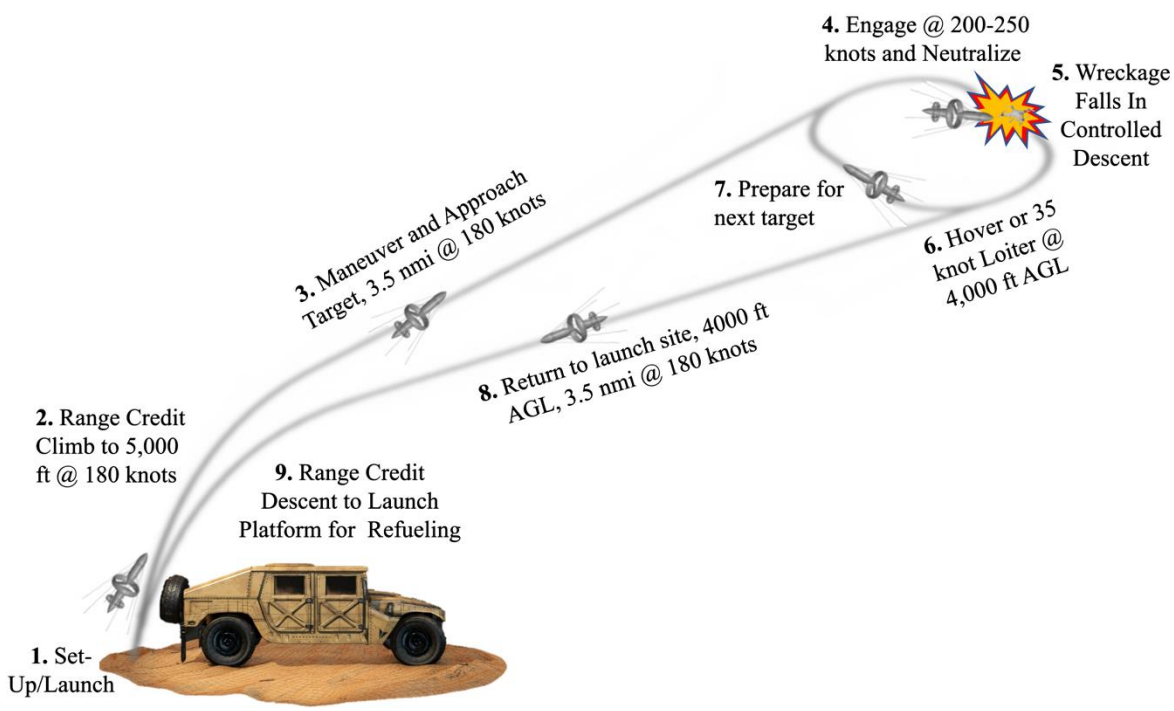

Figure 1.1: Mission Profile [2, 3]

2. Historical Review and Competition in the Market

Although Unmanned Aerial Vehicles (UAVs) have been used for combat as early as 1849, when Austrian forces tied bombs to hot air balloons and launched them over Venice [4], these vehicle types and their roles have changed greatly over time. With small civilian-operated UAVs only recently gaining popularity (and starting to cause trouble for both civilians and the military), the history of purpose-built anti-drone weapons is somewhat short.

While traditional firearms may be effective at countering some types of UAVs, this chapter will primarily investigate devices designed specifically for counter-UAV operations. Nearly all devices appropriate for countering type 1 and 2 UAVs as they are known today are currently available while others are still in development. These devices fall into three general categories: jamming devices, projectile launchers, and airborne platforms.

2.1 Jamming Devices

In many cases, the simplest and safest way to disable a UAV is to do so electronically, thereby avoiding explosives and high-energy materials. Anti-UAV jamming devices, such as the DroneShield Dronegun [5] and the Paladyne E1000MP [6], shown in Figure 2.1 and Figure 2.2 respectively, emit a jamming signal at a frequency that matches the target's communication signal. This forces the target into a controlled descent or eliminates control entirely. A concept of operations, CONOPS, diagram for devices of this type is shown in Figure 2.3. Currently available devices of this type are practical and simple to operate but require a line of sight between the operator and the target. They can interfere with nearby communications and GPS technology, limiting their availability to civilians. Many also struggle to be effective at a range greater than one kilometer.

Figure 2.1: DroneShield Dronegun Jamming Device [5]

Some large jamming devices, such as the Skyfence [7], create a stationary "wall" through which a UAV cannot pass through without losing control; this strategy is effective for area protection but is immobile. Other devices, like the Dronekiller [8] do not jam the target, but instead emit a software-defined radio signal which increases the bit error rate of onboard equipment.

Figure 2.2: Paladyne E1000MP Jamming Device [6]

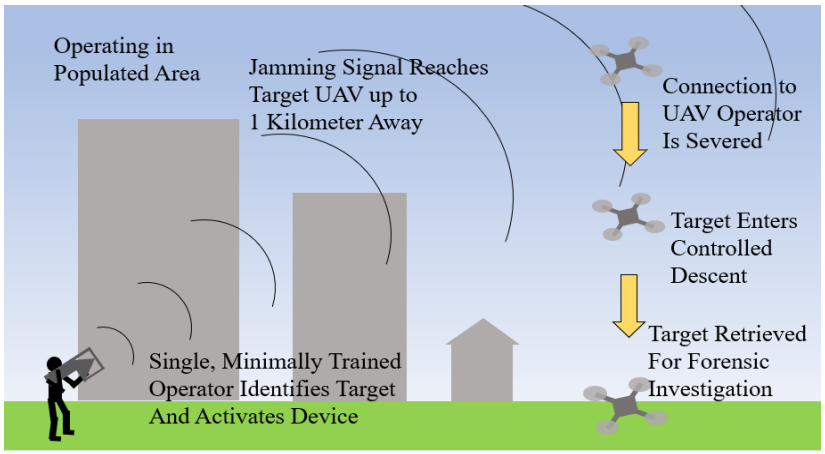

Figure 2.3 Jamming Device CONOPS

Depending on the configuration and flight path of the target, a controlled descent may not be possible, resulting its destruction and collateral damage to the surrounding area.

2.2 Launched Projectiles

More consistent with the missile design strategy, launched projectile devices enable a single soldier or vehicle to fire a projectile at a UAV target with the intent to disable or destroy it. A popular shoulder-launched missile system is the Raytheon FIM-92 Stinger: an infrared-guided anti-air missile with a 6.6-pound warhead and a range of nearly 5 kilometers [9]. Shown in Figure 2.4, the Stinger missile has been in service since 1978 and has been combat proven in conflicts around the world. Despite its reputation and versatility, it is a somewhat large system and may struggle to hit small, agile targets such as quad-copter UAVs, in part due to their low infrared signature. A less dangerous alternative to the Stinger missile is the SkyWall capture system, which fires a cannister containing a deployable net toward the target UAV. Once captured, the target is lowered to the ground with a parachute, allowing for forensic analysis [10]. Shown in Figure 2.5 and Figure 2.6, the SkyWall system offers a safe and re-usable solution here electronic jamming devices cannot be used, although at an operational range of only 0.3 kilometers.

Figure 2.4 Raytheon FIM-92 Stinger Missile [9]

Figure 2.5: SkyWall Net Mechanism [10]

Figure 2.6: SkyWall Launcher [10]

Figure 2.7: SAVAGE Kinetic Missile [11]

Another mobile launcher option is the SAVAGE missile concept, which is currently under development by SmartRounds Inc. and not yet available to consumers [11]. The SAVAGE missile system launches a 40-mm non-explosive missile, Figure 2.7 from a shoulder-launch platform (Figure 2.10). Electro-optical sensors guide the missile toward the target, which is then disabled upon impact. These re-usable rounds are effective against type 1, 2, and 3 UAVs up to a 5-kilometer range, but the ballistic nature of this system limits its availability and usefulness in populated areas.

Figure 2.8: SAVAGE Launcher [11]

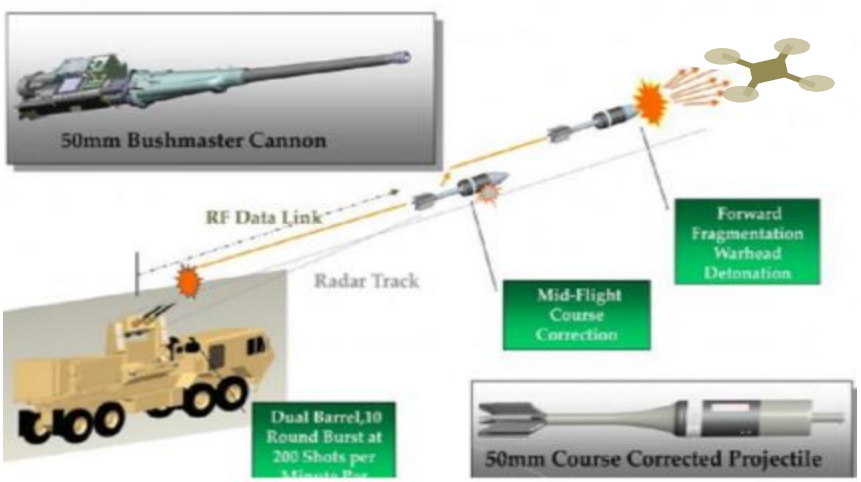

Figure 2.9 Operation of Anti-UAV 50-mm Shell [13]

Some counter-UAV devices employed by military groups are too large for a single soldier to wield and must be transported by a large vehicle. This category includes 50-mm anti-UAV shells launched from the Northrop Grumman Bushmaster cannon [12], as shown in Figure 2.9, as well as any standard vehicle-mounted automatic firearm. Some devices, such as the Lockheed Martin ATHENA, destroy their targets with directed laser weapons. Due to the military nature of larger devices such as these, their marketability and

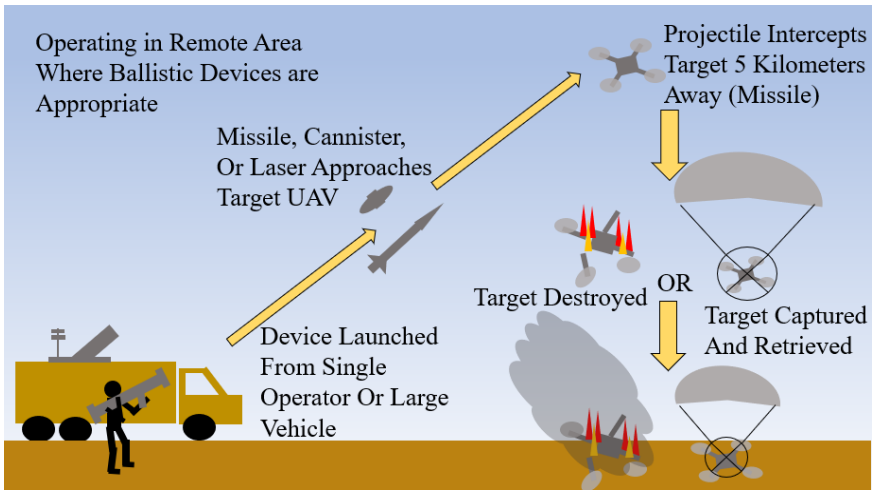

Figure 2.10: Shoulder or Vehicle Launcher CONOPS

viability in populated areas is greatly reduced. All launched projectile products require a line of sight between the target and the launcher to be effective. Furthermore, the target is destroyed, preventing forensic analysis. A CONOPS diagram is shown in Figure 2.10.

2.3 Airborne Platforms

Perhaps the safest (although somewhat complex) solution to the counter-drone problem is a fully controlled airborne platform which intercepts smaller UAVs non-destructively. Systems of this type, as seen in service by Japanese police forces [14], can capture UAVs in a populated area without the use of high-energetics and without a line-of-sight connection to the target. Such a system is the Delft Dynamics DroneCatcher [15]. As shown in Figure 2.11, the DroneCatcher utilizes a quad-copter configuration, with a mounted pneumatic net gun with a range of 20 meters. The DroneCatcher intercepts a target with a speed of 20 meters per second, then hovers nearby before firing the net. The captured UAV can be towed back to an operator or dropped with a parachute if the target is too heavy to retrieve. The DroneCatcher system is safe to use in populated areas but requires a ground station and an experienced pilot. A CONOPS diagram for this device is shown in Figure 2.12.

Figure 2.11: Delft Dynamics DroneCatcher [15]

A comparison between the CONOPS diagrams of all three system types (Figure 2.3, Figure 2.10, and Figure 2.12) reveals that nearly all launcher devices on the market are unsafe for use in populated areas, and that a "soft-kill" via jamming or capture can reduce collateral damage and provide valuable forensic data on the target. None of these devices are both available to civilians and simple to use without specialized training.

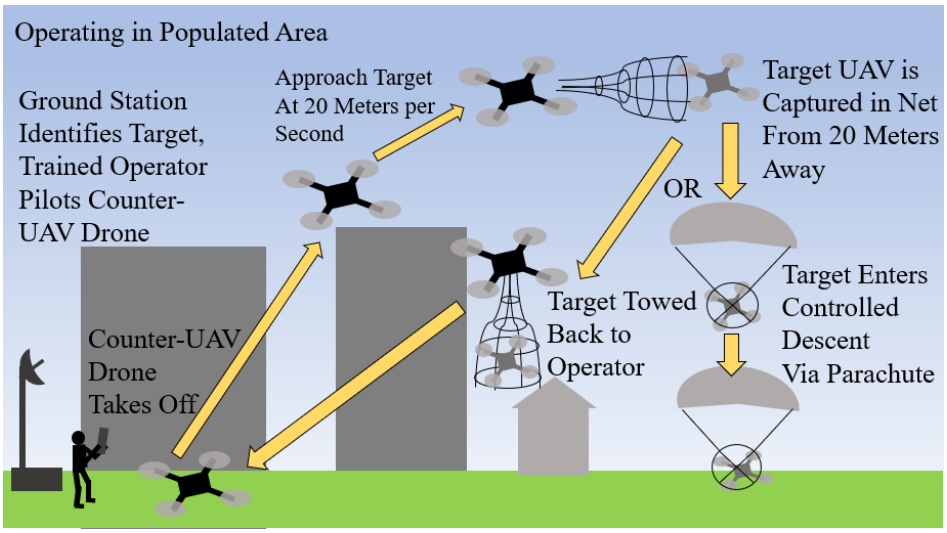

Figure 2.12: Airborne Platform CONOPS

3. Introduction of Design

Since UAVs and the threats they pose vary greatly and change quickly, versatility and adaptability were key considerations while designing this vehicle. Furthermore, system safety and mitigation of collateral damage are points of concern for any combat system. With these parameters in mind, the HFB-WEB team has created the RHI*NO (Ramming Halo Interceptor *Net Optional): A re-usable and durable UAV system which is capable of multiple interception techniques.

The coleopter configuration of the RHI*NO allows for vertical takeoff and landing from uneven ground, transition to a high-speed climb or dash, very high maneuverability, hover capability, and survival of extreme forces and impacts during operation. An emphasis on human situational awareness and system redundancy help to improve safety and mitigate collateral damage. A robust sensor suite ensures accurate payload delivery, and probability-of-kill is increased greatly by the ability to turn and re-engage a target. The standard payload allows for up to six kills per deployment, with even more possible through other engagement strategies. Payloads can be deployed during a close overfly maneuver, or in a hovering loiter above slower-moving targets.

Key features of the RHI*NO, later referred to as the hovering missile and Hovering Missile System (HMS), are outlined in Figure 3.1 and include a titanium-armored Kevlar fuselage, microstator guards to reduce operational noise and protect the variable pitch scimitar-blade propellers, and a standard payload which disables targets with nets fired from shotgun shells. Electric motors eliminate storage and flight control concerns related to fuel burn and internal combustion engines while providing exceptional performance at altitude. High-precision acoustic vector sensors and high-definition video transmitted to the operator in real time allow for first person (with depth perception) supervision or control of interceptions, as well as human assessment of target priority and identity to supplement the identification algorithms of the onboard computer. Electronically hardened internal components (all of which are currently available TRL 10 devices) and triple-redundant flight controls offer reliability during any mission. The entire system fits into a compact case and can be quickly assembled and launched by a single operator in a hostile environment.

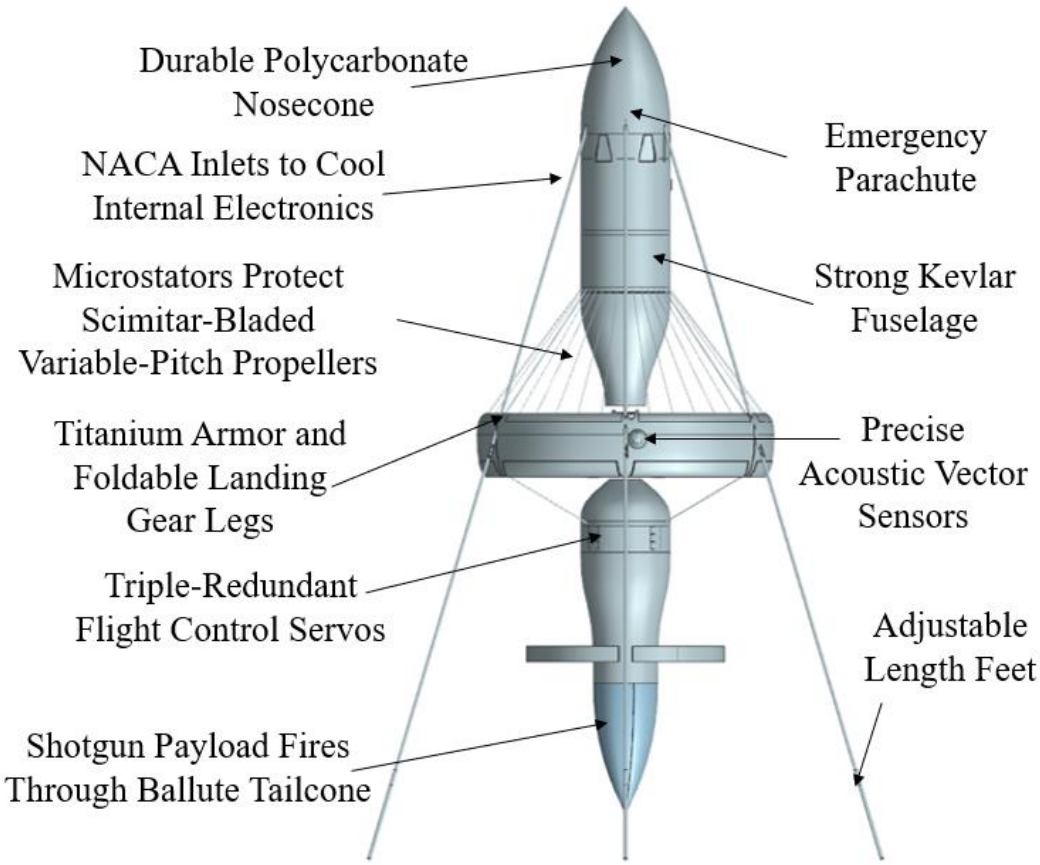

Figure 3.1: RHI*NO Design Features Overview

The RHI*NO was developed as a conceptual expansion of the XQ-138 project [16]; a compact aircraft with exceptional performance, control, and durability. Since the XQ-138 is known to have favorable handling and flight qualities, three size variations of the RHI*NO are scaled with these known proportions. These variations offer differing payload sizes for different missions and customers, so that every operator can choose their preferred balance between safety and firepower.

The performance characteristics of this design suggest that targets far beyond those detailed in the competition guidelines can be engaged: UAVs of class I to class V, ground targets, small manned aircraft, and beyond. The re-usable nature of the RHI*NO greatly reduces the system cost-per-interception compared to more conventional (and more dangerous) ballistic devices. As outlined in this report, the RHI*NO stands to replace huge portions of the current market for counter-UAV devices and provide a versatile and robust platform for military and security forces for years to come.

4. Initial Design Considerations

The following section details the process by which the system design configuration and target drone engagement methods were chosen by providing an overview of the design optimization function and its parameters and utilizing this function for the initial design down-selection.

4.1 Design Optimization Function

The following optimization function provides a method to quantitatively assess and compare the viability and desirability of each preliminary design and engagement mechanism considered for purposes of down-selection.

$$OF = \prod_{i=1}^{13} R_i \cdot \sum_{j=1}^{14} O_j \qquad \textbf{(Eq.1)}$$

The following requirements and their respective quantities were predetermined by those listed in the RFP [1].

$$R_1 = \begin{cases} 0 & if\ unable\ to\ interdict\ group\ 2\ UAVs \\ 1 & if\ able\ to\ interdict\ group\ 2\ UAVs \end{cases} \qquad \textbf{(Eq. 2)}$$

$$R_2 = \begin{cases} 0 & if\ W_{LS} > 40\ lb \\ 1 & if\ W_{LS} \leq 40\ lb \end{cases} \qquad \textbf{(Eq. 3)}$$

$$R_3 = \begin{cases} 0 & if\ W_{TS} > 125\ lb \\ 1 & if\ W_{TS} \leq 125\ lb \end{cases} \qquad \textbf{(Eq. 4)}$$

$$R_4 = \begin{cases} 0 & if\ warhead\ arming\ distance\ \leq 200\ ft \\ 1 & if\ warhead\ arming\ distance\ > 200\ ft \end{cases} \qquad \textbf{(Eq. 5)}$$

$$R_5 = \begin{cases} 0 & if\ payload\ change\ time > 5\ min \\ 1 & if\ payload\ change\ time \leq 5\ min \end{cases} \qquad \textbf{(Eq. 6)}$$

$$R_6 = \begin{cases} 0 & if\ IOC\ occurs\ after\ December\ 2027 \\ 1 & if\ IOC\ occurs\ by\ December\ 2027 \end{cases} \qquad \textbf{(Eq. 7)}$$

$$R_7 = \begin{cases} 0 & if\ rate_{production} < 20\ TS\ per\ year \\ 1 & if\ rate_{production} \geq 20\ TS\ per\ year \end{cases} \qquad \textbf{(Eq. 8)}$$

$$R_8 = \begin{cases} 0 & if\ range < 3.0\ nmi \\ 1 & if\ range \geq 3.0\ nmi \end{cases} \qquad \textbf{(Eq. 9)}$$

$$R_9 = \begin{cases} 0 & if\ h_{max} < 3{,}000\ ft\ AGL \\ 1 & if\ h_{max} \geq 3{,}000\ ft\ AGL \end{cases} \qquad \textbf{(Eq. 10)}$$

$$R_{10} = \begin{cases} 0 & if\ F_k < 10\ UAVs\ per\ hr \\ 1 & if\ F_k \geq 10\ UAVs\ per\ hr \end{cases} \qquad \textbf{(Eq. 11)}$$

$$R_{11} = \begin{cases} 0 & if\ a_{launch} > 2\ g's \\ 1 & if\ a_{launch} \leq 2\ g's \end{cases} \qquad \textbf{(Eq. 12)}$$

$$R_{12} = \begin{cases} 0 & if\ noise_{100\ ft} > 120\ dBA \\ 1 & if\ noise_{100\ ft} \leq 120\ dBA \end{cases} \qquad \textbf{(Eq. 13)}$$

$$R_{13} = \begin{cases} 0 & if\ storage\ life < 10\ yrs \\ 1 & if\ storage\ life \geq 10\ yrs \end{cases} \qquad \textbf{(Eq. 14)}$$

The objectives encapsulate HFB-WEB's primary goals for the system's design. The coefficients associated with each of the design objectives are correlated with the relative importance of each metric as defined by the team.

$$O_1 = 6 \begin{cases} \dfrac{range - 3.0\ nmi}{0.5\ nmi} & if\ 3.0\ nmi < range < 3.5\ nmi \\ 1 & if\ range \geq 3.5\ nmi \end{cases} \qquad \textbf{(Eq. 15)}$$

$$O_2 = 2 \begin{cases} \dfrac{h_{max} - 3{,}000\ ft}{2{,}000\ ft} & if\ 3{,}000\ ft < h_{max} < 5{,}000\ ft \\ 1 & if\ h_{max} \geq 5{,}000\ ft \end{cases} \qquad \textbf{(Eq. 16)}$$

$$O_3 = 3 \begin{cases} 0 & if\ system\ can\ only\ interdict\ in\ daylight \\ 1 & if\ system\ can\ interdict\ at\ night \end{cases} \qquad \textbf{(Eq. 17)}$$

$$O_8 = 8 \begin{cases} 0 & if\ unable\ to\ interdict\ group\ 1\ UAVs \\ 1 & if\ able\ to\ interdict\ group\ 1\ UAVs \end{cases} \qquad \textbf{(Eq. 22)}$$

$$O_9 = 5 \begin{cases} \dfrac{125\ lbs - W_{TS}}{50\ lbs} & if\ 75\ lb < W_{TS} < 125\ lb \\ 1 & if\ W_{TS} \leq 75\ lb \end{cases} \qquad \textbf{(Eq. 23)}$$

$$O_{10} = 8 \begin{cases} 0 & if\ sensor\ type/placement\ is\ nonideal \\ 1 & if\ sensor\ type/placement\ is\ ideal \end{cases} \qquad \textbf{(Eq. 24)}$$

$$O_4 = 8\begin{cases} 0 & if\ neither\ FCC\ or\ FAA\ regulations\ are\ met \\ 0.5 & if\ either\ FCC\ or\ FAA\ regulations\ are\ met \\ 1 & if\ both\ FCC\ and\ FAA\ regulations\ are\ met \end{cases} \quad \textbf{(Eq. 18)}$$

$$O_5 = 7\begin{cases} 0 & if\ energetics\ or\ pyrotechnics\ are\ used \\ 1 & if\ no\ energetics\ or\ pyrotechnics\ are\ used \end{cases} \quad \textbf{(Eq. 19)}$$

$$O_6 = 2\begin{cases} \dfrac{2\ \text{min} - t_{intercept}}{1\ min} & if\ 1\ min < t_{intercept} < 2\ min \\ 1 & if\ t_{intercept} \leq 1\ min \end{cases} \quad \textbf{(Eq. 20)}$$

$$O_7 = 5\begin{cases} \dfrac{\$5{,}000 - \frac{cost}{interdiction}}{\$2{,}000} & if\ \$2{,}000 < \frac{cost}{interdiction} < \$5{,}000 \\ 1 & if\ \frac{cost}{interdiction} \leq \$2{,}000 \end{cases} \quad \textbf{(Eq. 21)}$$

$$O_{11} = 10\begin{cases} 0 & if\ TD\ dropped \\ 0.5 & if\ TD\ parachute\ is\ employed \\ 1 & if\ TD\ captured\ and\ hauled\ to\ base \end{cases} \quad \textbf{(Eq. 25)}$$

$$O_{12} = 5\begin{cases} 0 & if\ part\ count > part\ count_{DJI\ Phantom\ I} \\ 1 & if\ part\ count < part\ count_{DJI\ Phantom\ I} \end{cases} \quad \textbf{(Eq. 26)}$$

$$O_{13} = 10\begin{cases} 0 & if\ maneuverability < target\ UAVs \\ 0.5 & if\ maneuverability = target\ UAVs \\ 1 & if\ maneuverability > target\ UAVs \end{cases} \quad \textbf{(Eq. 27)}$$

$$O_{14} = 3\begin{cases} 0 & if\ expert\ (t_{train} > 8\ hr) \\ 0.5 & if\ intermediate\ (1\ hr < t_{train} \leq 8\ hr) \\ 1 & if\ beginner\ (t_{train} \leq 1\ hr) \end{cases} \quad \textbf{(Eq. 28)}$$

4.2 Configuration Down-Selection

The effectiveness of each design type considered for this mission can be assessed with the optimization function described in the above section. The following seven configurations are considered and analyzed: a missile, a hovering missile, a quad-rotor missile, a quadcopter, a fixed wing UAV, a line-of-sight jammer gun, and a line-of-sight shotgun. The missile considers the use of both a warhead and a reinforced structure for ramming target drones. The hovering missile, quad-rotor missile, quadcopter, and fixed wing designs each consider the following engagement methods: a shotgun that deploys net-packed shells, a pneumatic net gun, the use of Kevlar strands for entangling the rotors of target drones, and a ramming technique. The two line-of-sight configurations only consider a single kill method: a jamming signal from the jammer gun or a net from the shotgun. Table 4.1 outlines the requirements and objectives that are met by each system configuration, along with their final score as determined by the optimization function. Designs that fail to meet the mission requirements are highlighted in red, and the highest scoring designs are highlighted in green. The engagement methods associated with the highest scoring configuration are detailed and down selected in the following section.

This effectiveness analysis suggests that a re-usable hovering missile design will be the most effective configuration for this mission, although it is unclear which of the engagement mechanisms (a shotgun net, a pneumatic net gun, rotor entanglement via Kevlar strands, or reinforcing the structure for ramming) are most advantageous, as the closeness of the total optimization function scores indicate. A modular hovering missile with multiple payload options is likely the most effective against a large range of targets in many interception scenarios. This versatility increases the likelihood of intercepting each and any target drone, as there are multiple engagement mechanisms available upon each deployment of the hovering missile. This level of variability is optimal due to the wide range of drones that this system must be capable of intercepting.

Table 4.1: System Design and Engagement Method Down-Selection Via the Optimization Function Defined in Chapter 3.1

System Design Configuration		Engagement Method	Requirements													Objectives														Optimization Function Total Score
			R_1	R_2	R_3	R_4	R_5	R_6	R_7	R_8	R_9	R_{10}	R_{11}	R_{12}	R_{13}	O_1	O_2	O_3	O_4	O_5	O_6	O_7	O_8	O_9	O_{10}	O_{11}	O_{12}	O_{13}	O_{14}	
Missile	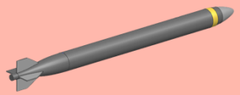	**Warhead**	1	1	1	1	1	1	1	1	1	1	**0**	1	1	6	2	3	8	0	2	0	0	0	8	0	5	10	1.5	**0 (Requirements not Met)**
		Ramming	1	1	1	1	1	1	1	1	1	1	**0**	1	1	6	2	3	8	7	2	0	0	0	8	0	5	10	1.5	**0 (Requirements not Met)**
Hovering Missile	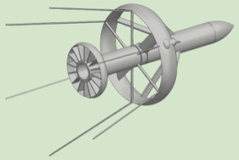	**Shotgun Net**	**1**	**1**	**1**	**1**	**1**	**1**	**1**	**1**	**1**	**1**	**1**	**1**	**1**	**6**	**2**	**3**	**8**	**0**	**2**	**5**	**8**	**5**	**8**	**2.5**	**5**	**10**	**0**	**64.5**
		Pneumatic Net Gun	**1**	**1**	**1**	**1**	**1**	**1**	**1**	**1**	**1**	**1**	**1**	**1**	**1**	**6**	**2**	**3**	**8**	**7**	**2**	**5**	**8**	**5**	**8**	**5**	**5**	**10**	**0**	**74**
		Kevlar Strands	**1**	**1**	**1**	**1**	**1**	**1**	**1**	**1**	**1**	**1**	**1**	**1**	**1**	**6**	**2**	**3**	**8**	**7**	**1**	**5**	**8**	**5**	**8**	**5**	**5**	**10**	**0**	**73**
		Ramming	**1**	**1**	**1**	**1**	**1**	**1**	**1**	**1**	**1**	**1**	**1**	**1**	**1**	**6**	**2**	**3**	**8**	**7**	**2**	**5**	**8**	**5**	**8**	**0**	**5**	**10**	**0**	**69**
Quad-Rotor Missile		Shotgun Net	1	1	1	1	1	1	1	1	1	1	1	1	1	6	2	3	8	0	2	5	0	5	0	0	0	5	0	36
		Pneumatic Net Gun	1	1	1	1	1	1	1	1	1	1	1	1	1	6	2	3	8	7	2	5	8	5	0	5	0	5	0	56
		Kevlar Strands	1	1	1	1	1	1	1	1	1	1	1	1	1	6	2	3	8	7	1	5	0	5	0	5	0	5	0	47
		Ramming	1	1	1	1	1	1	1	1	1	1	1	1	1	6	2	3	8	7	1	0	0	0	0	0	0	5	0	32
Quadcopter	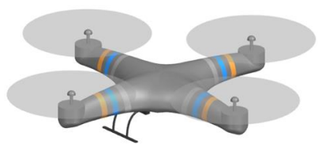	Shotgun Net	1	1	1	1	1	1	1	1	1	1	1	1	1	6	2	3	8	0	2	5	0	5	8	0	0	5	1.5	45.5
		Pneumatic Net Gun	1	1	1	1	1	1	1	1	1	1	1	1	1	6	2	3	8	7	2	5	8	5	8	2.5	0	5	1.5	63
		Kevlar Strands	1	1	1	1	1	1	1	1	1	1	1	1	1	6	2	3	8	7	1	5	8	5	8	2.5	0	5	1.5	62
		Ramming	1	1	1	1	1	1	1	1	1	1	1	1	1	6	2	3	8	7	2	0	8	0	8	0	0	5	1.5	50.5
Fixed Wing		Shotgun Net	1	1	1	1	1	1	1	1	1	1	1	1	1	6	2	3	8	0	2	5	0	5	0	0	5	0	0	36
		Pneumatic Net Gun	1	1	1	1	1	1	1	1	1	1	1	1	1	6	2	3	8	7	2	5	8	5	0	10	5	0	0	61
		Kevlar Strands	1	1	1	1	1	1	1	1	1	1	1	1	1	6	2	3	8	7	1	5	8	5	0	10	5	0	0	60
		Ramming	1	1	1	1	1	1	1	1	1	1	1	1	1	6	2	3	8	7	2	0	8	0	0	0	5	0	0	41
Line-of-Sight Jammer Gun		**Jamming Signal**	1	1	1	1	1	1	1	**0**	**0**	1	1	1	1	0	0	0	0	7	N/A	0	8	5	N/A	0	5	N/A	3	**0 (Requirements not Met)**
Line-of-Sight Shotgun		**Net Capture**	1	1	1	1	1	1	1	**0**	**0**	1	**0**	**0**	1	0	0	0	8	0	N/A	5	0	5	N/A	0	5	N/A	3	**0 (Requirements not Met)**

4.3 Hovering Missile Engagement System Down-Selection

The first option for engagement of target drones is the use of anti-drone shotgun-launched net shells. The most proven example of these on the market today are SkyNet Mi-5 shells, shown in Figure 4.1, which are already in use in military and civilian law enforcement [18]. These shells are traditional 12-gauge rounds which contain a five-foot wide net [18]. When the rounds are fired, five tethered pieces extend to create the net that wraps around the target drone, as illustrated in Figure 4.2, disabling its propulsion system and crashing it. This leads to impact damage to the drone, and the possibility of drone recovery and examination. The SkyNet shells are equipped with a parachute to prevent damage and injury caused by dangerous falling debris if the target is missed. These shells are already proven to be effective in use against Class 1 and 2 drones, as the Air Force uses these shells with modified Remington Model 870 shotguns [17]. For use in a reusable missile design, some sort of shotgun style launch system would be necessary, although it may not require the range or power of a normal shotgun depending on proximity of the missile to the target. A simple loading of the shotguns shells would take less than 5 minutes to complete ensuring the RHI*NO is fast to return into action.

Figure 4.1: SkyNet Shotgun Net Shells [17]

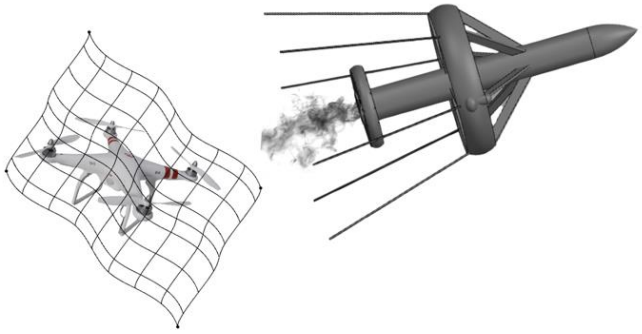

Figure 4.2: Shotgun Net Capture [3]

Another option for capturing a target drone involves the use of a pneumatic net gun, as shown in Figure 4.3. Advantages of using a pneumatic netgun over a shotgun net include the following: there is no need for a casing around the net which allows for nets to be reused and reloaded with ease, the net can be tethered to the system due to the gun's lower firing speed, there is minimal recoil from firing the net, no propellant is necessary which increases safety, and there is no gunshot residue which prevents engine

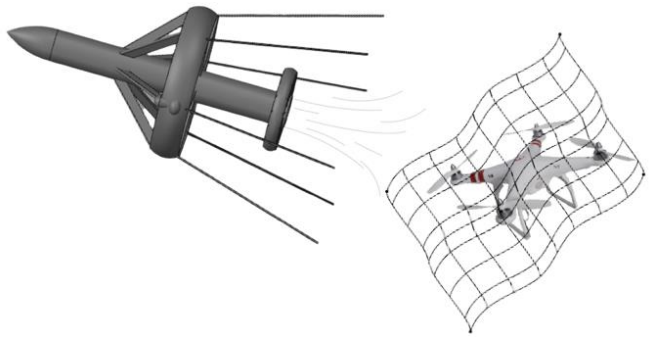

Figure 4.3: Pneumatic Gun Net Capture [3]

ingestion, damage, and stall. A disadvantage of a pneumatic net gun is the low power and firing range of the net. This requires the system to be closer to the target drone for interdiction and capture; the Delft Dynamics DroneCatcher (mentioned in Section 2.3) utilizes a pneumatic net gun with a range of 66 feet [15]. However, by interdicting the target drone at a closer range, less accuracy is required, thereby guaranteeing consistently high rates of interception given the system's maneuverability matches or exceeds that of the target drone. It should be noted that pneumatic guns require a nontrivial amount of compressed air storage even to shoot targets at relatively close distances, which adds additional complexity, volume, and weight to the system.

The third engagement method considered involves interfering with the rotors of the target drone. By dropping or shooting Kevlar strands in its flight path, as shown in Figure 4.4, the Kevlar entangles the exposed rotors to disable the drone and potentially haul it back to base. The employment of this method of drone capture adds an additional level of complexity to prevent the Kevlar from entangling the propulsion system of the anti-drone missile. However, because rotor entanglement has not yet been employed as a method of drone capture, additional research and testing must be performed to more clearly understand the capabilities and limitations of this capture method. While all three of these engagement systems which require firing a net or strands at a target could be deployed during a close overfly maneuver, they could also be deployed after entering a hover above the target and firing downward. This method allows for several attempts at hitting slower-moving targets such as quad-copters.

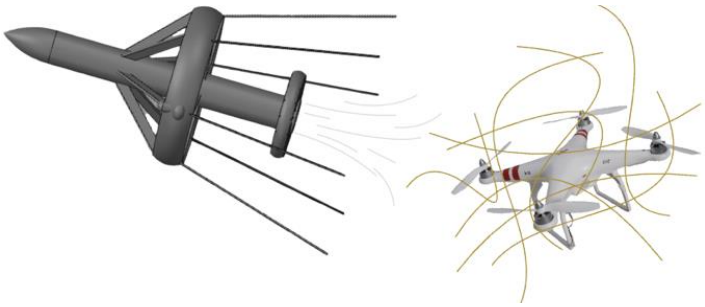

Figure 4.4: Kevlar Strand Rotor Entanglement [3]

The ramming engagement method is considered for its effectiveness and practicality. The baseline method utilizes strengthening certain sections or the whole body of the RHI*NO. Another concept is the inclusion of a front plating which would extend from the nose to act as a horn to pierce enemy systems. The ideal engagement consists of damaging the wing and/or the propeller of the target drone, thereby rendering the target inoperable. To achieve this goal, Kevlar and titanium are both considered due to their high strength and fracture toughness.

Figure 4.5: Piercing Horn Design [3]

The following concepts were taken into consideration: ramming horn, outer rim hardening, and full body hardening. Once the RHI*NO reaches the engagement phase of the operation, the flight speed would increase to ensure the horn pierces the wing, propeller, or body of the target, as shown in Figure 4.5. A potential flaw is if the HMS is unable to penetrate completely through the target drone or create a large enough hole; if this occurs the target may remain on the horn throughout the duration of the flight. This can be avoided by focusing on attacking the outer edges of the wings.

The outer rim variant utilizes strengthening a portion of the casing which surrounds the propeller. The missile engages the target and strikes with this strengthened section against the wings or propeller, as shown in Figure 4.6. With a larger ramming area, this method has a higher probability of successfully striking the target without damaging the missile. This specific area of hardening can be removed and applied as seen necessary for the mission. The complexity of the system is low, as only a layer of plating is attached.

Figure 4.6: Hardened Shell Design for Kinetic Kill [3]

The final ramming technique explored is the full body hardening. This technique employs adding a hardened shell to the entire missile like the exoskeleton of an insect. The missile would then be able to charge full force against the target without concern of how to effectively hit it. It is also the heaviest since the entire system requires armor, thus reducing usable weight. The concept of design is similar to the hardened outer rim design shown in Figure 4.6.

All of these ramming concepts employ the use of microstators over the propeller intake so as to prevent ingestion of debris created through impact. The ramming method of engagement does not allow for controlled descent of the target and debris, which may pose a hazard to civilians if operated in an inhabited location.

Upon comparing and contrasting the target drone engagement methods detailed in this section, it is decided that the first RHI*NO release will employ the use of both a hardened shell design for ramming and an aerial shotgun-launched net shell for disabling the target drone. The pneumatic net gun is provided as an option for future models and product releases of the RHI*NO if more densely packed compressed air storage can be achieved. The Kevlar strand payload was considered as an option, but testing resulted in the strands becoming entangled with one another and being ineffective.

5. Systems Design

The following section documents the sensor and communication system selection for the RHI*NO HMS.

5.1 Stability and Control Sensors

Several sensors are needed for the hovering missile to maintain flight control as well as to track and intercept a target. Sensors related to the navigation and control of the vehicle include a gyroscope, accelerometer, compass/magnetometer, and GPS [19]. An inertial measurement unit (IMU) is used in place of the gyroscope, accelerometer, and magnetometer.

5.2 Target Drone Tracking Sensors

Sensors used to identify and track a group I or II UAV include the following types as described by Table 5.1. Due to the high variation among potential targets, at least two of these detection methods must be employed to provide versatility.

Table 5.1: Target Tracking Sensors

Sensor Type	Functionality	Appropriate for Counter-UAV?
IR (Infrared)	Detects changes in heat signature to follow target	YES (May not be effective beyond 130 ft or against some targets [20])
RADAR (Radio Detection and Ranging)	Detects radio waves reflected off target	NO (RADAR antenna too large)
EO (Electro-Optical)	Detect visible light reflected off target	YES (Currently available and compatible with image processing algorithms)
AVS (Acoustic Vector Sensing)	Detect acoustic signature to follow target	YES (Requires tuning out host aircraft noise)
RF (Radio Frequency) Detector	Detect radio communication between target and operator	NO (Detector Too Large)

5.2.1 Acoustic Vector Sensors

Acoustic vector sensors, made commercially available in 2002 by Microflown Technologies, operate on the principle of measuring air particle velocity [21]. Compared to standard acoustic sensors which only measure sound pressure, the AVS system has the capability to determine the direction of an acoustic wave with a measurement at a single point. The AVS has already been integrated into UAVs significantly smaller than the hovering missile as shown in Figure 5.1 and can accurately detect precise acoustic signatures of specific UAV types at a range of 10 Hz to 10 kHz [21] without a line of sight to the target.

Figure 5.1: AVS Onboard Small UAV [21]

The AVS utilizes two wires strung across a channel through which air flows. As an acoustic wave disturbs the air within the channel, the wires are cooled at a differential rate according to the direction and intensity of the wave. This cooling changes the electrical resistance of the wires, allowing for a precise measurement of the direction and distance from which the sound originated. A cluster of three of these sensors pointing in three perpendicular directions can locate the source of a sound within three-dimensional space. As shown in Figure 5.2 and Figure 5.3, these sensors are remarkably small and lightweight, and can be easily integrated onto a UAV.

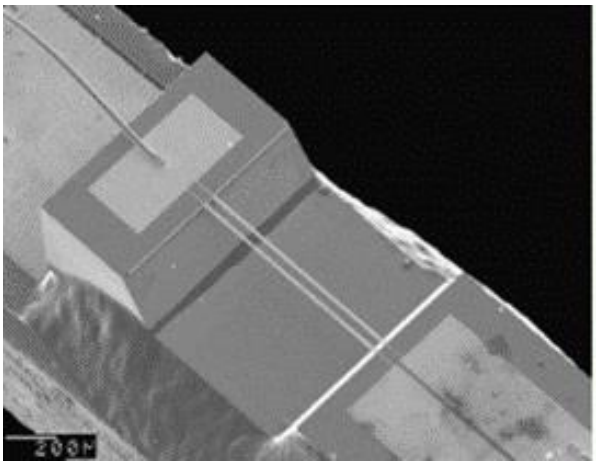

Figure 5.2: AVS Wires Across Airflow Channel [21]

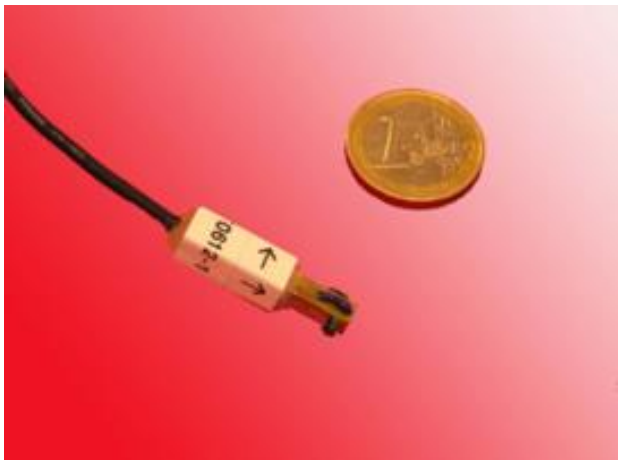

Figure 5.3: AVS Instrument Scale [22]

The AVS system does not require a silent host aircraft to be effective. Background noise caused by rotors or the environment can be filtered out by computer algorithms which search for specific acoustic footprints generated by potential targets. The accuracy of these algorithms for drone detection has been measured at 96% or higher in four different noise environments by a study in 2017 [23], as shown in Table 5.2.

Table 5.2: AVS Drone Identification Accuracy [23]

Setting of Drone Identification	Accuracy	Precision
Crowd	0.964	0.984
Nature in Daytime	0.992	0.983
Nature with Passing Train	0.978	0.983
Street with Traffic	0.964	0.987

If turbulent airflow generated by the hovering missile would impede the accuracy of the AVS system, a rotating casing can be used to create laminar flow over the sensor [24]. This casing would resemble a bullet protruding from the aircraft (shown in Figure 5.4) and would house the AVS. The rotating outer shell would provide laminar flow through which acoustic waves can pass without interruption, as well as protection against dirt particles and debris.

Figure 5.4: Laminar Flow Sensor Housing [24]

While acoustic vector sensors are accurate and conveniently sized, the origin of a 60-decibel noise (about the volume of a normal conversation) can only be tracked from 164 feet away [25]. Therefore, AVS is beneficial for end-game maneuvers, but requires supplementation from other sensory equipment for tracking outside of this range. As the hovering missile enters the final interception maneuver, the acoustic vector sensors will provide a precise measurement of the target's location in 3D space as shown in Figure 5.5. With this information, the autopilot can execute a ramming maneuver if desired, or closely overfly the target and drop or fire one of several specialized payloads, including SkyNet shells. The acoustic vector sensors remain effective regardless of direction and allow for precise payload deployment when the target is behind or below the hovering missile, as shown in Figure 5.6.

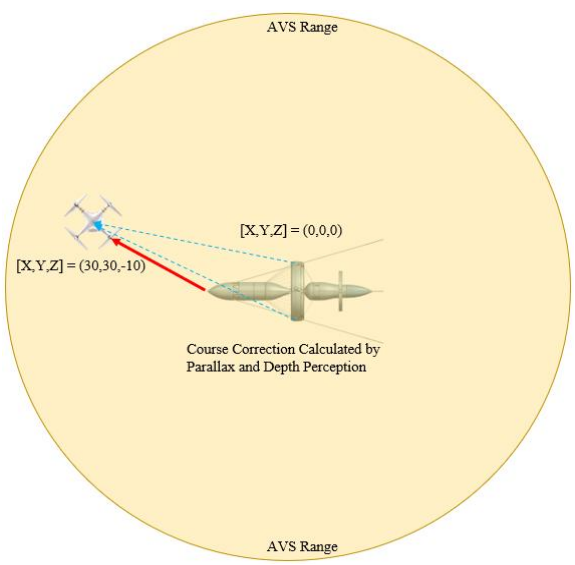

Figure 5.5 : AVS Target Tracking During Approach [26]

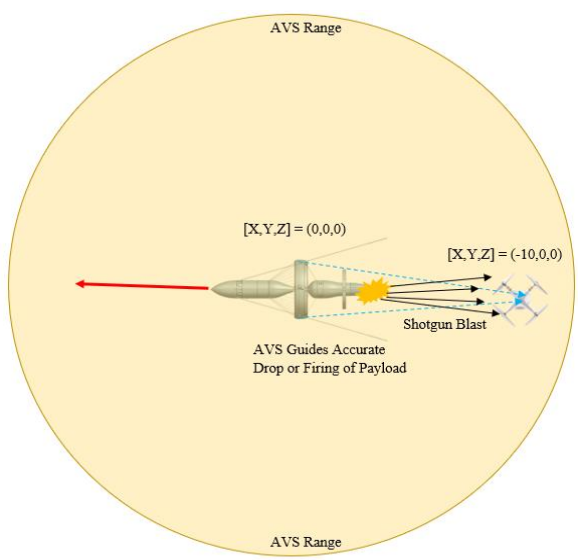

Figure 5.6: AVS Target Tracking During Interception Maneuver [26]

5.2.2 Electro-Optical Sensors

Similar to acoustic vector sensors, electro-optical (EO) sensors offer an extremely lightweight (3.4 g) and compact means of detecting targets within close ranges [27]. Like AVS, a computer algorithm can be used to identify the signature geometry of target UAVs. Electro-optical sensors onboard the hovering missile allow the operator to monitor (and maintain control over) the interception with a first-person view. Integrating two small EO sensors, like the one shown in Figure 5.7, on either side of the rotor shroud increases the effectiveness of the sensors and the situational awareness of the hovering missile via depth perception.

Figure 5.7 Wolfwhoop F4SD FC Integrated OSD [27]

5.3 Ground Station

The modular sensors for stability and control and communications, their specifications, and configuration within the HMS are outlined more thoroughly in Section 8. However, to communicate effectively with the HMS while it is in the field and to track unidentified drones that enter the airspace, a ground station is necessary. This ground station includes an RF sensor and a first-person view (FPV) headset. Due to the long range and minimum weight requirements, the Dedrone RF-160 (shown in Figure 5.8) is utilized as a backup tracking system for the RHI*NO and for detecting target drones that enter the airspace. This detector weighs only 15 lbf [28], so it can be carried into the field with ease. The cameras on board the RHI*NO wirelessly feed into the Orqa FPV.One headset shown in Figure 5.9. While the RHI*NO is capable of operating autonomously, it may still be necessary for a pilot to intervene and direct the drone is friendly UAVs are in the area or in the event that it comes across terrain that can only be realized from a camera. This active pilot monitoring allows for identification of the target drone prior to engagement.

Figure 5.8: Dedrone RF-160 [28]

Figure 5.9: Orqa FPV.One Headset [29]

6. Powerplant Design

The following section documents the propeller, battery, and motor sizing selection and design process for the RHI*NO HMS.

6.1 Propeller Sizing

This section highlights the propeller design for the HMS at 8, 12, and 16 lbs. A blade element momentum theory, (BEMT) code was developed by HFB-WEB and utilized for the analysis of the propeller in all three flight conditions: hover, climb, and dash. The hover condition is defined for a VTOL starting from 5000 ft to an altitude of 10,000 ft at 10 kts. The climb condition is based on traveling 5000 ft vertically and a distance of 3.5 nmi horizontally to achieve a climb gradient of 23.5%. The dash condition is based on traveling the complete distance of 3.5 nmi at a speed of 250 kts. All three of these flight condition specifications are investigated to optimize the RHI*NO's performance.

Two different rotor sizes are analyzed to find the best fit for the mission: the first utilizes a large rotor chord, while the second utilizes a smaller rotor chord at half the value of the first. A rough skin approximation to account for dust and scratches from operation or shipping and handling is estimated to approximate the coefficient of skin friction.

Design relationships between key design features and the rotor diameter are gathered from Ref. 30, as shown in Table 6.1, to use for design calculation estimates. The equations are rearranged to be in terms of rotor diameter, as it made design adjustments simple to employ for a family of sizes of the HMSs.

Table 6.1: Salient Characteristics Relationship to Rotor Diameter [31, 32]

Salient Characteristics	Relationship to Rotor Diameter			
	Large Rotor Chord, Rough Surface		**Small Rotor Chord, Smooth Surface**	
Fuselage Length	$l_f = 2.5D_{rotor}$	**(Eq. 29)**	$l_f = 2.5D_{rotor}$	**(Eq. 37)**
Fuselage Diameter	$D_{fus} = \frac{D_{rotor}}{3}$	**(Eq. 30)**	$D_{fus} = \frac{D_{rotor}}{3}$	**(Eq. 38)**
Rotor Guard Span	$b_{guard} = 1.1D_{rotor}$	**(Eq. 31)**	$b_{guard} = 1.1D_{rotor}$	**(Eq. 39)**
Rotor guard chord	$c_{guard} = \frac{D_{rotor}}{2}$	**(Eq. 32)**	$c_{guard} = \frac{D_{rotor}}{4}$	**(Eq. 40)**
Wetted Area	$S_{wet} = 4.3D_{rotor}^2$	**(Eq. 33)**	$S_{wet} = 2.15D_{rotor}^2$	**(Eq. 41)**
Skin Friction, C_f	C_f =0.004	**(Eq. 34)**	C_f =0.003	**(Eq. 42)**
Parasite Area, f	$f = 10^{-2.3979+Log_{10}(4.3D^2)}$	**(Eq. 35)**	$f = 10^{-2.5229+Log_{10}(2.15D^2)}$	**(Eq. 43)**
Coefficient of Drag, C_D	$C_D = \frac{(10^{-2.3979+Log_{10}(4.3D^2)}}{1.1D_{rotor}^2} + \frac{C_L^2}{2.2\pi}$	**(Eq. 36)**	$C_D = \frac{(10^{-2.5229+Log_{10}(2.15D^2)}}{0.55D_{rotor}^2} + \frac{C_L^2}{1.1\pi}$	**(Eq. 44)**

With the known required thrust, flight speed, and target rotor diameter, the primary featured of the propeller was established. To allow for design flexibility, a non-linear twist in the propeller is incorporated. This allows for increased efficiency between all three flight modes, as the only variable parameters during flight are the rotor speed

and the root pitch angle via a variable pitch propeller. The pitch of the propeller blades is varied by a servo connected to each propeller with a swash plate assembly, as shown Figure 6.1. The BEMT code incorporates Eq. 45 to Eq. 52 [33] to provide realistic values of thrust the propeller produced by the propeller. This code is capable of accounting for the mitigation of tip-loss effects from the induced inflow caused by the utilization of a ducted fan. The code allowed for the generation of plots similar to those shown in Figure 6.2 and Figure 6.3, which indicate where along the span of the propeller that lift is generated or stall occurs. The inflow ratio is calculated from Eq. 45, where r is the radius of the propeller from the root defined from the propeller stations divided by 2 using the trapezoid rule. The induced power/ torque coefficient is calculated based on Eq. 50.

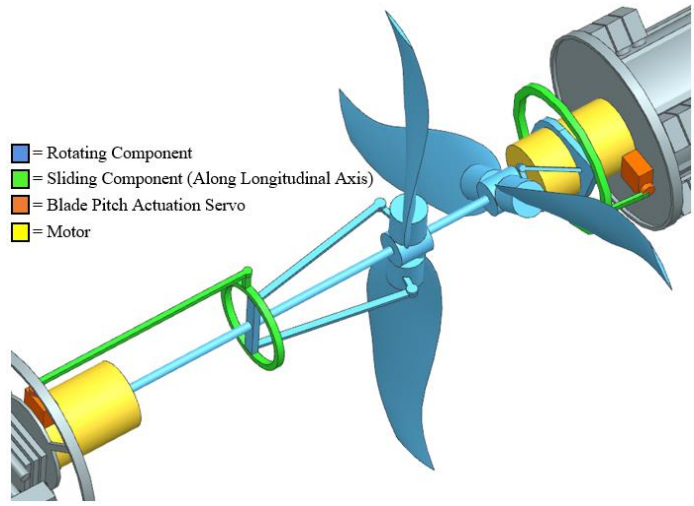

Figure 6.1: Propeller Actuation System

$$\lambda\,(r_n)[\sim] = \frac{\sigma[\sim]C_{l\alpha}\left[\frac{1}{rad}\right]}{16F(r_n)[\sim]}\left(\sqrt{1+\frac{32F(r_n)[\sim]}{\sigma[\sim]C_{l\alpha}\left[\frac{1}{rad}\right]}\theta(r_n)[rad]r_n[\sim]}-1\right) \quad \textbf{(Eq. 45)}$$

$$dC_T[\sim] = \frac{\sigma[\sim]C_{l\alpha}\left[\frac{1}{rad}\right]}{2} * (\theta_0(i) * (r[\sim])^2 - \lambda[\sim]r[\sim]) * dr[\sim] \quad \textbf{(Eq. 46)}$$

$$C_{P0}[\sim] = \frac{\sigma[\sim]C_{d0}[\sim]}{8} + \left(\frac{2\sigma[\sim]d_1[\sim]}{3C_{l\alpha}\left[\frac{1}{rad}\right]}\right)\left(\frac{C_T[\sim]}{\sigma[\sim]}\right) + \left(\frac{4\sigma[\sim]d_2[\sim]}{\left(C_{l\alpha}\left[\frac{1}{rad}\right]\right)^2}\right)\left(\frac{C_T[\sim]}{\sigma[\sim]}\right)^2 \quad \textbf{(Eq. 47)}$$

$$\theta_0\,[rad] = \frac{6C_{Treq}[\sim]}{\sigma C_{l\alpha}\left[\frac{1}{rad}\right]} - 0.75 * \theta_{tw}[rad] + \frac{3\sqrt{2}}{4}\sqrt{C_{Treq}[\sim]} \quad \textbf{(Eq. 48)}$$

$$\theta\,[rad] = \theta_0\,[rad] + r[\sim] * \theta_{tw}[rad] \quad \textbf{(Eq. 49)}$$

$$\frac{dC_Q}{dr}[\sim] = \frac{dC_{Pi}}{dr}[\sim] = C_l * \frac{\sigma}{2} * \frac{\lambda}{r}r^3 \quad \textbf{(Eq. 50)}$$

$$C_{Pideal}[\sim] = \frac{C_T^{\frac{3}{2}}}{\sqrt{2}} \quad \textbf{(Eq. 51)}$$

$$FM[\sim] = \frac{C_{Pideal}}{C_{Pi} + C_{P0}} \quad \textbf{(Eq. 52)}$$

To maximize the performance during all three flight phases, an iterative approach was taken by changing the values of θ_1 (a variable in the non-linear twist equation) and θ_{tw} (the linear twist portion). When the lift curve over the propeller span for dash is optimized by bringing it close to 0° angle of attack (AOA) and the blue curve is straight, (Figure 6.2), the propeller is stalled over an increased portion of the span for the hover condition (Figure 6.3). This means the propeller design is optimized for the dash condition of the flight mission. Once an acceptable design was met that showed high efficiency at the required thrust for each flight condition, the values for θ_1 and θ_{tw} were kept constant for the rest of the designs involving that weight of the missile. Table 6.2 displays the key characteristics for each of the chosen propeller designs.

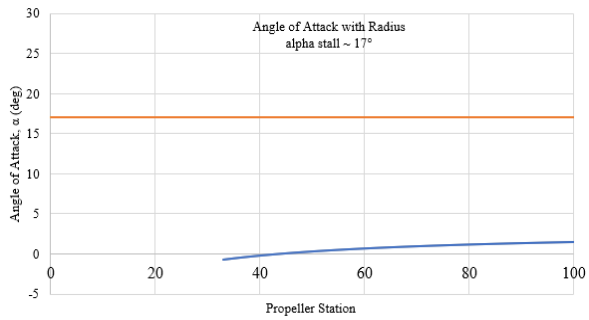

Figure 6.2: Dash Configuration Propeller AOA Created with BEMT Code

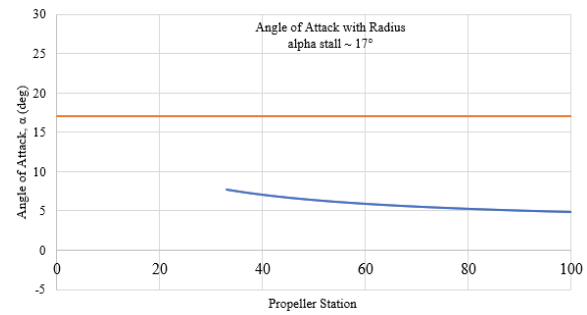

Figure 6.3: Climb Configuration Propeller AOA Created with BEMT Code

Each of the rotor diameters are analyzed with variations only in rotor speed and blade root angle, and a trend is found which displays the required shaft power versus the rotor diameter. The hover, climb, and dash condition trends are superimposed to create a shaft power sizing chart for each missile design weight, as shown in Figure 6.5. Through this method it is possible to find the optimal rotor diameter which fulfills all mission requirements for each weight class of the missile family.

Table 6.2 Salient Propeller Design Characteristics

	8 lb.			12 lb.			16 lb.		
	Hover	Climb	Dash	Hover	Climb	Dash	Hover	Climb	Dash
Diameter Rotor (in)	14.3			17.4			20		
Shaft Power (hp)	1.67	1.05	1.64	2.44	1.59	2.46	3.33	2.15	2.95
Shaft Power (W)	1245	783	1223	1820	1186	1834	2483	1603	2200
Efficiency/FM (%)	54.9	89.3	70.3	56.8	88.6	69.4	55.9	87.8	70.4
Theta0	7	32	30	5	20	20	10	27	30
Theta_1	34			33			34		
Theta_tw	-28			-17			-28		
Rotor Speed (RPM)	6650	5780	11200	4800	4980	9290	4540	4550	8000
Vtip (ft/s)	415	360	700	365	378	705	396	397	700
Fwd Flight Speed (kts)	10	120	250	10	120	250	10	120	250
Root Chord (in)	1.66			2.02			2.33		
Taper Ratio	0.9								
Root Cutout (%)	30								
Number of Rotor Blades	2								
Ducted fan	Yes								
Thrust Calculated (lbf)	10	2.54	1.51	15	3.8	2.24	20	5.08	2.96
CT Calculated	0.0296	0.01	0.0016	0.039	0.009	0.0016	0.033	0.0084	0.0016

6.2 Battery and Motor Sizing

The initial concept design utilizes an electric motor and battery as a power plant. This section focuses on the feasibility of this concept and integration into the design family. Multiple electric motors are explored; these motors' prominent traits of weight and electrical power are displayed in Table 6.3. The electrical power converted into

mechanical power assuming a conservative efficiency of 92%. Corresponding ESC's are found for the chosen motors and their weights are considered. Currently, the design utilizes an estimation for the combined weight of the propeller and spinner to be 40 grams. The power to weight ratio of the motor, ESC, and propeller/spinner is obtained from Eq. 54. Li-Thionyl Chloride batteries are used for the calculation. Figure 6.4 was used to obtain the power density of the battery, assuming the time for a single use of this system is 5 mins.

Table 6.3 Electric Motors [34-39]

Electric Motor	Max Power (W)	Weight (g)
Turnigy SK8 6374-192KV Sensored Brushless Motor (14P)	4400	940
PROPDRIVE v2 5060 270KV Brushless Outrunner Motor	2400	438
Turnigy RotoMax 50cc Size Brushless Outrunner Motor	5300	1080
Turnigy SK8 6354-260KV Sensored Brushless Motor (14P)	3000	630
Turnigy SK3 90mm (6S-8S 3000w) Fandrive Brushless EDF Motor - 3968-1500 KV	3000	363
Turnigy XK-4074 2000KV Brushless Inrunner	3000	380

UAVs with standard configurations use 38% of the takeoff weight for the power plant and fuel [40]. This value is used as a mass budget for the design family. The weights are summed in Eq. 55. By rearranging to solve for power, Eq. 56 is obtained and becomes the method employed to justify if an electrical power source is possible.

$$W_{motor,ESC,prop} = \frac{P_{systshaft}}{P/W_{motor,ESC,prop}} \quad \textbf{(Eq. 53)}$$

$$W_{battery} = \frac{P_{systshaft}}{P/W_{battery}} \quad \textbf{(Eq. 54)}$$

$$W_{tot} = budget_{mass} = W_{motor,ESC,prop} + W_{battery} \quad \textbf{(Eq. 55)}$$

$$P_{systshaft} = \frac{W_{tot}}{\frac{W_{motor,ESC,prop}}{P} + \frac{W_{battery}}{P}} \quad \textbf{(Eq. 56)}$$

With the use of the propeller design results, the required shaft power for each of the three flight phases for a variety of rotor diameters is determined. This is performed for 3, 5, 8, 12, 16, and 24 lbf HMS designs. It is found that only the 8, 12, and 16 lbf designs converged to a feasible data point; these results are shown in Figure 6.5. Upon plotting all the required shaft powers and the available shaft power from the electric motors it is observed that the motors for these designs are incapable of producing enough power with the typical 38% weight of takeoff allotment. By increasing the weight used for the power plant and fuel from 38% to 55% of the takeoff weight for these three designs, a viable design is reached. Therefore, a fully electric design is utilized for the RHI*NO HMS.

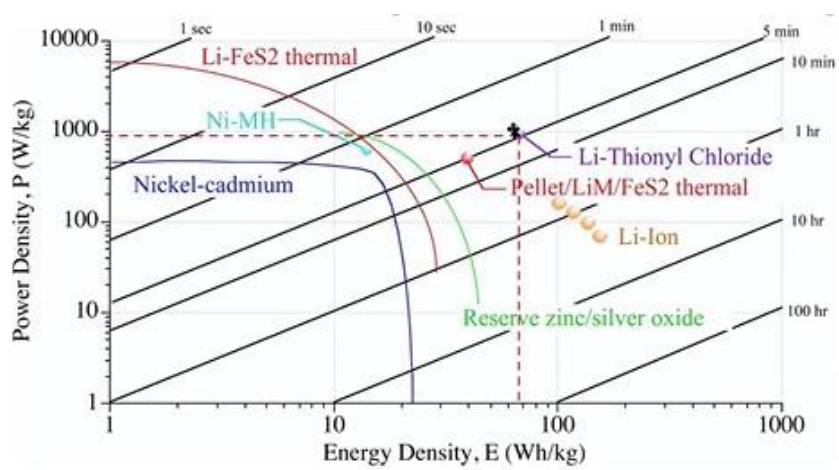

Figure 6.4 Experimentally Gathered Battery Sizing Data [41]

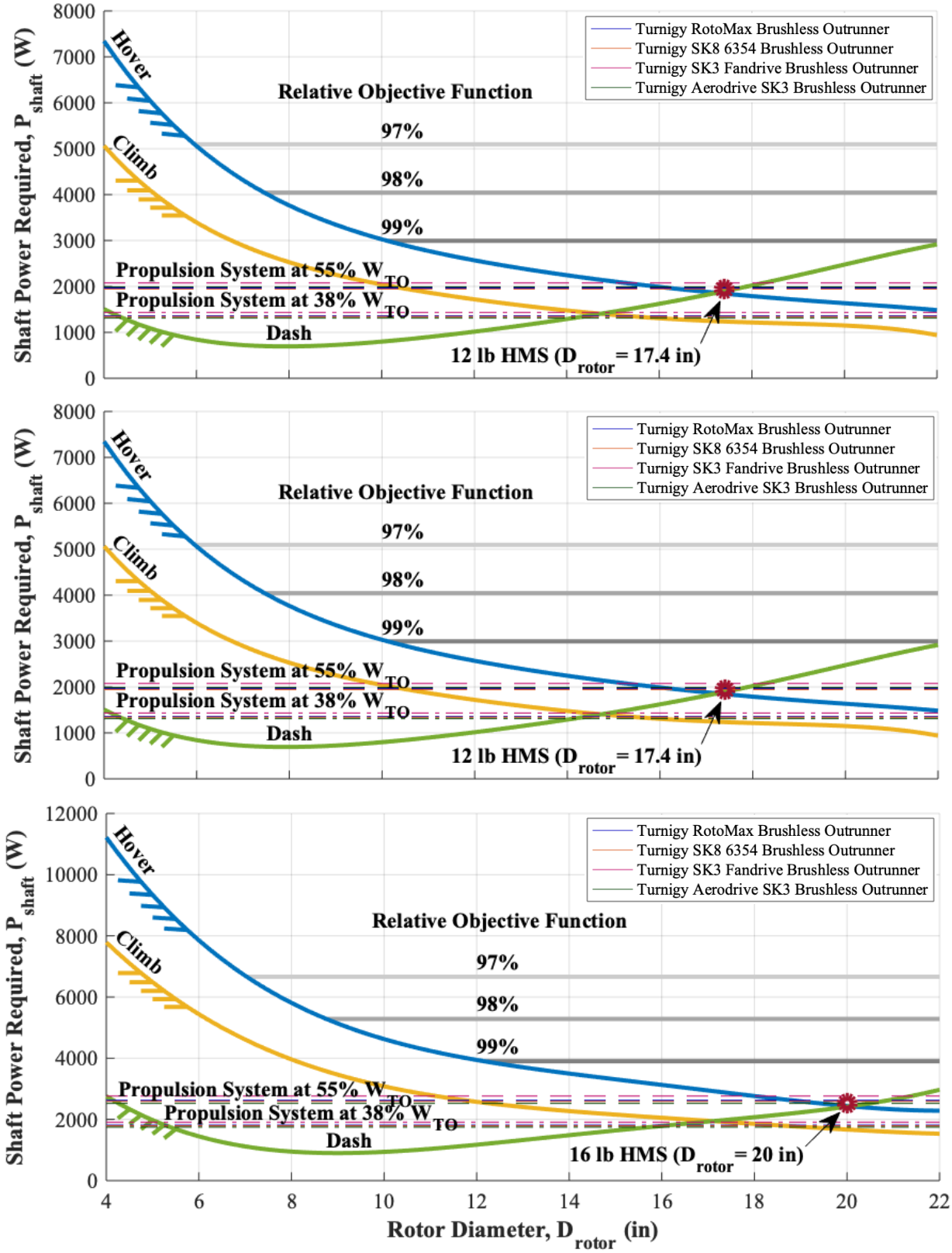

Figure 6.5: Engine Sizing 38% and 55% Takeoff Weight for 8, 12, and 16 lb HMSs

6.3 Doghouse Plot

By making use of the optimized propeller and powerplant design characteristics determined above, the flight envelope of the RHI*NO is determined by running the BEMT code at various altitudes, propeller RPM's, propeller root pitch angles, and flight speeds. The results of this analysis are shown in the doghouse plot in Figure 6.6, illustrating that the RHI*NO vastly exceeds the minimum requirements of the RFP. The HMS is capable of reaching a performance ceiling of 63,000 ft due to the system's use of an electric power plant as opposed to a fuel-based power plant. While there is no drop in motor performance with altitude for electric vehicles, the decrease in propeller efficiency is non-negligible and was therefore accounted for in the calculations performed to generate Figure 6.6. This massive range in performance has major implications on the ability of the RHI*NO to intercept drone classes well outside of those specified in the RFP; this is discussed in more detail toward the end of the report.

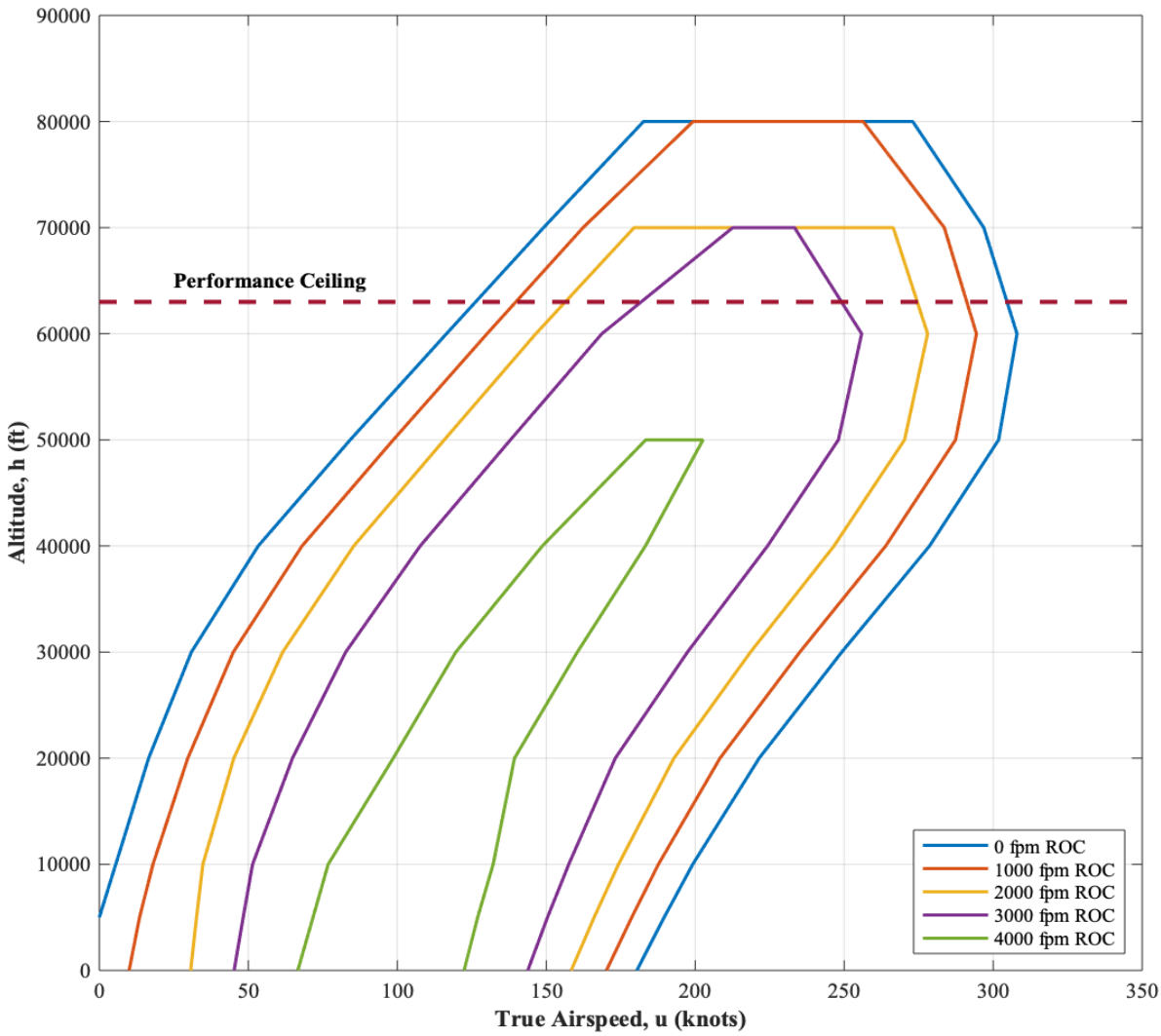

Figure 6.6: 12 lb HMS Doghouse Plot

6.4 Noise Compliance

This section documents the expected noise that the hovering missile design generates. Figure 6.7 displays experimentally collected noise levels recorded in decibels for the XQ-138 design. As the RHI*NO's design configuration is similar to that of the XQ-138, it is expected that the current missile design will produce a maximum of 70 dB at a distance of 100 ft from the launch location. Because the XQ-138 utilized an internal combustion engine and the RHI*NO employs electric motors, this 70 dB estimation is immensely conservative. Therefore, it is guaranteed that the noise emissions are well below the design constraint of 120 dB within 100 ft of the launch location.

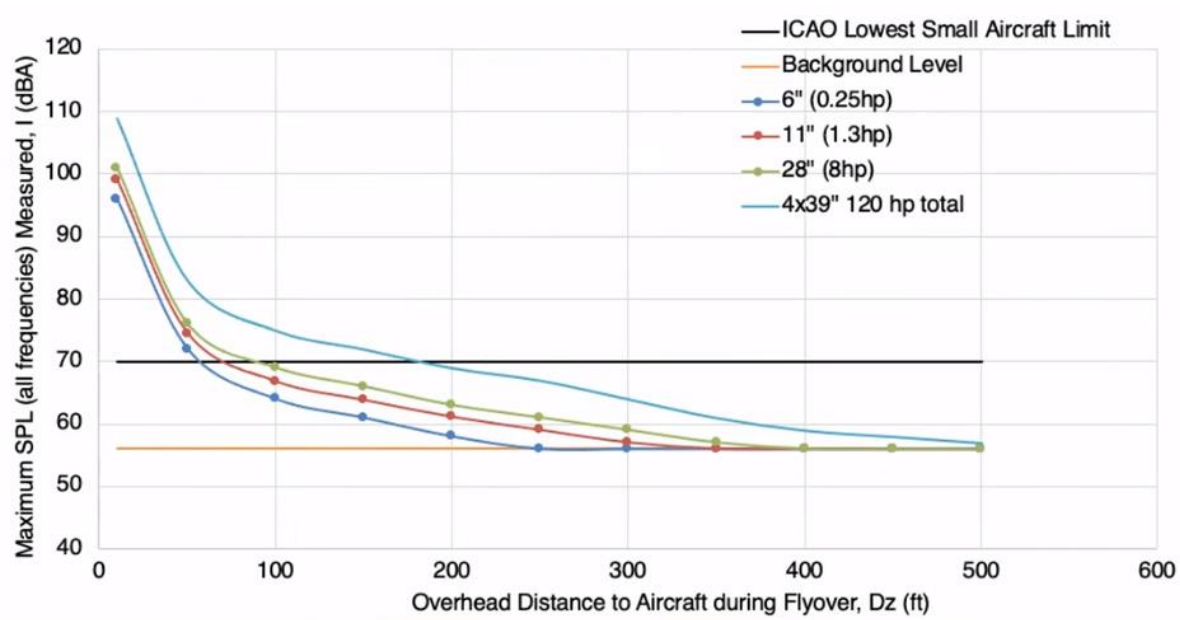

Figure 6.7: XQ-138 Experimentally Collected Noise Levels [42]

Moreover, the chosen RHI*NO design implements the use of microstators – documented later in the report – to smooth the incoming rotor flow and decrease the noise level by more than 3 dB. An experimental noise testing for a conventional ducted fan vs a ducted fan with microstators is shown in Figure 6.8. The provided URL shows a video of the testing and results, performed at The University of Kansas.

Figure 6.8: Conventional vs MicroStator Noise [43]

7. Structural Design

The following section documents the external and internal structural design of the RHI*NO HMS.

7.1 Rotor Guard Design

The rotor guard design is heavily influenced by the rotor design due to the ducted fan design configuration. The span, or diameter, of the rotor guard is nearly the same as the rotor span, thereby preventing rotor tip vortices and maintaining rotor tip loading. The chord of the rotor guard is 25% of the rotor diameter. This chord corresponded with a wetted area that satisfied the drag requirements for dash. These ratios for rotor guard span and chord are similar to that of the XQ-138, a design with the same configuration as the RHI*NO. The airfoil cross-section, however, is not directly related to the rotor diameter. This is instead determined by the practical needs of the rotor. To allow the rotor to smoothly run against the rotor guard to prevent rotor tip vortices, a flat-bottomed cross-section would be necessary. However, a thick cross-section would also be beneficial, as thickness in the rotor guard would allow for the storage of a larger number of batteries. A cross-section with both a flat bottom and a considerable amount of thickness is the Clark Y-18 airfoil, shown below in Figure 7.1. The airfoil data can be found in Ref. 44.

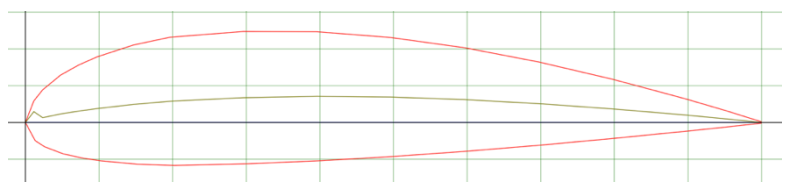

Figure 7.1: Rotor Guard Clark Y-18 Airfoil [45]

7.2 Empennage Design

For control surface design, both a grid fin control surface (shown in Figure 7.2) and a conventional fin control surface design are considered. Grid fins, also known as lattice fins, provide a few important benefits over a conventional fin design. A grid fin provides a greater control authority than a conventional fin of similar size; a point of concern due to the length constraints on the hovering missile body. The hinges for the grid fins are placed directly at the end of the missile body, maximizing the moment arm for control forces to ensure maximum control. Additionally, grid fins can be folded against the body, allowing for more compact storage. It should be noted that grid fins require a more involved manufacturing approach than conventional fin control surfaces due to the intricacies of the design lattice, and the large amount of wetted area will result in significant drag penalties compared to fin control surfaces. Despite this potential drawback,

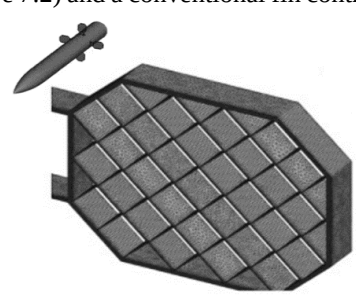

Figure 7.2: Grid Fin [45]

the grid fin empennage design was chosen over a conventional fin design due to the immense benefits that come with increased control authority and maneuverability.

The primary goal of the stability and control analysis is to ensure that the system is stable in return and maneuverable in counter-drone pursuit. A static margin of zero is desirable for flight prior to the use of any interdiction payload, as this provides high maneuverability for endgame maneuvers, without compromising control authority over the system caused by instability. This also results in a positive static margin after interdiction, as the center of gravity shifts forward due to the loss of the interdiction payload weight in the tail, thereby making the RHI*NO stable on return.

To achieve these stability characteristics with grid fins, a longitudinal x-plot, shown in Figure 7.3, was developed. This plot consists of three lines expressed as a function of grid fin area: the most aft flight CG (takeoff weight), the most forward flight CG (weight after the use of interdiction payload), and the HMS aerodynamic center.

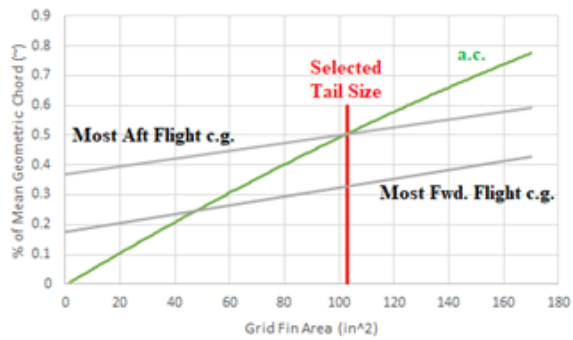

Figure 7.3: RHI*NO Longitudinal X Plot

The CG lines were found using the methods outlined in Section 8.7 using varying grid fin weights. To find the aerodynamic center line, reference 46 was used. To achieve a static margin of zero for the most aft flight CG, a grid fin frontal area of 103 in^2 was necessary, indicating that the grid fins need to extend approximately 3.5 inches outside of the fuselage. It was determined that the grid fins will be circular and divided into four quadrants.

7.3 Titanium Armor Sizing

In Table 7.1, the various armor weight estimations can be seen for the 8, 12, and 16-pound designs. Titanium was selected for the protective material due to its high strength-to-weight ratio. To estimate the armor weight on the fuselage alone, the thickness of the titanium plating is added to the fuselage diameter, and their combined area is found. After this, the area of the fuselage alone is subtracted, resulting in the area of the armor surrounding the fuselage. This area is multiplied by the length of the fuselage to get the volume of the armor encasing the RHI*NO's fuselage. This volume is multiplied by the density of titanium for the total weight of the fuselage armor. The same process is used to find the volume and weight of the armor on the shroud.

Table 7.1: Titanium Armor Weight

Size of Design (lb)	Leading Edge and Forward Fuselage Armor (lb)
8	0.438
12	0.494
16	0.725

It should be noted that a partially armored configuration was selected, covering the front fuselage and leading edge of the shroud. A fully armored design is unnecessary and would add extra weight. The nose of the system is left unarmored and is made out of polycarbonate to ensure electric and optical transparency for the sensors.

7.4 External Structure

As shown in Figure 7.4, the RHI*NO features a sleek fuselage design; to reduce wetted area, a section of the forward fuselage is cut away and supported by the microstators and landing gear. Additionally, the aft fuselage is narrowed by wrapping the external structure around the internal components to eliminate wasted space. For drag reduction, a ballute on the tail of the design allows for steady airflow from the fuselage into the free stream (instead of a perpendicular drop which causes the drag coefficient to double). The ballute is a hollow, inexpensive, replaceable structure made of thin plastic film through which the SkyNet shells are fired during interception. The ballute easily screws into place, allowing for quick replacement of the payload. The six landing gear legs are made of titanium. Table 7.2 provides the salient characteristics of the vehicle configuration.

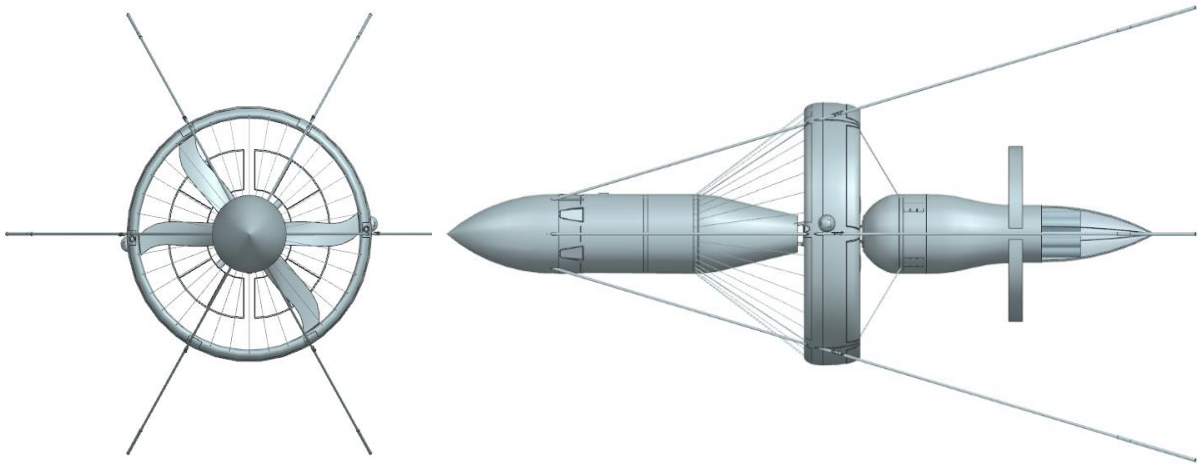

Figure 7.4: Hovering Missile Three-View

7.5 Internal Structure

The skeleton design of the internal structural components of the RHI*NO is shown in Figure 7.5. To support the structure, bulkheads are spaced throughout the fuselage and ribs are placed within the rotor guard. The microstators are connected at ring frames to the fuselage to allow for proper load transfer during ramming and in-flight maneuvers. The skin is a semi-monocoque design of Kevlar composite, and the frontal portion of the fuselage, along with the leading edge of the rotor guard, is layered with titanium as discussed in the titanium armor report section. The microstators and landing gear legs are also made of titanium.

During a ramming maneuver, the loads caused by impact will follow the pathways illustrated in Figure 7.6. Both the landing gear and the microstators act as braces to distribute the initial compressive load on the forward fuselage along the rotor guard to the aft fuselage. After meeting in the aft fuselage, loads are absorbed into a bulkhead designed to withstand compression. Due to the gap between the forward and aft fuselage sections for propeller placement, force is not transferred linearly to the aft fuselage. This arrangement helps to protect the potentially sensitive payload from damage due to sudden deceleration.

Table 7.2: HMS Salient Characteristics

	Rotor Guard	**Grid Fins**
Area (2D Projection)	77.3 in^2	18.7 in^2
Span	19 in	13.8 in
MGC	4.2 in	1 in
MCG LE, FS	26.1 in	41.0 in
Sweep Angle	0	0
Thickness Ratio	0.23	0.1
Airfoil	Clark Y 18 (Stretched)	Plate
Incidence Angle	0 deg	0 deg
	Fuselage	**Overall Aircraft**
Length	43.2 in	46.1 in
Max Diameter	19 in	32.4 in

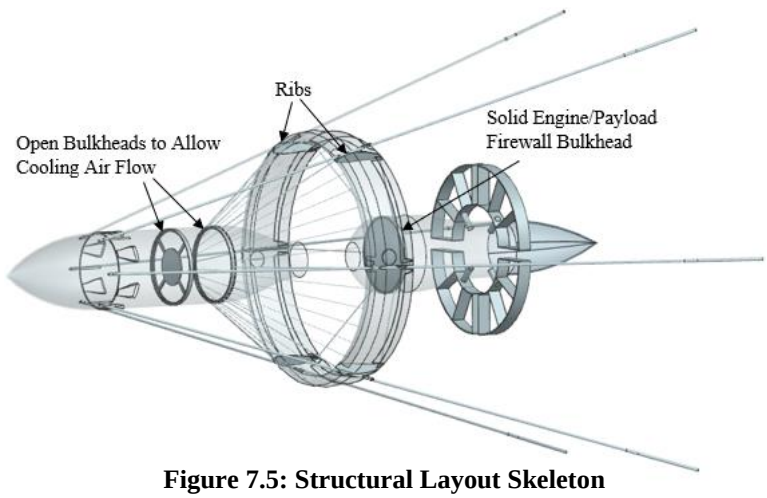

Figure 7.5: Structural Layout Skeleton

7.6 V-n Diagrams

The maneuver and gust loads for the RHI*NO system are shown in the first V-n diagram in Figure 7.7. However, the HMS will be undergoing loads more extreme than those typically encountered by the average UAS. These include substantial shipping and handling loads after being manufactured and immense ramming loads during interception; the second V-n diagram in Figure 7.7 more accurately illustrates these design loads. Therefore, the RHI*NO is designed according to the highest possible load it will experience during its lifetime: ramming.

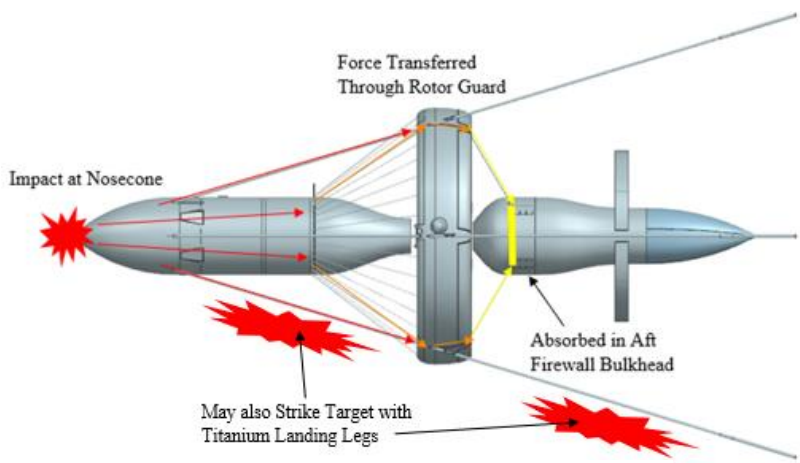

Figure 7.6: Ramming Load Pathways

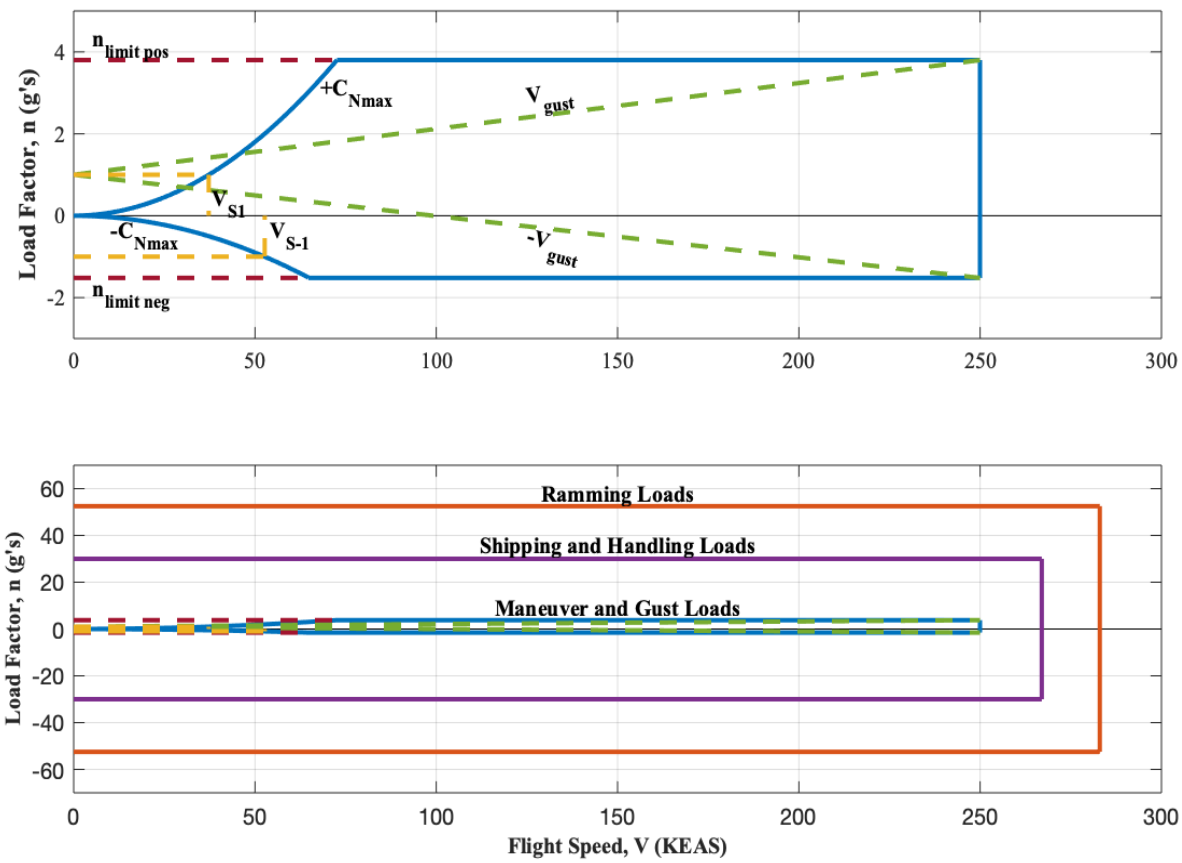

Figure 7.7: RHI*NO V-n Diagrams

7.7 Launch and Recovery System Design

The design of the launch procedure considers the following factors to determine the best configuration: simplicity, effectiveness, weight minimization, practicality, and transportability. The launch methods considered include rocket-assisted, tube-assisted, slingshot, platform, and telescopic landing gear leg designs. The rocket-assisted launch was ruled out by the 2g launch acceleration requirement. The concept of a tube-assisted launch posed the benefit of meeting the RFP shoulder-launch criteria. However, this advantage is heavily outweighed by the concept's lack of transportability; a tube of the same diameter as the RHI*NO would be highly impractical to carry into the field. Therefore, a shoulder-launched design is unjustifiable. While a slingshot launch is ideal in terms of transportability, this concept was eliminated from consideration due to the high probability of incurring an unstable moment on the RHI*NO at launch, as there is no ideal placement on the system for a launch mount. Because the HMS is capable of vertical take-off, a launch platform design was heavily considered to ensure the HMS can be deployed from level ground. Benefits include practicality, quick set up, simplicity, and effectiveness. This method

does, however, require a table-like structure to be carried out into the field. Therefore, the employment of spring-loaded telescopic legs, as shown in Figure 7.8, is the most intuitive approach; this configuration is simple, effective, lightweight, practical, and transportable as no additional components are necessary for launch.

Figure 7.8: Spring-Loaded Telescopic Legs

This design also allows for the HMS to self-level when launching from rugged or uneven terrain, as illustrated in the situational renderings for sandy and rocky terrain in Figure 7.9 and Figure 7.10 respectively. Because the HMS will be taking off vertically in a hover, the maximum launch acceleration of 2 g's can easily be met. The legs will be connected to the propeller shroud via spring-loaded hinges to allow the landing gear to compress into a streamline configuration at highspeed, thereby reducing frontal area and system drag, and allowing for more compact storage.

Figure 7.9: Takeoff from Sandy Terrain

Figure 7.10: Take-off from Rocky Terrain

Many landing configurations were considered for the recovery of the RHI*NO as well: net capture, a parachute, and vertical hover landing. The usage of a net suspended between two poles to catch the system as it approaches the ground was ruled out due to the amount of additional cargo needed for set-up. A parachute landing was the second-best option due to its low size and weight. However, this option adds an additional level of risk due to the possibility of the parachute not deploying at a high enough altitude to reduce speed and prevent damage on impact. The leading configuration is the vertical hover landing due to its low risk of damage in comparison to the other configurations. An additional benefit is that the HMS is already configured for this landing type by the launch

system design. The spring-loaded hinge on the rotor shroud allows for the landing gear to self-deploy at landing flight speeds, and the spring-loaded telescopic leg design will help to reduce impact on hard landings and allow for the HMS to level itself on uneven landings or rugged terrain. An emergency parachute is implemented onboard the HMS as a safety precaution in case of system malfunction, but it will not be used as a primary means of landing.

The backup parachute will be stored in the nosecone of the HMS. To allow for proper deployment and to ensure the parachute release mechanism is failsafe, the nose will be spring-loaded and held in place by pin-released servos. Upon command, the servo will release the pin, the nosecone will be ejected, followed closely by the parachute deployment. To avoid the need for the replacement of the nosecone in the event of an emergency landing, it will be attacked to the parachute via a string. This method of deployment is similar to those used by model rockets, as shown in Figure 7.11.

Figure 7.11: Emergency Parachute Deployment [47]

8. Design Integration

The following section details the integration of the systems, powerplant, and structures of the RHI*NO.

8.1 Layout of Major Systems

This section documents the layout of major systems within the fuselage of the RHI*NO HMS design. A depiction of the fuselage structural layout can be observed in Figure 8.1. The design features removable battery packs housed in the rotor guard with snap-on covers for quick battery replacement in under 2 minutes between landing and relaunch, and a removable nose cone; under which resides the parachute and parachute release mechanism.

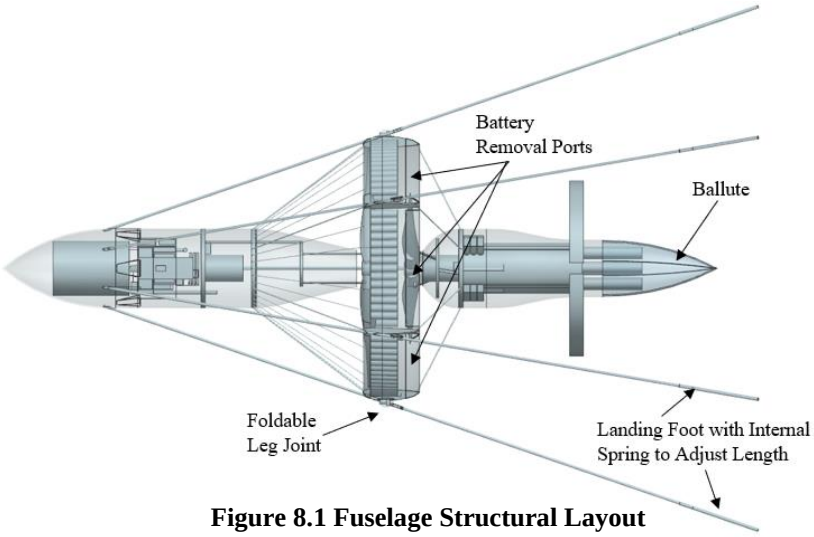

Figure 8.1 Fuselage Structural Layout

The sensors and flight computer are housed in the forward section of the fuselage. As the effect of interference between the electric motor and the sensors is unknown, the spacing between them is maximized [48]. The testing of these electromagnetic interferences is documented later in the report.

There is expected to be interference between the sensor transmitter and the FPV transmitter, as the two are co-located at the nose of the HMS. To mitigate this interference, the operating frequencies will be offset from each other. The FPV will transmit at a frequency of 5.8 GHz and be received from the ground station at 900 MHz. The sensor transmitter will be set at a frequency of 2.4 GHz. This frequency difference will allow for both transmitters to operate with minimal interference [49].

The wires between the sensors and flight computer are assumed to be well insulated so the effects of interference between the two can be ignored [50]. Wires from the aft section of the fuselage will pass through the titanium microstators to the flight computer. Figure 8.4 depicts the concept of electrical wires passing through the microstators. The nose will be constructed of polycarbonate, as this material is both optically and electrically transparent. This material will also encase the optical sensors on the rotor guard for protection during collisions.

The sensors, antenna, and flight computer are housed in a removable metal cage. This cage as depicted in Figure 8.2 and Figure 8.3 allows for easy access and removal of both the flight computer and sensors. The wire buses from the sensors and antenna will be bunched together and zip tied to the side of the cage to prevent excessive movement. Rails will protrude from the side of the metal cage which allow for easy installation and removal side into predefined grooves of the Kevlar fuselage. The rails also serve as a torque box due to the snug-fitting cage.

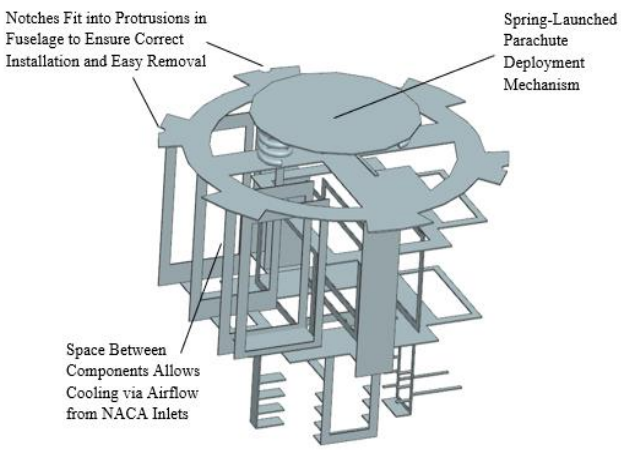

Figure 8.2: Removable Sensor Cage Empty

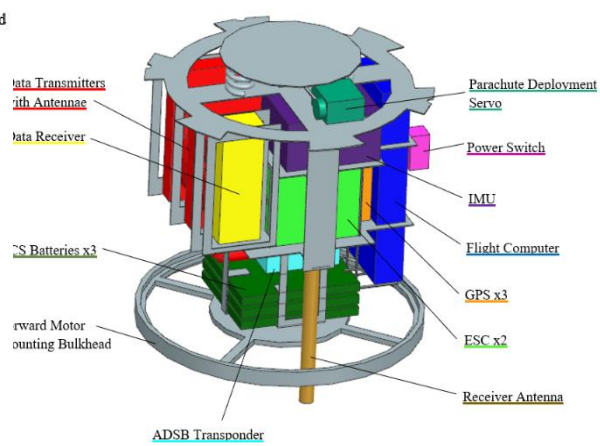

Figure 8.3: Removable Sensor Cage Filled

The RHI*NO features two motors that rotate in opposing directions to allow for increased roll authority and to prevent drag caused by swirling the airflow. By smoothing the incoming airflow from the first propeller the second propeller will experience an increase in produced thrust.

The connection wires between the motors and ESCs will be heat shrunk together and attached to the side of the fuselage with anchored wire busses to prevent excess movement in flight. Servos used for variable pitch of the

propeller are mounted to the fuselage side. The wires are kept away from moving parts of the servos and links to prevent possible entanglement. The servos have a metal foil covering applied to electrically harden them and act as protection from electromagnetic interference. The wiring concept can be observed in Figure 8.4.

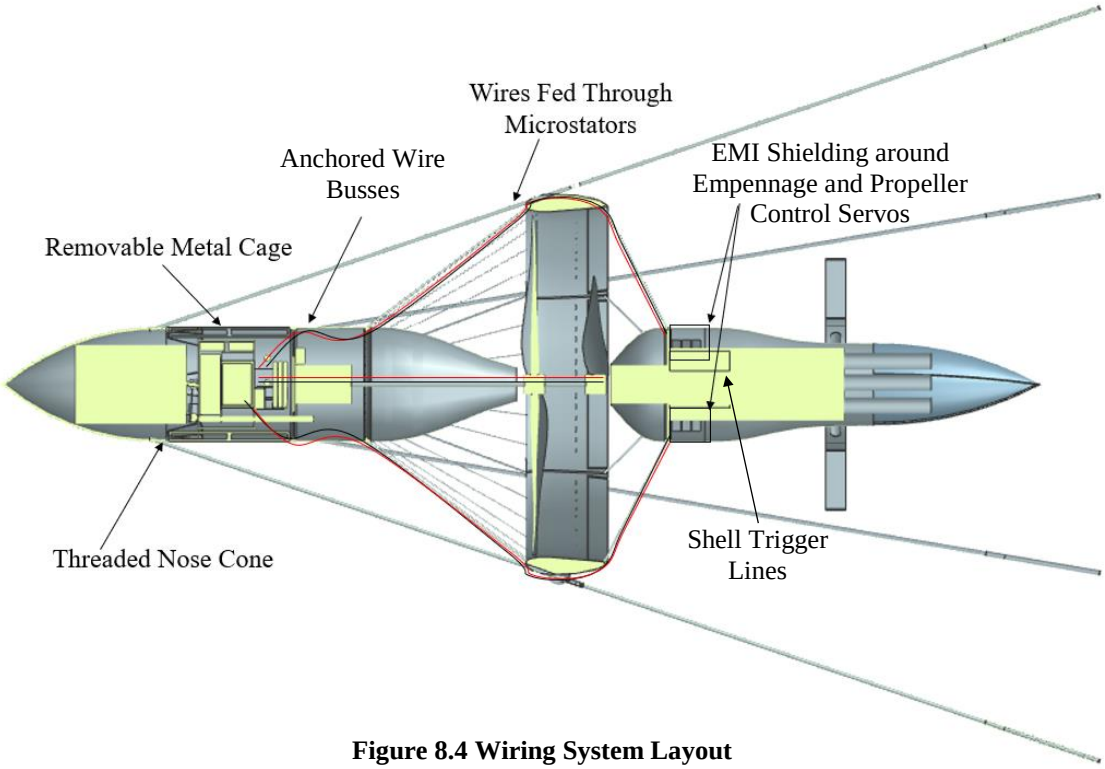

Figure 8.4 Wiring System Layout

8.2 Redundancy

As the missile is expected to perform in conditions which pose potential damage redundancy of the system is required to ensure optimal performance. Each grid fin has three servos connected to a common link, which creates redundancy and safety within the system. In the event of a servo failure, the other two servos in the chain will break the malfunctioning servo free from its mounting with opposed torque, resulting in no loss of control. In addition, each grid fin servo setup is individually wired and passes through a different microstator to the flight computer. This allows for increased safety as if one microstator were to be damaged, only one grid fin would be inoperable.

8.3 Wiring Block Diagram

The hovering missile utilizes a central flight computer to facilitate autopilot and data collection operations and to control the flight motor and servos via the ESC. This computer, as well as a data transmitter and receiver and their respective antennae, are powered by two dedicated FCS lithium-polymer batteries. These batteries also power the control servos and navigation systems (GPS &IMU).

The target acquisition sensors (AVS & cameras) and their respective transmitters and antennae are powered with a separate identical lithium-polymer battery. The flight computer analyzes the data from these sensors with recognition algorithms to track the target before transmitting information back to the pilot.

Six lithium thionyl-chloride battery packs consisting of 8 batteries in series power the main motors. The battery packs are arranged in parallel to extend the flight time duration. To prevent battery packs from charging one another, diodes have been added between each pack. There is a total of nine battery packs including the three FCS batteries. These connections are shown in Figure 8.5.

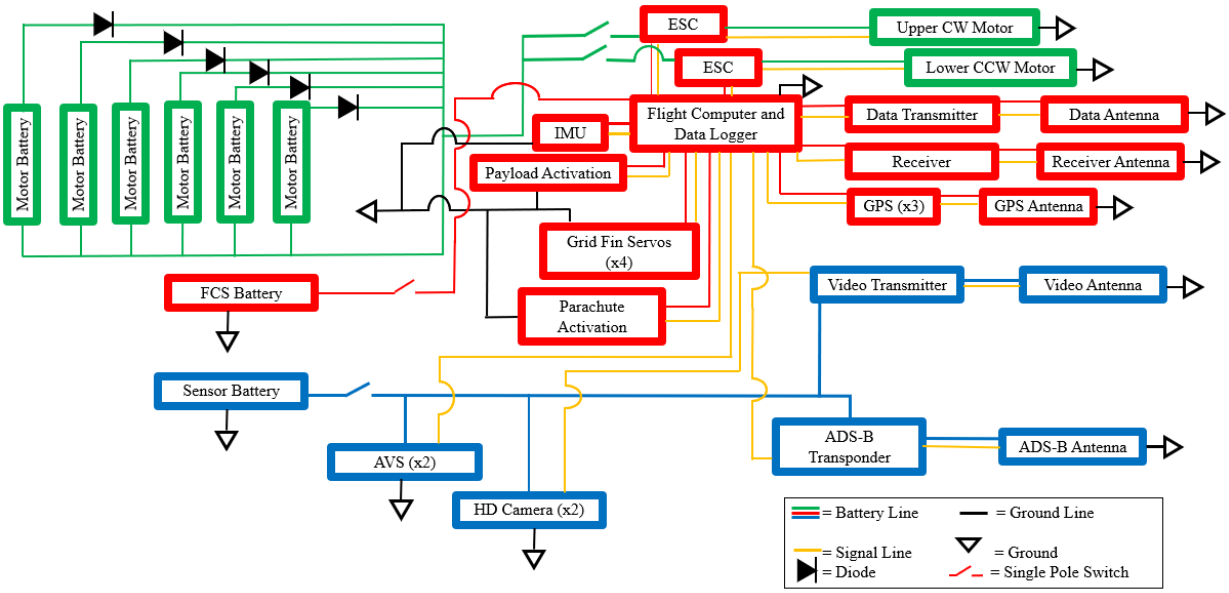

Figure 8.5: RHI*NO Wiring Block Diagram

8.4 Electric Load Summaries

The total energy required for each of the system groupings can be observed in Table 8.1. Table 8.2 displays the key characteristics of the batteries for each system. Based on the prescribed flight speeds and distances the total time of flight for the mission specification is 4.2 minutes or 250 seconds. A break down of time spent in each phase of flight can be observed in Table 8.3.

The electric power loads expected throughout each of the flight stages are presented in Table 8.3. The preflight values consider idle current draw of each component on their corresponding battery system. The components are grouped together in terms of power source. For example, the motors and ESC are to be powered by the main batteries while the sensors and control surfaces are each powered by a separate battery pack. This will ensure both battery packs are sized appropriately for the mission. Any value with multiple of that component displays the combined

power requirement. The servo calculations account for a 6V supply and all 15 servos operating at a stall current draw of 700 mA. The time through each of the stages was estimated based on flight speed and required travel distance. Multiplying the power required at each stage by the time in seconds the stage is expected to last results in the energy load in Joules, shown in Table 8.4**Error! Reference source not found.**. This value was then used to compare to the number of batteries required for the system.

Table 8.1 Total Energy Load Requirements

Total Energy Propulsion (kJ)	328
Total Energy FCS (kJ)	17
Total Energy Sensor (kJ)	4

Table 8.2 Battery Key Characteristics

	Capacity (mAh)	Voltage (V)	Weight (g)	Number in System	Watt Hours	Kilojoules
Motor Batteries	2600	3.6	19	84	790	2800
FCS Batteries	2500	3.7	29	2	18.5	66
Sensor Batteries	2500	3.7	29	1	9.25	33

Table 8.3: RHI*NO Electrical Power Summary for Battery Sizing

Electrical Load Item	**Preflight** 5 min(W)	**Takeoff** 10 sec (W)	**Climb** 65 sec (W)	**1st Engagement** 20 sec (W)	**2nd Engagement** 40 sec (W)	**Return** 90 sec (W)	**Landing** 20 sec (W)
YEP 100A SBEC Brushless Speed Controller	2.31	2.31	2.31	2.31	2.31	2.31	2.31
PROPDRIVE v2 5060 270KV Brushless Outrunner Motor FWD	0	910	593	920	920	593	910
PROPDRIVE v2 5060 270KV Brushless Outrunner Motor AFT	0	910	593	920	920	593	910
Total Propulsion	**2.31**	**1820**	**1190**	**1840**	**1840**	**1190**	**1820**
IMU (Inertial Measurement Unit) (Accelerometer/Gyro)	0.06	0.06	0.06	0.06	0.06	0.06	0.06
GPS X 3	0.11	0.11	0.11	0.11	0.11	0.11	0.11
Power Switch	0.02	0.02	0.02	0.02	0.02	0.02	0.02
Parachute Release Servo	0.72	0.72	0.72	0.72	0.72	0.72	0.72
Grid Fin Servos (all moving, gusty)	8.64	50.4	50.4	50.4	50.4	50.4	50.4
Propeller Pitch Sensors X 2	1.44	8.4	8.4	8.4	8.4	8.4	8.4
Total Flight Control	**11.0**	**59.7**	**59.7**	**59.7**	**59.7**	**59.7**	**59.7**
PU Match (AVS)	2.31	2.31	2.31	2.31	2.31	2.31	2.31
RunCam Nano HD	2.31	2.31	2.31	2.31	2.31	2.31	2.31
Transmitter (6 km)	1.2	1.2	1.2	1.2	1.2	1.2	1.2
Receiver (50 km)	1	1	1	1	1	1	1
Flight Computer MP2128 HELI	0.91	0.91	0.91	0.91	0.91	0.91	0.91
Total Sensor	**7.7**	**7.7**	**7.7**	**7.7**	**7.7**	**7.7**	**7.7**
Total Overall System Design	**34.0**	**3770**	**2500**	**3810**	**3810**	**2500**	**3770**

Table 8.4: RHI*NO Electrical Energy Summary for Battery Sizing

Electrical Load Item	Preflight 5 min(J)	Takeoff 10 sec (J)	Climb 65 sec (J)	1st Engagement 20 sec (J)	2nd Engagement 40 sec (J)	Return 90 sec (J)	Landing 20 sec (J)
YEP 100A SBEC Brushless Speed Controller	693	23.0	150	42.0	69.3	208	46.2
PROPDRIVE v2 5060 270KV Brushless Outrunner Motor FWD	0	9100	38550	16560	27600	53370	18200
PROPDRIVE v2 5060 270KV Brushless Outrunner Motor AFT	0	9100	38550	16560	27600	53370	18200
Total Propulsion	**693**	**18200**	**77240**	**33160**	**55270**	**107000**	**36450**
IMU (Inertial Measurement Unit) (Accelerometer/Gyro)	18	0.6	3.9	1.08	1.8	5.4	1.2
GPS X 3	32.4	1.08	7.02	1.94	3.24	9.72	2.16
Power Switch	6	0.2	1.3	0.36	0.6	1.8	0.4
Parachute Release Servo	216	7.2	46.8	13.0	21.6	64.8	14.4
Grid Fin Servos (all moving, gusty)	2592	504	3276	907	1512	4536	1008
Propeller Pitch Sensors X 2	432	84	546	151.2	252	756	168
Total Flight Control	**3296**	**597**	**3881**	**1075**	**1791**	**5374**	**1194**
PU Match (AVS)	693	23.1	151	42	69.3	208	46.2
RunCam Nano HD	693	23.1	151	42	69.3	208	46.2
Transmitter (6 km)	360	12	78	22	36	108	24
Receiver (50 km)	300	10	65	18	30	90	20
Flight Computer MP2128 HELI	273	9.1	59.2	16.4	27.3	81.9	18.2
Total Sensor	**2319**	**77.3**	**502.5**	**139.1**	**232**	**696**	**155**
Total Overall System Design	**6310**	**18900**	**81600**	**34380**	**57300**	**113000**	**37800**

8.5 General List of Components

Table 8.5 shows the general components used in the design of the RHI*NO. Many of these components are consumer off the shelf (COTS) and technology readiness level (TRL) 10.

Table 8.5: General Component List Description [51-60]

Component	Image	Dimensions (in)	Weight (g)	Weight (oz)
Kevlar (Fuselage and Rotor Guard)		Varies	Varies	Varies
Propeller Custom Made		Varies	Varies	Varies
Roll Servos (HF 5055 MG) X 12		0.89” x 0.45” x 0.94”	9.5	0.3
Propeller Pitch Sensors (HF 5055 MG) X 2		0.89” x 0.45” x 0.94”	9.5	0.3
Parachute Release Servo (HF 5055 MG)		0.89” x 0.45” x 0.94”	9.5	0.3
YEP 100A SBEC Brushless Speed Controller		2.36” x 1.57” x 0.78”	81	2.9
PROPDRIVE v2 5060 270KV Brushless Outrunner Motor		2.32” x 1.97” x 1.97”	438	15.4

Table 8.5: General Component List Description [51-60] Continued

Grid Fins		2.19” x 3.86”	77.1 / each	10.88 / each
Lithium Thionyl Chloride Batteries		1.32” x 1.32” x 2.41”	19	3.2
IMU (Inertial Measurement Unit) (Accelerometer/Gyro)		3” x 1.97” x 0.98”	45.4	1.6
GPS		1.18” x 1.18” x 0.4”	5	0.2
PU Match (AVS)		0.28” x 0.28” x 2.28”	5	0.2
RunCam Nano HD		0.71” x 0.55” x 0.55”	5	0.2
Power Switch		0.83” x 0.83” x 0.6”	5	0.2
Parachute		4" x 4” x 5.3"	283.5	10.0
Shotgun Shells X 6		2.4” x 0.75” x 0.75”	42.7 / each	1.5 / each
Transmitter (6 km)		2.7” x 1.4” x 1.1”	42	1.5
Receiver (50 km)		2.4” x 0.87” x 0.59”	6	0.2
Antenna		5.8”	6	0.2
ADS-B Transponder		0.47" x 0.98" x 1.54"	20	0.7
FCS Battery (33.3 kJ)		0.17" x 2.28" x 2.48"	29	1.0
Micro-Pilot FCS: MP2128^{HELI2}		3.94" x 1.57" x 0.59"	40	1.4
Kevlar Barrel x6		12” x 0.78" x 0.78”	16.1 / each	0.57 / each
Fith Ops Shotgun Shell Trigger		1” x1” x 3”	99.2 / each	3.50 / each

8.6 Weight and Balance

This section documents the weight and balance analysis of the RHI*NO design. As previously reported, the weight fraction of the propulsion system so the design could be possible was found to be 55% of W_{TO} for a 14.3-inch rotor diameter at 8 lbf. W_{TO}, while a 12 lbf. design is able to achieve a 55% W_{TO} for propulsion using a 17.4-inch rotor diameter, and a 16 lbf. W_{To} design is achieved with a 55% W_{TO} using a 20-inch rotor diameter. With these benchmarks for the sizing of the missile, other areas of the design had to sacrifice the amount of weight given to them. These categories are broken off into structure and fixed equipment, propulsion, SAS/coms/power package, and sensor/payload.

Table 8.6 displays the weight fractions of the RHI*NO for an 8, 12, and 16 lbf design. The titanium guard was estimated with weights based on Section 7.3 of this report. It should be noted light blue boxes indicate estimates made from using a linear trend between the XQ-138 11 inch and 24-inch designs, Ref. 61. Green boxes indicate achieved metrics, notably the % of W_{TO} used for propulsion and the overall design weight of the missile. Red boxes indicate metrics which were not obtained.

As an electronic motor is utilized instead of an internal combustion engine, therefore there is no trapped fuel and oil, and the weight of fuel is replaced by the weight of batteries. It was observed when determining the weight fractions for the 8 lbf design there was not enough payload weight to allow for the SkyNet shell payload to be present; the 8 lbf design is capable of ramming only.

The 12 lbf design is able to hold the SkyNet shell payload as well as 1.75 lbf of titanium armor covering the entire forward fuselage and rotor guard.

Table 8.6 Weight Fraction Calculations

	RHI*NO (14.3 in) 8 lbf			RHI*NO (17.4 in) 12 lbf			RHI*NO (20 in) 16 lbf		
	Weight (gmf)	Weight (oz)	Weight Fraction	Weight (gmf)	Weight (oz)	Weight Fraction	Weight (gmf)	Weight (oz)	Weight Fraction
Structure and Fixed Equipment	**1480**	**52.2**	**42.0**	**1560**	**55.0**	**28.1**	**1730**	**61.1**	**28.3**
Fuselage and Rotor Guard	150	5.28	4.3	202	7.1	3.6	272	9.6	4.9
Titanium Guard	198	7.0	5.6	225	7.9	4.1	328	11.6	5.9
Grid Fins	163	5.8	4.6	163	5.8	2.9	163	5.8	2.9
Pitch and Yaw Servos	118	4.16	3.3	118	4.2	2.1	118	4.2	2.1
Propeller Pitch Servos	18	0.63	0.5	18	0.6	0.3	18	0.6	0.3
Fasteners and Frames	136	4.80	3.9	136	4.8	2.4	136	4.8	2.4
Electronics Cage	32	1.1	0.9	32	1.1	0.6	32	1.1	0.6
Bulkheads	113	4	3.2	113	4	2.0	113	4	2.0
Landing Gear x 6	227	8.0	6.4	227	8.0	4.1	227	8.0	4.1
Ribs	32	1.1	0.9	32	1.1	0.6	32	1.1	0.6
Nose Cone	259	9.12	7.3	259	9.12	4.7	259	9.12	4.7
MicroStators	14	0.50	0.4	14	0.5	0.2	14	0.5	0.3
Mechanical and Electrical Connectors	20	0.72	0.6	20	0.7	0.4	20	0.7	0.4
Propulsion	**1430**	**50.4**	**40.6**	**2400**	**84.8**	**43.3**	**2800**	**98.9**	**45.7**
Propdrive Brushless Motor, YEP 100A ESC, Propellor	804	28.4	22.8	804	28.4	14.5	804	28.4	14.5
Batteries	625	22.0	17.7	1600	56.4	28.8	2000	70.5	36.0

Table 8.6 Weight Fraction Calculations Continued

SAS/Coms/Power Package	**204**	**7.2**	**5.8**	**204**	**7.2**	**3.7**	**204**	**7.2**	**3.3**
IMU (Accl+Gyro)	45	1.6	1.3	45	1.6	0.8	45	1.6	0.8
GPS X 3	15	0.5	0.4	15	0.5	0.3	15	0.5	0.3
Power Switch	5	0.16	0.1	5	0.2	0.1	5	0.2	0.1
Substrate and Connectors	9	0.30	0.2	9	0.3	0.2	9	0.3	0.2
Flight Computer	40	1.4	1.1	40	1.4	0.7	40	1.4	0.7
Flight Battery x 3	91	3.20	2.6	91	3.20	1.6	91	3.20	1.6
Transponder	18	0.64	0.5	18	0.64	0.3	18	0.64	0.3
Sensor/Payload	**410**	**14.5**	**11.6**	**1390**	**49.0**	**25.0**	**1390**	**49.0**	**22.7**
Camera (RunCam Nano HD) x 2	10	0.35	0.3	10	0.4	0.2	10	0.4	0.2
Acoustic Vector Sensors (Estimated) x 2	10	0.35	0.3	10	0.4	0.2	10	0.4	0.2
Pneumatic Net Gun (Trigger, Barrel)	0	0.00	0.0	725	25.6	13.0	725	25.6	13.0
Shot Gun Shell Weight X 6	0	0.00	0.0	254	9.0	4.6	254	9.0	4.6
Emergency Parachute	295	10.4	8.4	295	10.40	5.3	295	10.40	5.3
Receiver	5	0.16	0.1	5	0.16	0.1	5	0.16	0.1
Transmitter x 2	91	3.20	2.6	91	3.2	1.6	91	3.2	1.6
MGWTO (gmf,lbf,%)	**3520**	**7.77**	**100**	**5560**	**12.2**	**100**	**6130**	**13.5**	**100**

8.7 Center of Gravity Determination

Figure 8.6 and Figure 8.7 describe the internal layout of each component inside the hovering missile. With these locations and weight information known, it is possible to calculate the center of gravity (CG) for each component as well as the vehicle as a whole in three important conditions: empty weight (no batteries, payload, or parachute), operating empty (shells expended), and takeoff weight (batteries, parachute, and payload onboard). These CG locations are shown for each configuration in Figure 8.8. Note that the coordinate system origin is 10 inches forward of the tip of the nose.

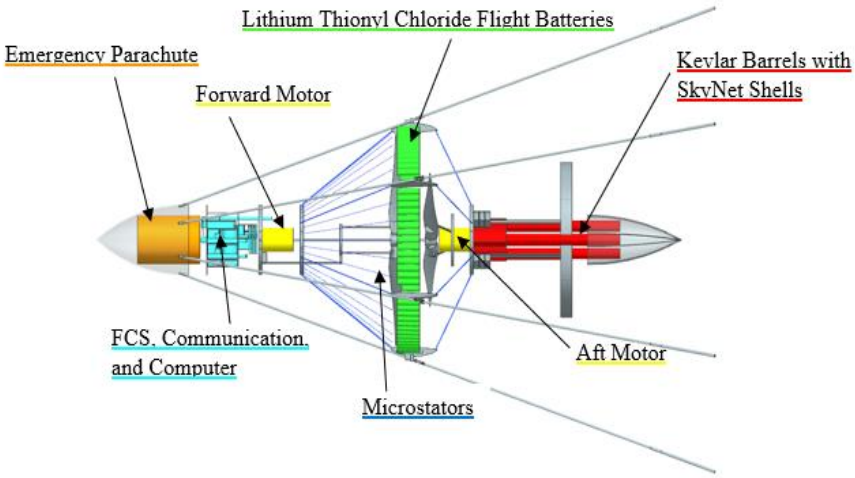

Figure 8.6 Internal Layout

The CG of the vehicle with full payload and batteries on board sits at 50% of the rotor guard chord, which is the location of the center of lift for a wing of this type. [62] This results in a static margin of 0 which maximizes maneuverability during interception. As the payload is expended, the CG shifts forward, increasing stability.

These CG locations are shown in relation to the percentage of the mean geometric chord in Figure 8.9 Figure 8.7 shows how the electronic components fit into the nose (see Figure 8.3 for details).

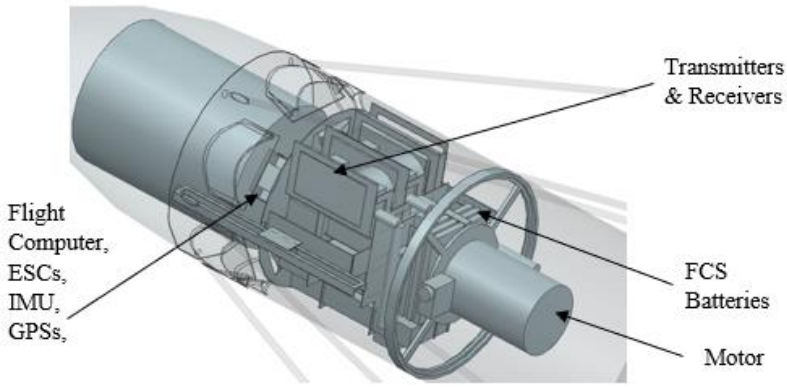

Figure 8.7: Nose Layout

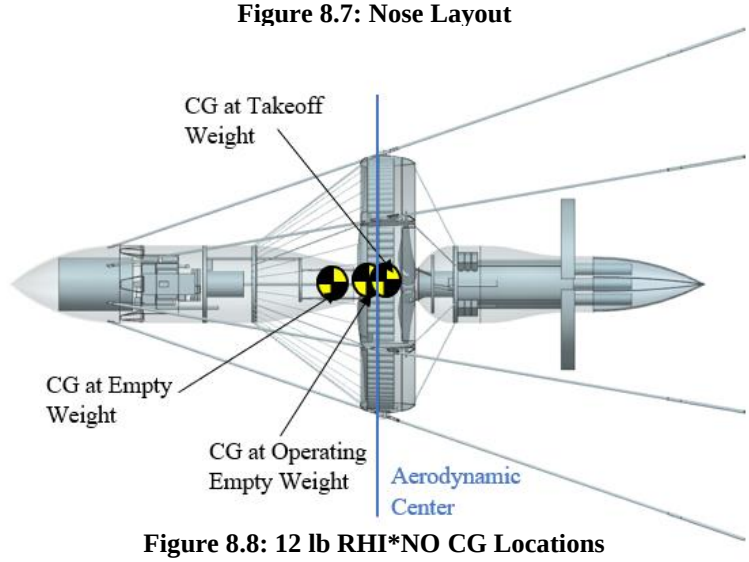

Figure 8.8: 12 lb RHI*NO CG Locations

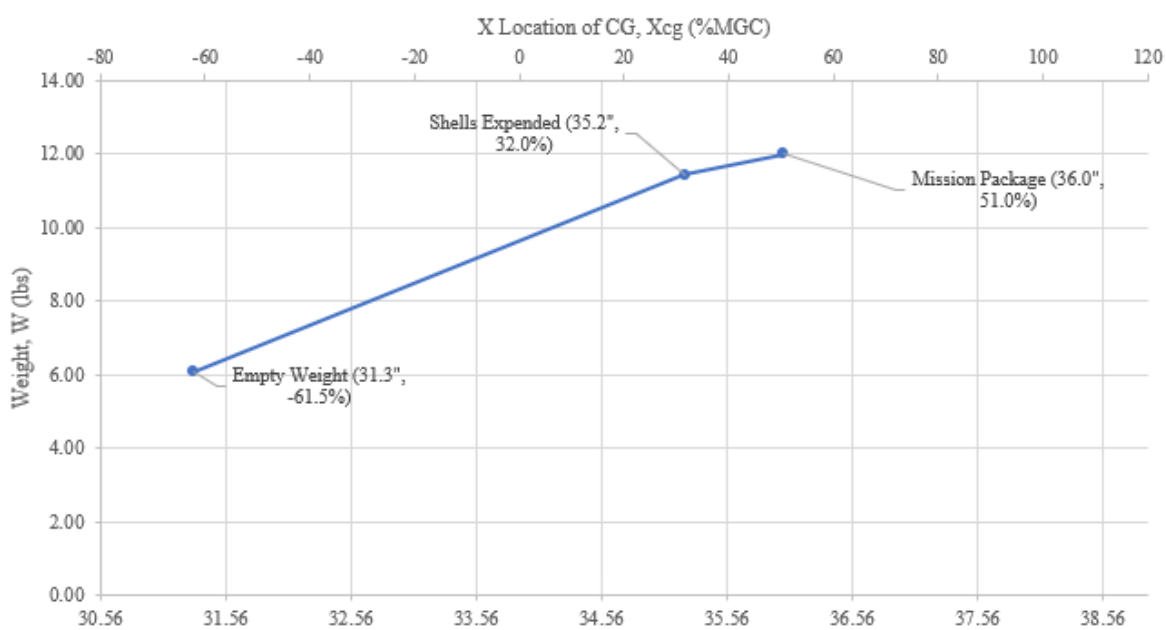

Figure 8.9: C.G. Excursion Plot

Table 8.7 provides the weight, weight fraction, and center of gravity location for each component of the hovering missile. Note that components which are patterned radially are given a distance from the centerline rather than a Y and Z position for an arbitrary unit. Note also that components distributed symmetrically in the Y and/or Z axes are shown with a ± symbol.

Table 8.7: 12 lb RHI*NO CG Component Breakdown

Component	Total Weight (lbs)	Xcg (in)	Ycg (in)	Zcg (in)	Weight Fraction (%)
STRUCTURE & FIXED EQUIPMENT	**3.12**	~	~	~	**26.00**
Nosecone	0.57	14.9	0.0	0.0	4.75
Forward Fuselage	0.20	22.7	0.0	0.0	1.67
Aft Fuselage	0.18	46.5	0.0	0.0	1.50
Rotor Guard	0.56	37.7	0.0	0.0	4.67
Grid Fin (x4)	0.36	51.5	±3.1	±3.2	3.00
Microstators (Total)	0.03	33.7	0.0	0.0	0.25
Ribs (x6)	0.07	38.0	9.1 From Center		0.58
Forward Bulkhead	0.07	24.5	0.0	0.0	0.58
Aft Firewall Bulkhead	0.15	43.1	0.0	0.0	1.25
Ring Frame Bulkhead	0.03	28.2	0.0	0.0	0.25
Landing Gear (x6)	0.50	44.0	11.9 From Center		4.17
FCS Cage/Parachute Springs	0.06	20.9	0.1	0.2	0.50
Grid Fin Servos (x12)	0.24	44.1 ± 0.5	±2.2	±2.2	2.00
Forward Prop Servo	0.02	24.8	-1.5	0.0	0.17
Aft Prop Servo	0.02	42.8	0.0	-1.5	0.17
Parachute Deployment Servo	0.02	19.5	1.4	-0.5	0.17
Grid Fin Servo Arm (x4)	0.03	47.4	1.9 From Center		0.25
Ballute	0.00	57.6	0.0	0.0	0.00
FUEL & POWERPLANT	**4.93**	~	~	~	**41.08**
Forward Motor	0.61	26.0	0.0	0.0	5.08
Forward Propeller & Actuator Assembly	0.09	36.5	0.0	0.0	0.75
Forward Motor Shaft	0.01	31.7	0.0	0.0	0.08
Aft Motor	0.61	41.7	0.0	0.0	5.08
Aft Propeller & Actuator Assembly	0.09	39.6	0.0	0.0	0.75
Flight Battery (x84)	3.52	37.6	9.1 From Center		29.33
SENSORS/FCS/COMS/POWER	**1.07**	~	~	~	**8.92**
AVS (x2)	0.02	37.9	±9.2	±0.4	0.17

Table 8.7: 12 lb RHI*NO CG Component Breakdown **Continued**

Camera (x2)	0.02	37.7	±9.7	±0.7	0.17
ESC (x2)	0.36	21.7	0.0	0.3 & -0.8	3.00
IMU	0.10	20.3	0.0	-0.4	0.83
Power Switch	0.01	21.4	0.0	-2.8	0.08
Flight Computer	0.09	21.8	0.0	-2.0	0.75
GPS 1	0.01	20.4	-1.9	0.1	0.08
GPS 2	0.01	21.9	-1.9	0.1	0.08
GPS 3	0.01	21.9	0.0	-1.4	0.08
Transmitter (x2)	0.19	21.5	0.1 & -1.1	1.2	1.58
Receiver	0.01	21.0	1.2	1.5	0.08
Receiver Antenna	0.01	22.7	1.7	0.0	0.08
FCS Battery (x3)	0.19	23.8 ± 0.2	0.0	0.0	1.58
ADS-B Transponder	0.04	22.8	0.7	0.0	0.33
PAYLOAD	**2.86**	**~**	**~**	**~**	**23.83**
Parachute	0.65	16.4	0.0	0.0	5.42
Generic Payload	2.21	47.6	0.0	0.0	18.42
OR					
Parachute	0.65	16.4	0.0	0.0	5.42
Barrel (x6)	0.33	51.2	0 & 1.3 From Center		2.75
Shell (x6)	0.56	47.5	0 & 1.3 From Center		4.67
Trigger (x6)	1.31	44.7	0 & 1.3 From Center		10.92
OPERATING EMPTY WEIGHT	**9.79**	**33.4**	**0.0**	**0.0**	**81.6**
TAKEOFF WEIGHT	**12.00**	**36.0**	**0.0**	**0.0**	**100.0**

8.8 Exploded View

An exploded view and breakdown of materials of the hovering missile is provided in Figure 8.10. Note that some recurring components (such as landing gear) are shown only once for clarity, and that all electronics are TRL 10 COTS products. Titanium armor is included with the rotor guard and fuselage parts and is not shown separately here.

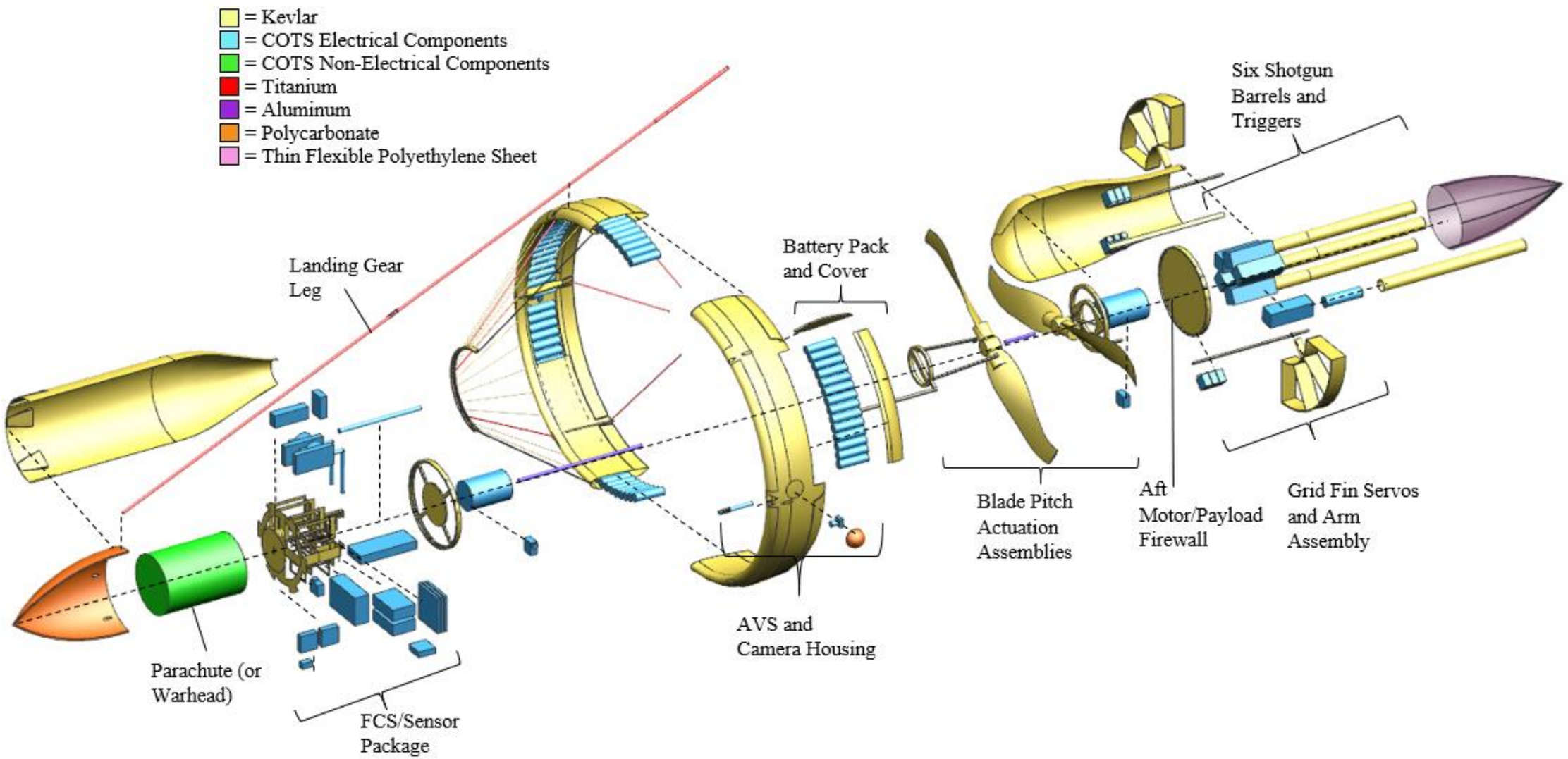

Figure 8.10: Exploded View and Material Break Down

8.9 Color Schemes

Figure 8.11 illustrates the advanced realistic CAD of the hovering missile with the primary color scheme.

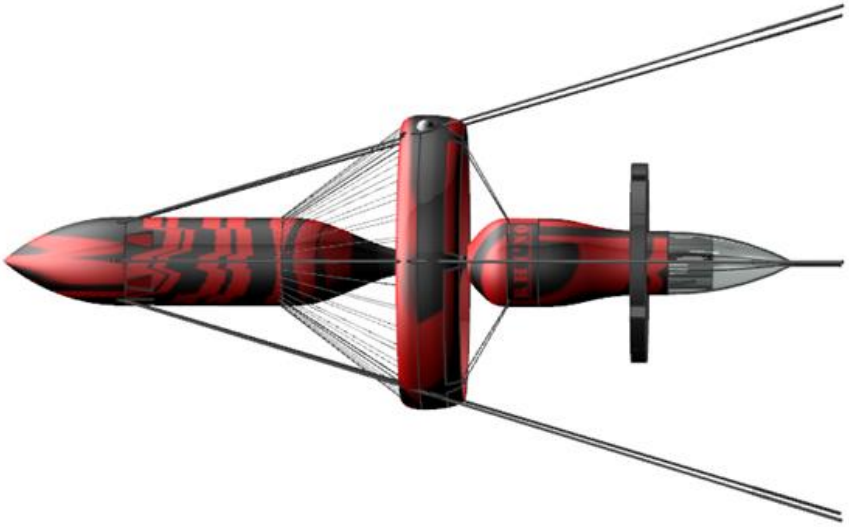

Figure 8.11 Hovering Missile Advanced CAD

Figure 8.12 provides alternative color schemes for the hovering missile appropriate for each branch of the United States military, as well as a night-operations scheme.

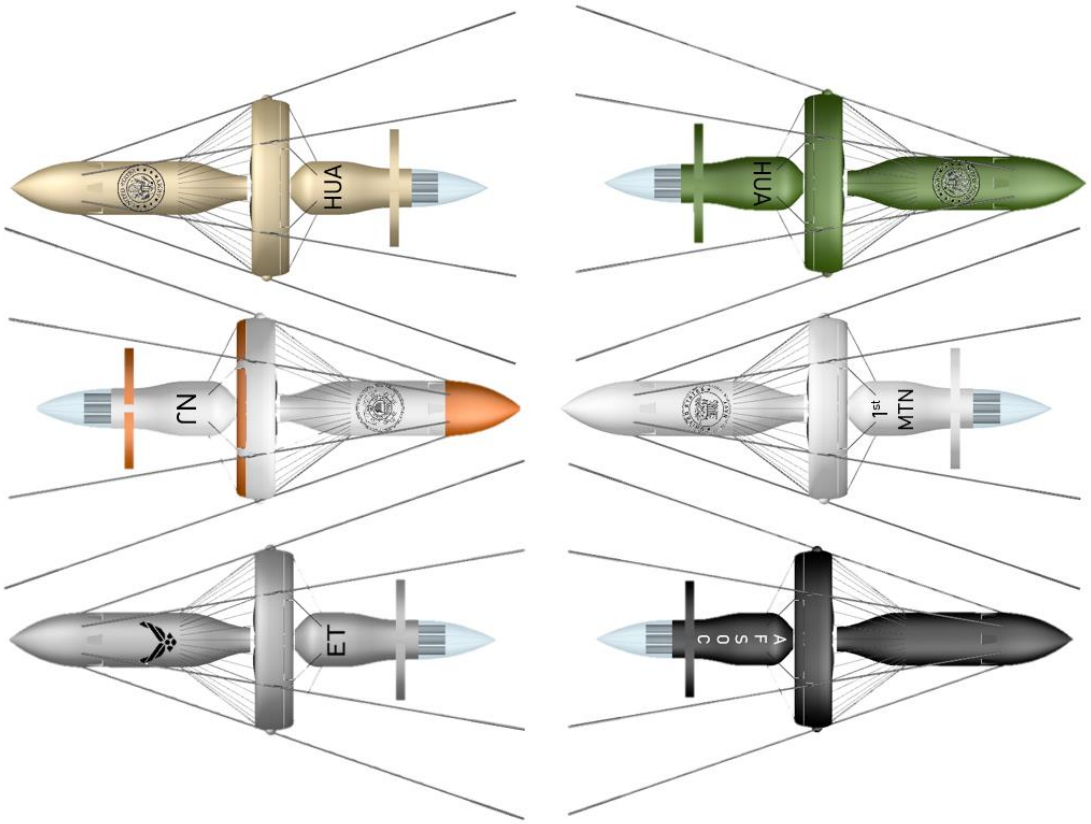

Figure 8.12 Alternate Color Schemes (Left Side Top to Bottom: Army (Desert), Coast Guard, Air Force), (Right Side Top to Bottom: Army (Olive Drab), Navy, (Night-Operation)

8.10 Packing

The RHI*NO is designed to disassemble into a single carrying case as shown in Figure 8.13. After removing the nosecone, ballute, landing gear, grid fins, and payload, it can be transported by a single individual to the desired launch location as shown in Figure 8.14. Because only three HMS systems are needed for any one mission to meet the 10 target interceptions per hour requirement, each of the three soldiers will carry one RHI*NO case and the ground station flight controller. This will weigh approximately 12 lb. for each RHI*NO and an additional 3 lb per unit. to account for the case and ground station flight controller. In addition, one soldier will carry the 15 lb Dedrone RF-160 system. This weight falls well within the maximum weight of 50 lb any one soldier is permitted to carry.

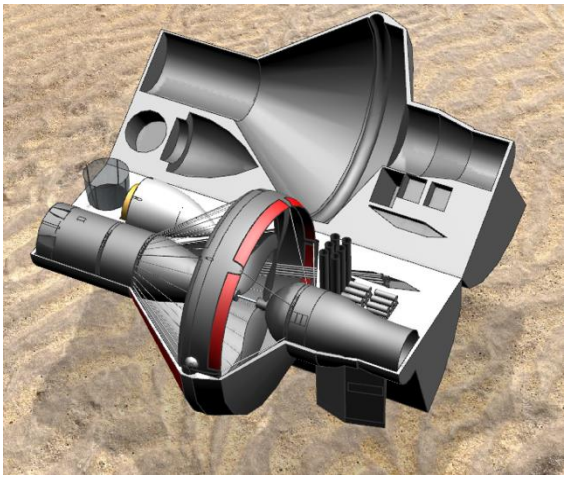

Figure 8.13: 12 lb RHI*NO Missile Disassembled in Carrying Case

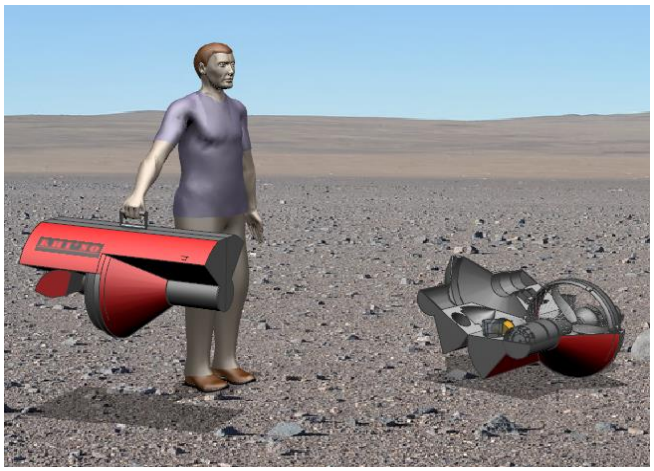

Figure 8.14: 12 lb RHI*NO Missile Carrying Case Size Illustration

Figure 8.15 provides a sizing reference for the 8. 12. And16 lb RHI*NO designs when being operated in the field; the female soldier is in the 20th percentile (5 feet and 2 inches tall) and the male soldier is in the 90th percentile (6 feet and 3 inches tall).

Figure 8.15: Relative RHI*NO Size Perspective Graphic [2, 63, 64]

8.11 Alternate Payload Viability

Despite the versatility of the RHI*NO in terms of its ability to ram or shoot down target drones with either a net or standard shotgun shell, the HFB-WEB team recognized the value of offering other payload options for consumers with different needs. While the base model of the RHI*NO is equipped with a shotgun payload, these other options, among others, can be designed more thoroughly and offered upon request.

8.11.1 Payload Range-Altitude Diagram

This section documents how the range of the HMS is influenced from the removal of payload and addition of batteries. Upon use of the already determined weight fuel fractions for batteries, the payload limit was determined. The corresponding range which can be achieved for the 8, 12, and 16 lb. designs are shown Figure 8.16. As the RHI*NO is capable of operation without additional interception techniques such as the SkyNet shells or emergency parachute, these weights are removed and replaced with more batteries. This increases the weight fraction of the propulsion system and thus the range the HMS can achieve. The graph is based on an alternative form of the Breguet range equation (Eq. 57) that is modified for electric power, as the batteries do not lose weight throughout flight [65]. Based on the current weight of batteries for the 12 lb. design the RHI*NO is capable of transporting a payload of 2.5 lb. for a range of 35 nmi.

$$R = \frac{c_b}{g} * \left(\frac{C_L}{C_D}\right) * \left(\frac{W_{batt}}{W_{TO}}\right) * \eta_{prop} \quad \textbf{(Eq. 57)}$$

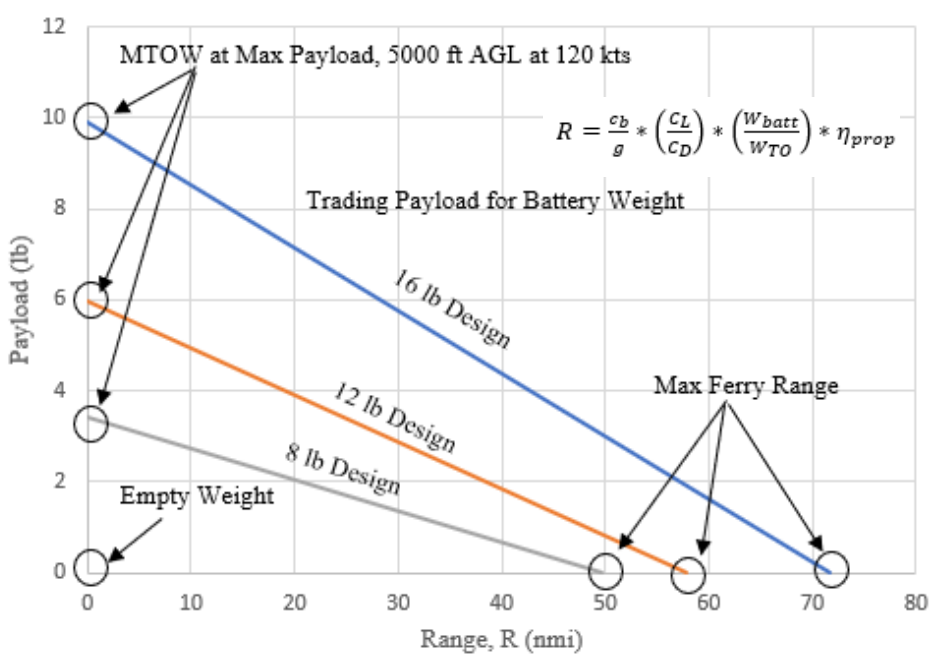

Figure 8.16 Payload vs Range For 8, 12, and 16 lb. Designs

8.11.2 Range Testing of Custom Shotgun Shell Solution

While the SkyNet shells offer a viable method of interception, a somewhat simpler strategy was investigated: packing Kevlar strands affixed to weights into a 12-gauge shotgun shell and firing in the direction of the target, with the intention that the long strands would tangle the rotors of the target. This strategy was tested with live ammunition, with strands made using different combinations of 1 and 2' long Kevlar strings tied to 0.2 g and 0.5 g weights and fired into a ballistic-gel target from 25 feet away, as shown in Figure 8.17. The test was performed at Platte Falls Conservation Area and Shooting Range in Platte County, Missouri. Each "net" was packed into an emptied 12-gauge shotgun shell along with additional standard shot to achieve the necessary shell mass of 32 g (the minimum at which the shell will fire).

During all seven Kevlar strand ballistics tests, the net failed to deploy as expected, hitting the target in a tangled mass regardless of how it was inserted into the shell, as shown in Figure 8.18. The Kevlar strands burned and frayed after firing, as shown in Figure 8.19. An eighth final test was performed using a standard shotgun shell for comparison which resulted in all targets being disabled and destroyed, as expected. Table 8.8 provides a summary of each test and what was learned. These tests suggest that standard shotgun shells or commercially proven SkyNet shells are more viable than a customized solution.

Figure 8.17: Shotgun Testing Setup

Figure 8.18 Wad of Kevlar Strands Embedded Within Target

Figure 8.19 Burned and Frayed Kevlar Strands

Table 8.8 Range Testing Summary

Fired from 25', Shell Mass = 32g (12-Gauge)				
Test #	**Strand Length (ft)**	**Strand Quantity**	**Weight Attached to Strand (g)**	**Packing Details**
1	1	10	0.2	Strands Stuffed in with Standard Shot on Top
2	1	10	0.2	Strands Wound in to Prevent Tangling, Standard Shot on Top
3	2	7	0.5	Strands Tied Together, Standard Shot Between Kevlar and Weight
4	1	N/A	N/A	Large Wad of Kevlar not Attached to Weights, Standard Shot on Top
5	1	10	0.5	Strands Stuffed in with Standard Shot Below
6	10	1	0.5	Strand Stuffed in with Standard Shot on Top
7	10	1	0.5	Strands Wound in to Prevent Tangling, Standard Shot on Top
8	N/A	N/A	N/A	Standard Shotgun Shell
Results: Kevlar Strands Consistently Failed to Untangle and Became Frayed and Burned After Firing				

8.11.3 Pneumatic Net Gun Weight Estimation

To determine the viability of a pneumatic net gun, its approximate weight was determined with the use of the published weight and diagonal width of the Delft DroneCatcher [15]. To approximate the weight of the drone component of the DroneCatcher, a linear diagonal width to weight relation was formed based on the diagonal width and weight of the DJI Inspire 2 and DJI Matrice 600 Pro, shown in Figure 8.20 and Figure 8.21 respectively. Using the available specifications for these two designs, a drone weight value of 11.2 pounds was interpolated for the quadcopter vehicle of the DroneCatcher. This weight was subtracted from the total weight of around 13.2 pounds to find the approximate pneumatic net gun payload weight of 2 pounds [66, 67]. This weight includes not only the net gun, but also any net capsules, attachment structure, or miscellaneous weights which would not be found in a typical camera-carrying quadcopter.

Figure 8.20 DJI Inspire 2 [66]

Figure 8.21 DJI Matrice 600 Pro [67]

9. Class I Stability and Control Analysis

To analyze the stability and control characteristics of the HMS, the RHI*NO design was input into Advanced Aircraft Analysis (AAA). It should be noted prior to discussion that AAA possesses no way of modeling a ring wing design, and therefore, some error is expected. To input what AAA would interpret as an equivalent lifting surface,

Table 9.1: L/D Comparison	
Method	L/D Value at Dash Condition
Estimation	5.37
AAA	7.53
Error (%)	28.7

the ring wing was modeled as a monoplane with anhedral. Because the grid fins could not be modeled accurately either, they were instead modeled as a vertical stabilizer crossed with a horizontal stabilizer, each with a 5:1 aspect ratio. Upon entry of the design geometry, the flight conditions were specified as well. For this analysis, the dash condition at 250 kts was performed. The percent error between the estimated lift-to-drag ratio (L/D) and the calculated value from AAA is presented in Table 9.1. Because the L/D output by AAA was larger than expected, the required amount of thrust required for the dash condition was reduced, thereby decreasing the required thrust from the propulsion system.

AAA is also capable of calculating stability and control derivatives. Key stability derivatives were chosen and are presented in Figure 9.2, Figure 9.1, and Figure 9.3. Three key longitudinal stability derivatives will be discussed first, followed by three lateral stability derivatives. Starting with $C_{D\alpha}$, it has been calculated to be 0.334 rad^{-1}. Roskam states in his stability and control textbook [68], that the appropriate range for this derivative is between 0 rad^{-1} and 2.00 rad^{-1}. This value is on the lower end since the aircraft being analyzed has small. The second derivative to discuss is $C_{L\alpha}$; the appropriate range for this coefficient is between 1.00 rad^{-1} and 8.00 rad^{-1} [68]. The value calculated came out to be 3.43 rad^{-1}, which falls into the defined range. $C_{L\alpha}$ should be greater than $C_{D\alpha}$, because if it were not, the aircraft performance would decrease significantly as angle of attack increased. The final longitudinal derivative to discuss is $C_{M\alpha}$, which was calculated to be -0.886 rad^{-1}. This coefficient should be negative to provide a restoring pitching moment [68]. This makes sense for post-interdiction flight, as high maneuverability associated with lower stability would be unnecessary. Dr. Roskam defines the appropriate range for this coefficient between 1.00 rad^{-1} and -4.00 rad^{-1} [68]. Since the RHI*NO is designed to be an acrobatic aircraft, it makes sense that while there is a restoring pitching moment, it is not extreme. This allows it to still be maneuverable while still being manageable to fly.

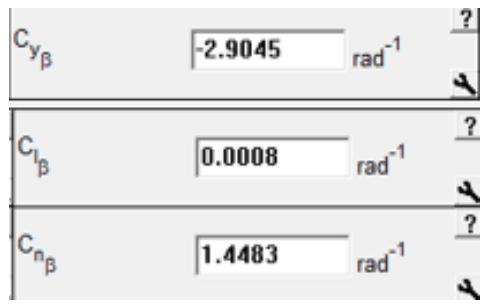

Figure 9.1: Lateral Stability Derivatives From AAA

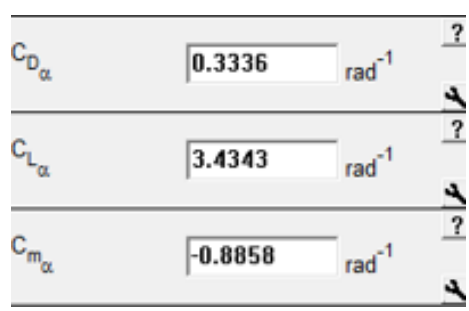

Figure 9.2: Stability Derivatives From AAA

Next up are the lateral stability derivatives, the first being the side-force coefficient with respect to sideslip, $C_{y\beta}$. $C_{y\beta}$ can be seen to

have a value of -2.90 rad^{-1}. This is usually negative, so the value found corresponds with expectations [68]. To counteract this and keep the aircraft on the desired trajectory, $C_{y\beta}$ is negative to push the aircraft back against this desired direction. Dr. Roskam defines the acceptable range of this coefficient to be between -0.10 rad^{-1} and -2.0 rad^{-1} [68]. The reason this value is on the larger side is because the vertical tail, the AAA approximation of the top and bottom grid fins, is near the size of the ring wing, so the vertical tail will have a large impact on the design. Next, the rolling coefficient due to sideslip, $C_{l\beta}$, was found to be 0.0008 rad^{-1}. The appropriate range for this coefficient is between 0.10 rad^{-1} and -0.40 rad^{-1} [68]. The relatively small value for this coefficient is expected due to the symmetry of the aircraft since the RHI*NO is radially symmetric. The final lateral stability derivative, $C_{n\beta}$, was calculated to be 1.45 rad^{-1}. This is a positive value and will help the aircraft should it turn into the direction the sideslip is coming from. If $C_{n\beta}$ were negative, it would not allow the aircraft to turn into the gust like it should. The range for this coefficient is given to be 0 rad^{-1} to 0.40 rad^{-1} [68]. $C_{n\beta}$ exceeds this range due to the relatively comparable size of the vertical tail and ring wing.

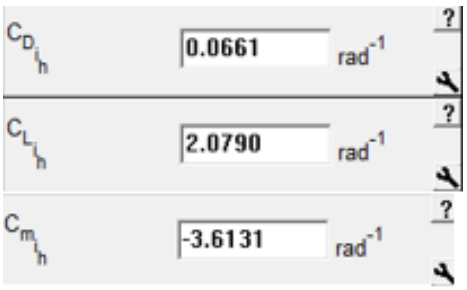

Figure 9.3: Control Surface Derivatives From AAA

For this design, control is maintained using the grid fins and setting their incidence. Control is reflected through the horizontal and vertical tail incidences. Both C_{Dih} and C_{Lih} are positive, with values of 0.0661 rad^{-1} and 2.08 rad^{-1} respectively. Roskam outlines that both these values should be positive [68]. The final control derivative of C_{mih} is -3.61 rad^{-1}, which is appropriate, as Roskam states that this derivative should be negative [68].

Dutch roll, spiral, and roll modes are also able to be calculated with this software. A linear time invariant model, LTI was developed for the RHI*NO while in cruise condition. The Dutch roll and spiral modes are displayed in Table 9.2. These values are noted to be stable.

Table 9.2: Modal Analysis of the RHI*NO

Mode	Stability	Damping	Frequency (Hz)
Dutch Roll	Stable	0.162	69.1
Phugoid	Stable	0.33	19.1
Short Period	Stable	N/A	N/A

10. Structural Analysis

The worst-case scenario during impact involves a 55-pound class 2 UAV flying at 250 knots impacting the 12-pound 250 knot hovering missile head-on. While the RHI*NO is capable of engaging up to class 5 UAVs as shown in Section 13.1 it is not expected to do so via ramming. Ramming targets larger than class 2 is feasible, but the HMS will not be re-usable. The loads experienced in this situation can be roughly approximated with a point-mass analysis. Using equations:

$$m_1 v_1 + m_2 v_2 = m_1 v'_1 + m_2 v'_2 \quad \textbf{(Eq. 58)}$$

$$v_1 + v'_1 = v_2 + v'_2 \quad \textbf{(Eq. 59)}$$

where m_1 is the mass of the hovering missile (in slugs), v_1 is the velocity in feet per second, and v'_1 is the velocity after the collision (with subscripts 2 corresponding to those quantities for the target), the final velocity of the hovering missile can be solved as:

$$v'_1 = \frac{m_1 v_1 + 2 m_2 v_2 - m_2 v_1}{m_1 + m_2} = \frac{\left(0.37\ slug * 422\frac{f}{s}\right) + 2\left(1.71\ slug * -422\frac{f}{s}\right) - \left(1.71\ slug * 422\frac{f}{s}\right)}{0.37\ slug + 1.71\ slug} = -966\frac{f}{s} \quad \textbf{(Eq. 60)}$$

If the impact is assumed to occur over 1/100th of a second, the acceleration experienced by the hovering missile is then:

$$-966\frac{f}{s} / 0.01\ s = -96600\frac{f}{s^2} \quad \textbf{(Eq. 61)}$$

The force imparted on the missile is this acceleration multiplied by the mass:

$$F = m * |a| = 0.37\ slug * 96600\frac{f}{s^2} = 35700\ lbf \quad \textbf{(Eq. 62)}$$

This force will be divided into seven parts: the forward section of the fuselage will counteract a force equal to its momentum change, and the rest will be divided among the six landing gear struts as shown in Figure 10.1

With the acceleration of the forward fuselage section already known, the momentum can be calculated by summing the masses of each component inside. This summation is provided in Table 10.1. Note that the forward motor and pitch-variation servos are not included as they are behind the microstators, which act as a second set of struts to divert the impact force.

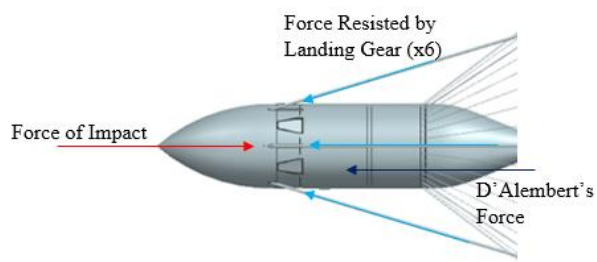

Figure 10.1: Impact Force Distribution

The impact force resisted by the momentum of the forward fuselage (D'Alembert's force) is then:

$$F = m * |a| = 0.037\ slug * 96600\frac{f}{s^2} = 3570\ lbf \quad \textbf{(Eq. 63)}$$

with the remaining force resisted by the landing gear struts:

$$F = \frac{Total\ F - F\ Resisted\ by\ Fuselage}{6} = \frac{35700\ lbs - 3570\ lbs}{6} = 5360\ lbf\ per\ landing\ gear\ leg \quad \textbf{(Eq. 64)}$$

The stress experienced by the fuselage tube can be calculated by dividing the force over the area:

Table 10.1: Forward Fuselage Weight Summation

Component	Weight (lbf)
Fuselage Tube	0.29
Titanium Armor	0.12
Flight Computer	0.09
Power Switch	0.01
IMU	0.10
GPS (x3)	0.03
Receiver Box	0.01
Receiver Antenna	0.01
Transmitter (x2)	0.19
ADS-B Transponder	0.04
ESC	0.18
FCS Battery (x2)	0.12
Total	**1.19 lbf = 0.037 slugs**

$$\sigma = \frac{F}{\pi(\frac{D}{2})^2 - \pi(\frac{d}{2})^2} = \frac{3570\ lbs}{\pi(\frac{5.8\ in}{2})^2 - \pi(\frac{5.764\ in}{2})^2} = 10900\ psi \qquad \textbf{(Eq. 65)}$$

where D and d represent the outer and inner fuselage diameters, respectively. During a head-on impact, the primary failure mode of the fuselage tube will be buckling. The following formula can be used to determine the maximum length of a column before buckling:

$$\sigma = \frac{\pi^2 EI}{(KL)^2} \rightarrow L = \frac{\sqrt{\frac{\pi^2 EI}{\sigma}}}{K} \qquad \textbf{(Eq. 66)}$$

where E is the elastic modulus of Kevlar in compression, I is the moment of inertia of the fuselage cross section, and K is the end fixity coefficient. K can be approximated as 2, which reflects a column fixed at one end, by the support from the microstators. E is given as 4.6 Msi in compression [69], and I for a tube can be calculated as:

$$I = \frac{\pi(D^4 - d^4)}{64} = \frac{\pi(5.8\ in^4 - 5.764\ in^4)}{64} = 1.366\ in^4 \qquad \textbf{(Eq. 67)}$$

Using Equation 68, the critical length of the forward fuselage tube to resist buckling is then:

$$L = \frac{\sqrt{\frac{\pi^2 EI}{\sigma}}}{K} = \frac{\sqrt{\frac{\pi^2 * 4600000\ psi * 1.366\ in^4}{10900\ psi}}}{2} = 37.7\ in \qquad \textbf{(Eq. 68)}$$

This length is longer than the specified forward fuselage tube length, meaning that no bulkheads or structural reinforcements are required to resist buckling during a ramming maneuver. Note that this analysis neglects the further buckling resistance added by the internal rails on which the flight control systems will be installed.

11. Aerodynamic Analysis

The following section details the drag polar and CFD analyses.

11.1 Drag Polar Analysis

The wetted areas of the hovering missile can be approximated with the use of the following equations:

Fuselage (Tube and Cone):

$$S_{Wet_{Fuselage}} = (2\pi r_f * h_f) + \pi r_f \left(r_f + \sqrt{h_{nc}^2 + r_f^2}\right) \qquad \textbf{(Eq. 69)}$$

Rotor Guard (Elliptical Torus and Sphere):

$$S_{Wet_{RotorGuard}} = \left(2\pi \sqrt{\frac{{a_{rg}}^2 + {b_{rg}}^2}{2}}\right) * (2\pi * r_{rg}) + (4\pi * {r_c}^2) \qquad \textbf{(Eq. 70)}$$

Grid Fins:

$$S_{Wet_{GridFins}} = (2\pi * r_{gf_o} * 2 * t_{gf}) + (2\pi * r_{gf_i} * 2 * t_{gf}) + (16 * 2 * t_{gf} * w_f) + (4 * 2\pi * r_{fa} * l_{fa}) \qquad \textbf{(Eq. 71)}$$

Microstators (Ellipse):

$$S_{Wet_{Microstator}} = (2\pi * \sqrt{\frac{{a_m}^2 + {b_m}^2}{2}}) * l_m * 56 \qquad \textbf{(Eq. 72)}$$

Landing Gear (Tubes):

$$S_{Wet_{LandingGear}} = 6 * l_{lg} * (2\pi r_{lg}) \qquad \textbf{(Eq. 73)}$$

In the above equations, r_f is the radius of the fuselage, h_f is the height of the cylindrical fuselage, h_{nc} is the height of the nosecone, a_m and b_m are the semimajor and semi minor axes of the microstators, respectively, l_m is the length of the microstators, l_{lg} is the length of the landing gear, r_{lg} is the radius of the landing gear, r_{gfo} is the outer radius of the grid fins, r_{gfi} is the inner radius of the grid fins, t_{gf} is the thickness of the grid fins, w_f is the width of the fin segments, r_{fa} is the radius of the fin actuator arm, l_{fa} is the length of the fin actuator arm, a_g and b_g are the semimajor and semi minor axes of the rotor guard ellipse, respectively, r_{rg} is the radius of the rotor guard, and r_c is the radius of the hemisphere-shaped camera shields. These wetted areas are compared to those calculated from the CAD models in Table 11.1; because each of the CAD calculations are verified to be within 10% of the hand calculations, the CAD calculations are assumed to be more accurate. It is possible to extrapolate the equivalent parasite area f as 0.036 ft^2 with a skin friction coefficient of 0.003 using Ref. 70.

Table 11.1: Wetted Area Calculations Verified by CAD Model

Part	Hand-Calculated Area (in^2)	CAD-Calculated Area (in^2)	Error (%)
Fuselage	743.4	745.4	0.3
Microstators	152.7	160.9	5.4
Landing Gear	151.3	151.3	0
Grid Fins	212.7	226.0	6.3
Rotor Guard	553.6	502.9	9.2
TOTAL	**1813.7**	**1786.5 (12 ft^2)**	**2.5**

From this value, the zero lift drag coefficient (C_{D0}) can be calculated as 0.034 by using equation 74, where S is double the value of the duct diameter multiplied by the rotor guard chord. To show why the design has a ballute, the value of C_D is plotted for the design with and without a ballute. C_{D0} increases twofold to 0.068 without a ballute. Alternatively, AAA defines the zero lift drag coefficient as 0.15. Each of these estimated coefficients, with the use of equation 75, are graphically represented in Figure 11.1.

$$C_{D_0} = \frac{f}{S} \qquad \textbf{(Eq. 74)}$$

$$C_D = C_{D_0} + \frac{C_L^2}{\pi A e} \qquad \textbf{(Eq. 75)}$$

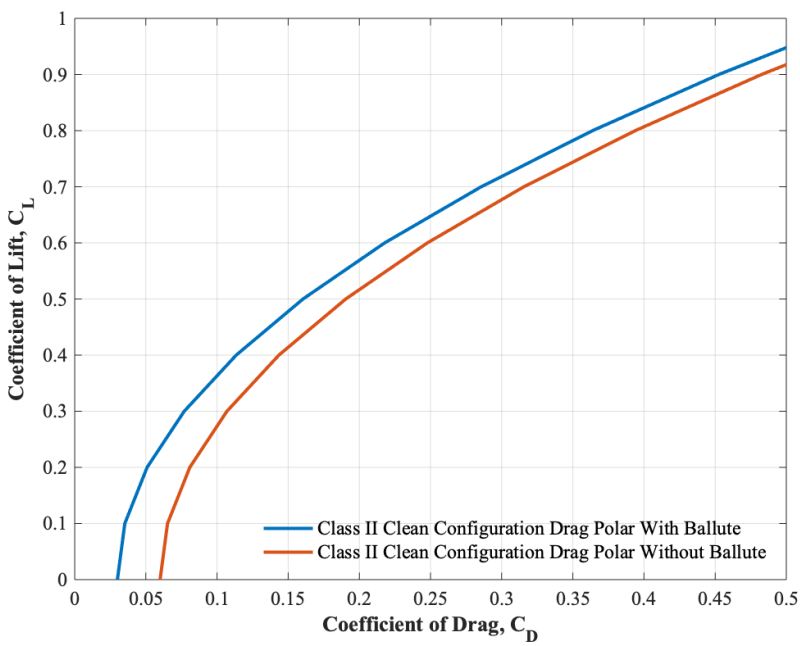

Figure 11.1: Drag Polars for 12 lb. HMS

11.2 CFD Analysis

The following section covers the model characteristics, verification, and results of the HMS CFD analysis.

11.2.1 Geometry

A simplified model of the hovering missile was analyzed with Siemens STAR CCM+ software to better visualize the aerodynamics of the aircraft. This model includes the primary structure comprising of the forward and aft fuselages, rotor guard, nosecone, ballute, and landing gear, while omitting the microstators, inlets, and finer details of the landing gear to keep the mesh at a workable size. The propellers are modeled as virtual disks through which air accelerates and have no physical model. Figure 11.2 provides an isometric view of the geometry in question.

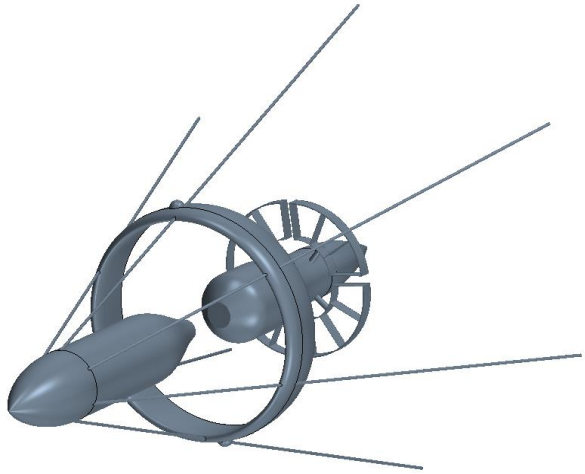

Figure 11.2 Solid Bodies for CFD Analysis

This geometry sits at the center of a cube-shaped region, with each side at a distance of ten times the length of the vehicle from the center. This scale is best illustrated with the mesh in the following subsection. The solid bodies were subtracted from this cube region to create the control volume through which air may flow.

11.2.2 Mesh Characteristics

A mesh operation utilizing the built-in surface repair and remeshing functionalities was executed on the control volume as described above. This mesh used polyhedral cells with a target base size of 0.01 meters (0.03 ft) and fifteen prism layers (near wall thickness = 3.5E-6 m) projecting from every solid surface at a total thickness of 50% of the base size to capture the boundary layer. Custom base sizes were applied to several areas of interest as described in Table 11.2

Table 11.2: Base Size Variations

Surface/Volume	Base Size (%)	Justification
General Volume	100	~
Nosecone, Rotor Guard Leading Edge and Ballute Surface	20	Primary Stagnation and Expansion Zones
Control Volume Boundary Surfaces	15,000	Away from Area of Interest

The resulting mesh contained 6,550,688 cells with over 32 million faces. Figure 11.3 through Figure 11.6 show the mesh at the surface of several points of interest, and Figure 11.7 and Figure 11.8 show the mesh volume around key points as well as the control volume as a whole.

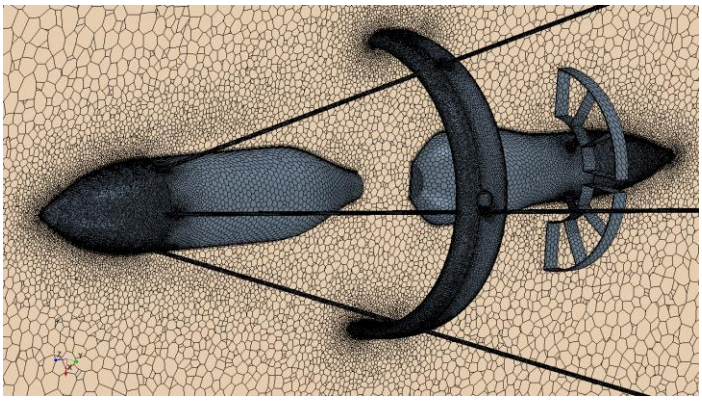

Figure 11.3: Surface and Volume Mesh

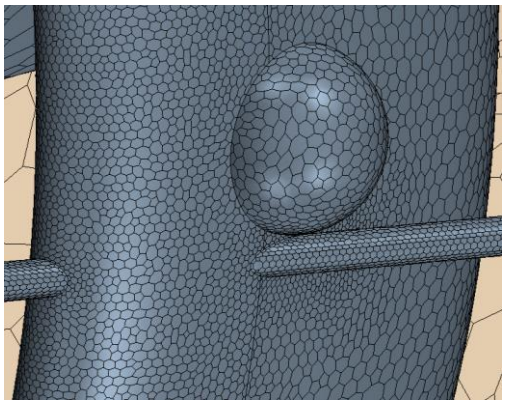

Figure 11.4: Surface Mesh at Landing Gear Intersection

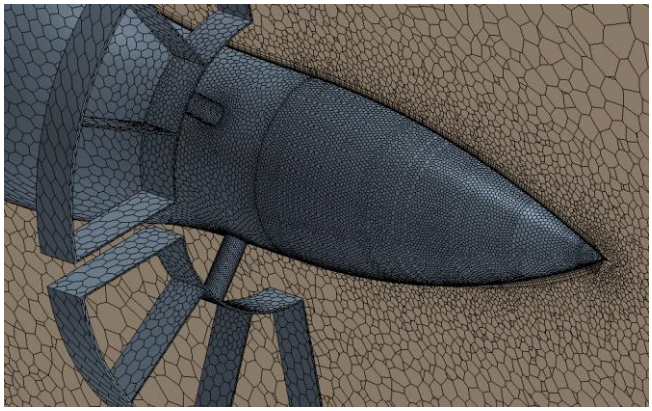

Figure 11.5: Surface Mesh and Prism Layers at Ballute and Grid Fins

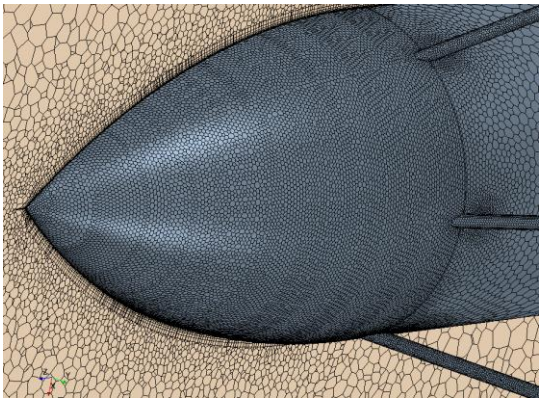

Figure 11.6: Surface Mesh and Prism Layers at Nosecone

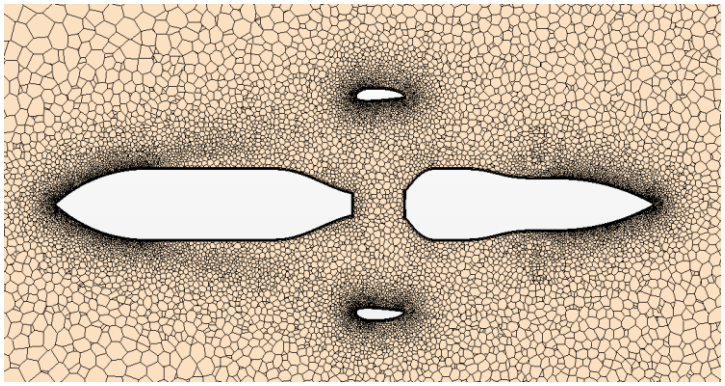

Figure 11.7: Volume Mesh Around Vehicle Area

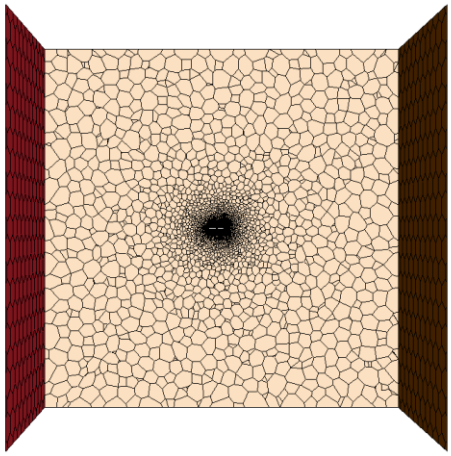

Figure 11.8: Total Volume Mesh

11.2.3 Physics Models and Conditions

The physics models used in this simulation are shown in Figure 11.9 and reflect the steady flow of air as an ideal gas at a reference pressure of 12.16 psi (expected at 5000 feet altitude) and 250 knots. Second order Spalart-

Allmaras turbulence was used, and no initial conditions were specified. The control volume velocity inlet was set at a velocity of 250 knots and three degrees angle of attack. The outlet was set as a pressure outlet, and the other surfaces of the control volume were modeled as symmetry planes to prevent interference with the flow.

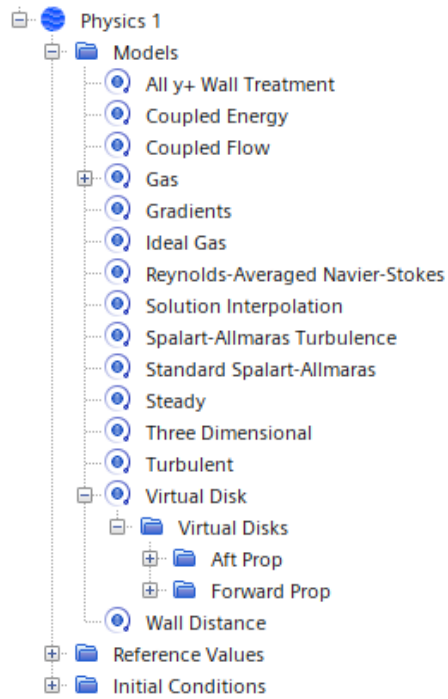

Figure 11.9 Physics Conditions

The propellers were modeled as two virtual disks each with an rpm of 9290 and spinning in opposing directions. Since the exact geometry and characteristics of the propeller used with the hovering missile are not easily defined, arbitrary (but realistic) coefficients are used in a polynomial to define the propeller curve and thrust distributed according to Goldstein's optimum distribution. The locations of the virtual disks are shown in Figure 11.10.

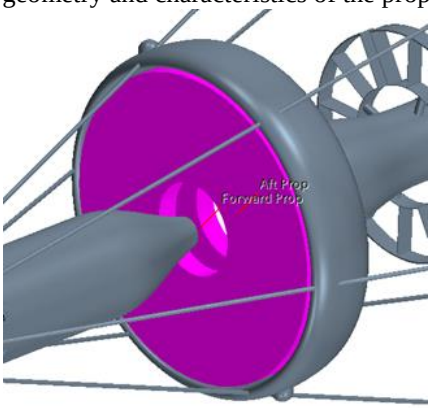

Figure 11.10 Virtual Disk Propellers

11.2.4 Verification

As shown in Figure 11.11, the wall Y+ values are at or below one almost everywhere on the surface (optimal for this turbulence model), suggesting very high reliability in results. Although this is a simplified model which ignores the impact of the microstators and approximates the propellers, it was determined that these results are trustworthy enough for a comparison to expected aerodynamic values.

The residual values are shown in Figure 11.12. This simulation was started with a second order turbulence model until convergence (830 iterations), then the angle of attack of three degrees was implemented. After a mistake was realized and corrected at 1200 iterations, the model ran to

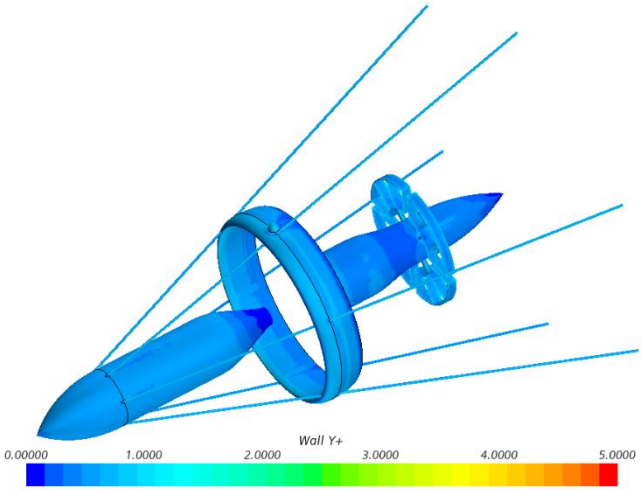

Figure 11.11: Wall Y+ Distribution

convergence at 2000 iterations. Note that while the turbulence residual converges below only 1E-03, the continuity, momentum, and energy residuals all lie firmly below 1E-05.

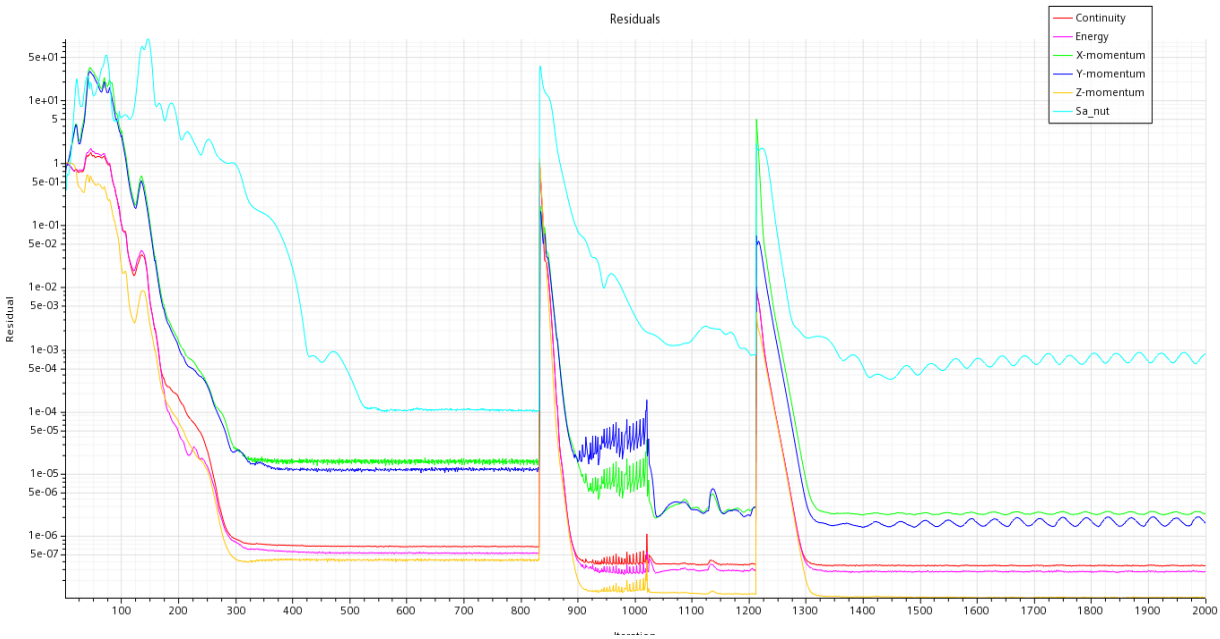

Figure 11.12: Residuals Plot

11.2.5 Results and Analysis

Figure 11.13 through Figure 11.17 provide illustrations of the pressure distribution on the surface of the hovering missile, as well as the pressure and velocity changes of the surrounding air while travelling at 250 knots. Note that the highest and lowest surface pressures occur at the leading and trailing edges of the grid fins. This is expected and optimal, since a higher pressure here equates to more powerful flight control. The center of pressure was calculated to be 27.6 inches aft of the tip of the nosecone, as shown in Figure 11.18.

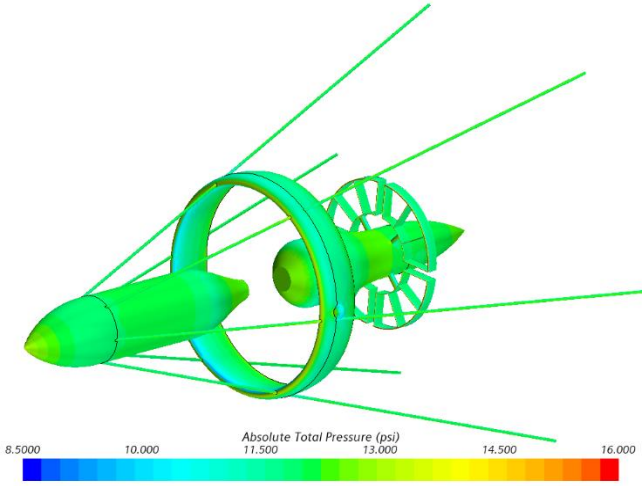

Figure 11.13: Absolute Pressure Distribution

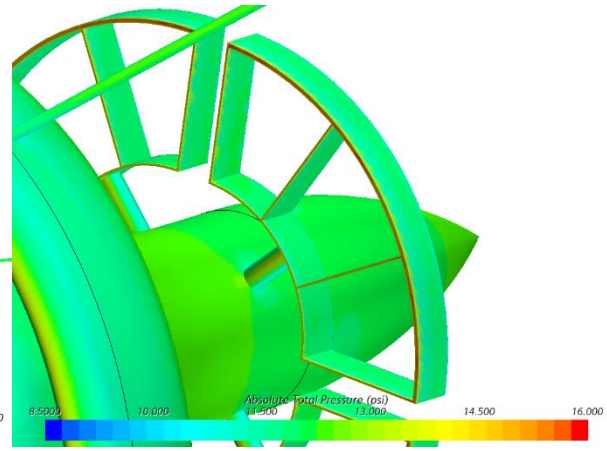

Figure 11.14: Absolute Pressure Distribution in Area of Interest

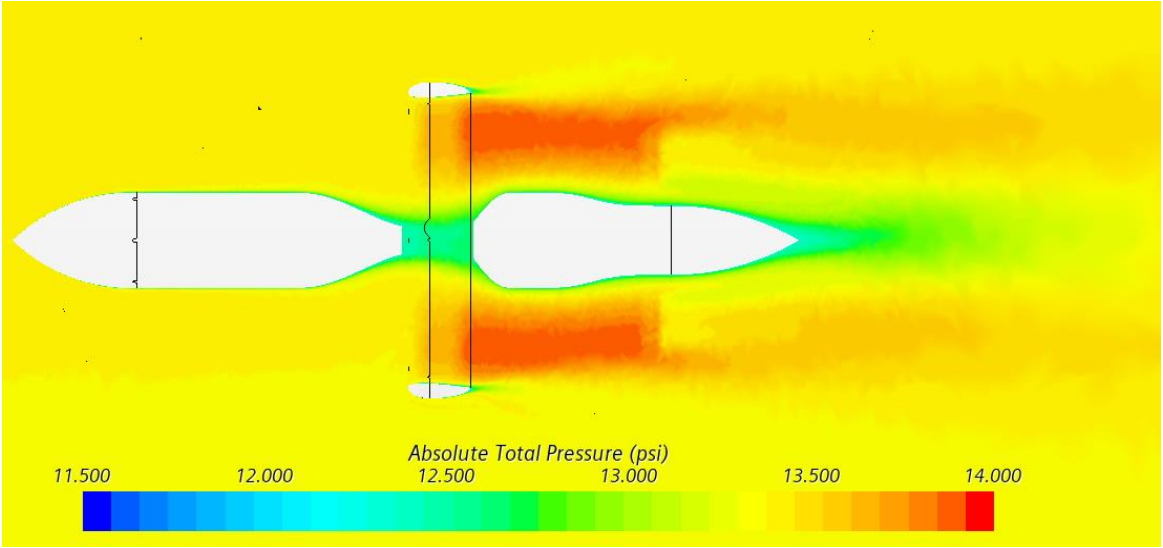

Figure 11.15: Absolute Total Air Pressure

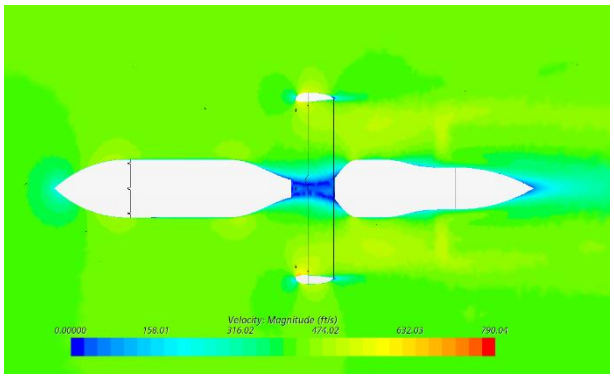

Figure 11.16: Air Velocity Magnitude

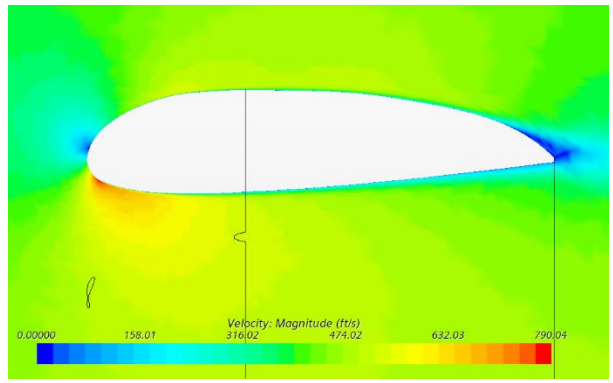

Figure 11.17: Air Velocity at Airfoil

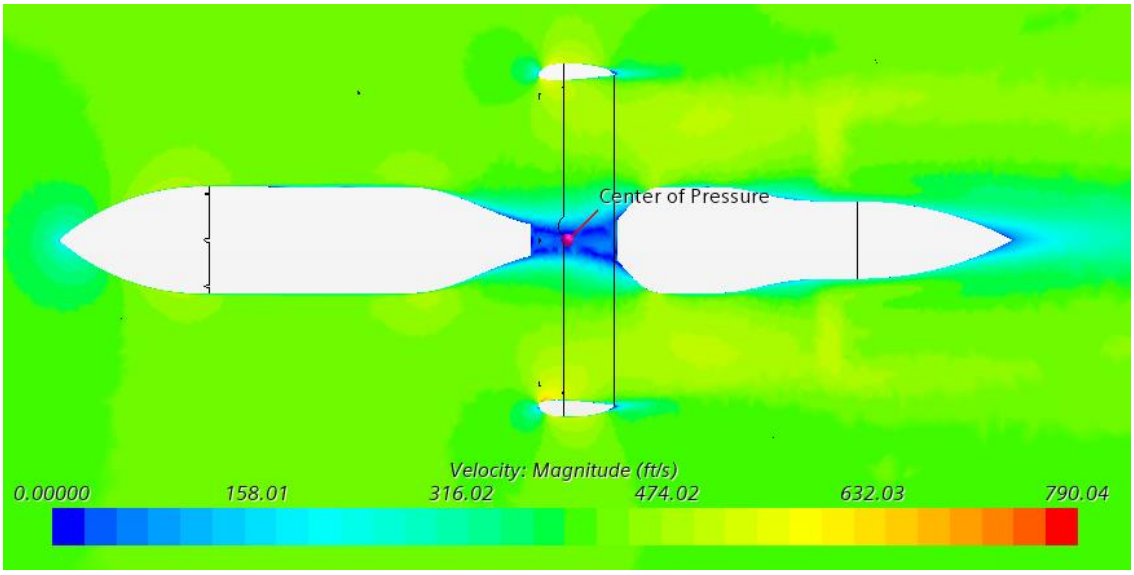

Figure 11.18: Center of Pressure Location

Before this final simulation, a lower fidelity simulation was run which included the NACA inlets on the forward fuselage. This geometry is shown in Figure 11.19. While the numerical results from this preliminary simulation are not trustworthy, they provide a look into how the NACA inlets swirl the flow to maximize mass flow through the inlet, as shown in Figure 11.19 and Figure 11.22. Figure 11.22 describes the velocity vectors at a cross section of the wing.

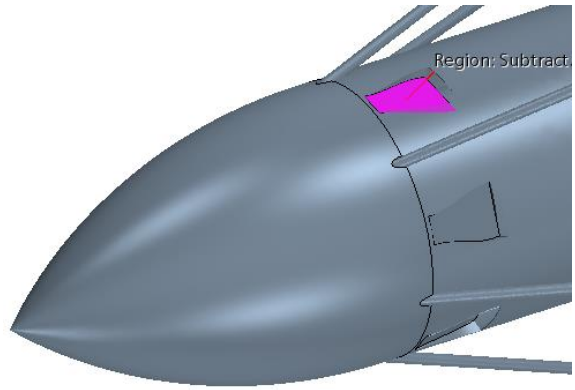

Figure 11.19: NACA Inlet Geometry

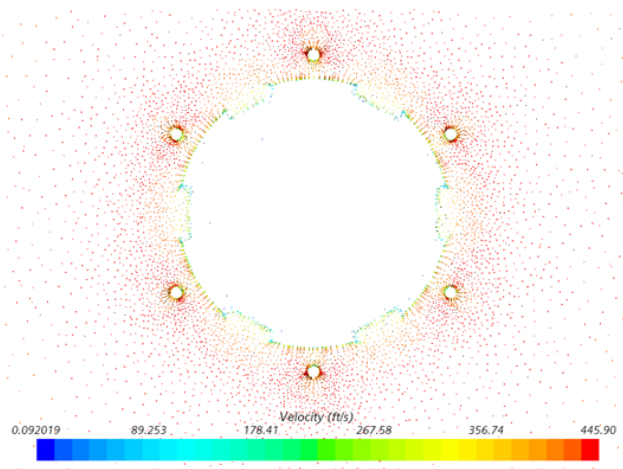

Figure 11.20: Velocity Vectors Around Inlet Fuselage Section

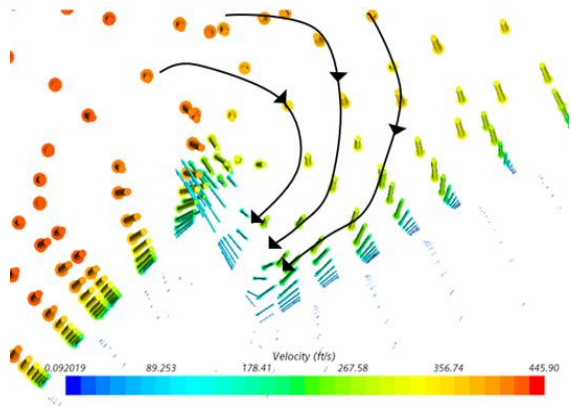

Figure 11.21: Swirl Generated by NACA Inlets

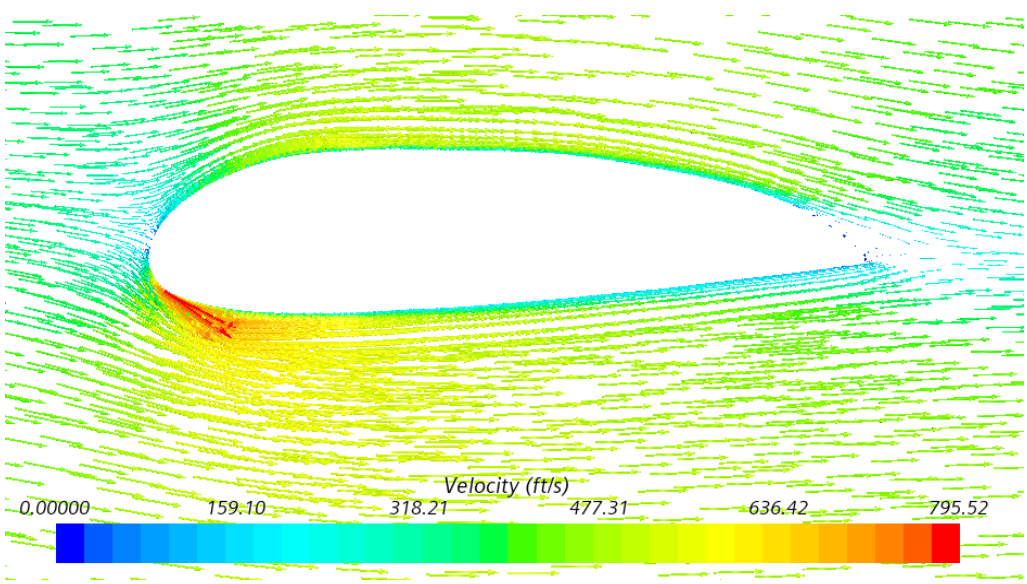

Figure 11.22: Velocity Vectors Around Clark Y Airfoil

12. Antenna Analysis

The RHI*NO utilizes two antenna one with an operating frequency of 5.8 GHz and a second with an operating frequency of 2.4 GHz. In an effort to verify the chosen selection of frequencies the 2.4 GHz antenna was designed, experimentally tested both with a physical model in The University of Kansas anecdotic chamber and a simulation using HFSS, High Frequency Structural Simulator, and the results analyzed.

12.1 Physical Model Creation

To size the antenna Eq. 76 was used. This allowed the known operating frequency of 2.4 GHz to dictate the wavelength. Once the wavelength was determined an approximation for a dipole length of $\frac{\lambda}{2}$ was utilized. This dictated the total length of the dipole to be 12.5 cm. The width of 1.3 cm was arbitrarily chosen as the operational bandwidth was unknown. The port dimensions were 0.5 X 1.3 cm with 4 X 0.25 cm cable connector. A depiction of the created dipole antenna can be observed in Figure 12.1. To utilize the fuselage structure efficiently the antenna was integrated by being wrapped around the inside of the fuselage.

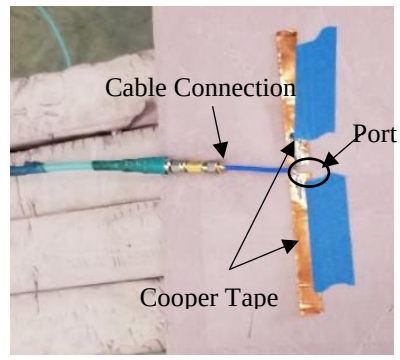

Figure 12.1: Physically Created Dipole For 2.4 GHz Resonance Frequency

$$\lambda = \frac{c}{f} \qquad \text{(Eq. 76)}$$

A simplified mockup design was constructed with a cardboard shipping tube used for the Kevlar fuselage and aluminum foil to represent titanium. The nose cone was not included as it was to have little effect on the antenna. It was also assumed the spinning propellers would create a ground plane which would remove the need to model the

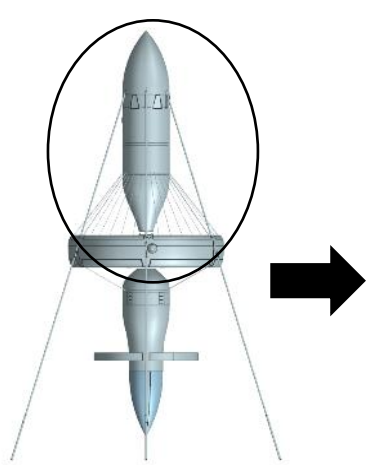

Figure 12.2: RHI*NO Missile

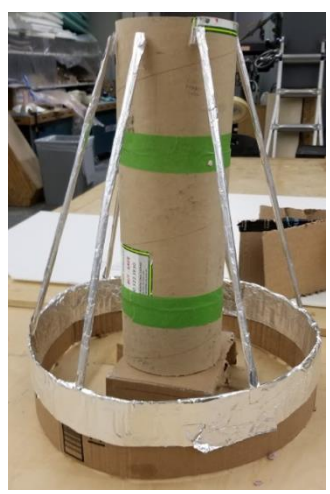

Figure 12.3: Physical Mockup Design

Figure 12.4 AUT Integrated onto Mockup Design

aft section of the design. Figure 12.15 depicts the finished mockup design model. Figure 12.4 depicts the created dipole integrated on the fuselage mockup and placed within the anecdotic chamber.

The electronics housed within the fuselage were tested to observe the electromagnetic interference created. These were modeled with foam wrapped in aluminum foil as shown in Figure 12.5. In addition, tests were conducted to observe the interaction of the motor when it was in the powered off and powered on states, Figure 12.6.

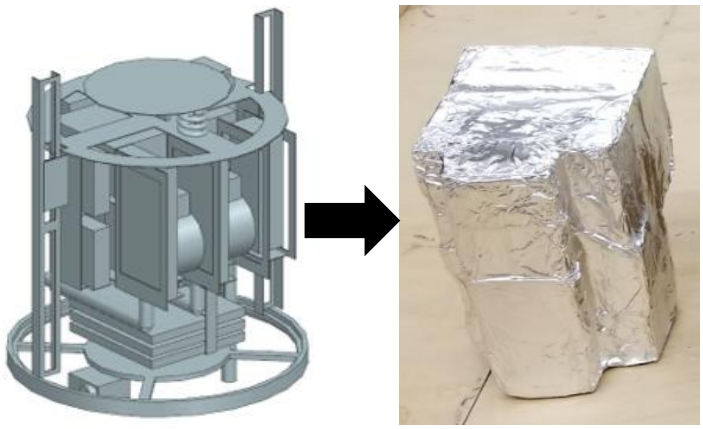

Figure 12.5 :Modeled Sensors and Electronics with Aluminum Wrapped Foam

Figure 12.6: Mounted Turnigy 270KV Motor (Same as Specified for Design)

12.2 Anecdotic Chamber Experimental Set-up

The AUT, antenna under test, was electronically calibrated to remove the inherent noise generated from reflections within the cable, Figure 12.7. While a reference antenna, ETS 3117 Horn antenna, Figure 12.8, was placed on the opposing side of the anecdotic chamber. The sweep frequency was set from 1 GHz to 3 GHz with 801 points to capture the S_{11} results. The plotted S_{11} results of all the trials are shown in Figure 12.9. It is apparent large noise existed in the initial testing of the dipole and thus the bandwidth is not what is expected though the resonating

Figure 12.7: Electronic Calibration

Figure 12.8: ETS 3117 Double Horn Antenna [2]

frequency is shown to be 2.38 GHz. Also, upon observance of the results whether the motor was powered on or powered off had no effect on the inference. A numerical representation of the results can be observed in Table 12.1. Overall, the results yielded once integrated onto the fuselage there was a drop-in resonance frequency and the addition of electronics or the motor did not change this new value. Therefore, to size the antenna properly a smaller than anticipated dipole antenna must be used. To further analyze the design and extract the exact length dimensions a simulation in HFSS, High Frequency Structural Simulator was utilized.

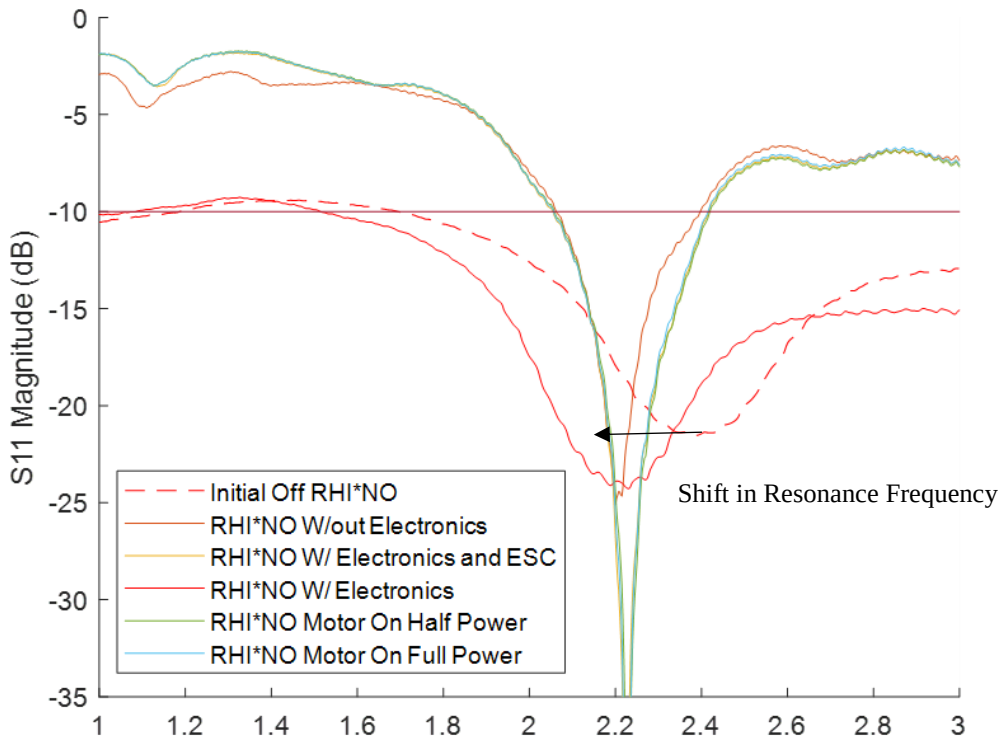

Figure 12.9 S_{11} Comparison of All Tested Conditions

Table 12.1 Resonance Frequency and bandwidth Results for Each Tested Condition

Test	Resonance Frequency (GHz)	Bandwidth (GHz)
Initial	2.38	1.7 – N/A
RHI*NO w/out Electronics	2.2	2.06 – 2.40
RHI*NO with Electronics	2.22	1.5 – N/A
RHI*NO with Electronics and ESC, Motor Off	2.22	2.05 – 2.42
RHI*NO Motor On Half Power	2.22	2.05 – 2.42
RHI*NO Motor On Full Power	2.22	2.04 – 2.41

12.3 HFSS Model

To verify the results obtained in the physical experiment a HFSS simulation was conducted with the same parameters as the physical model. Figure 12.10 displays the created model and the volume of integration. To achieve desirable results a standard practice of $\lambda/4$ of spacing from any edge of the model was employed. PEC, perfect

electric conductor, boundary conditions were applied to the copper arms of the dipole. While a lumped port integration was applied at the location of the port, Figure 12.11. The volume of integration had a radiation boundary applied to ensure the propagation of the waves were kept equal throughout the far-field.

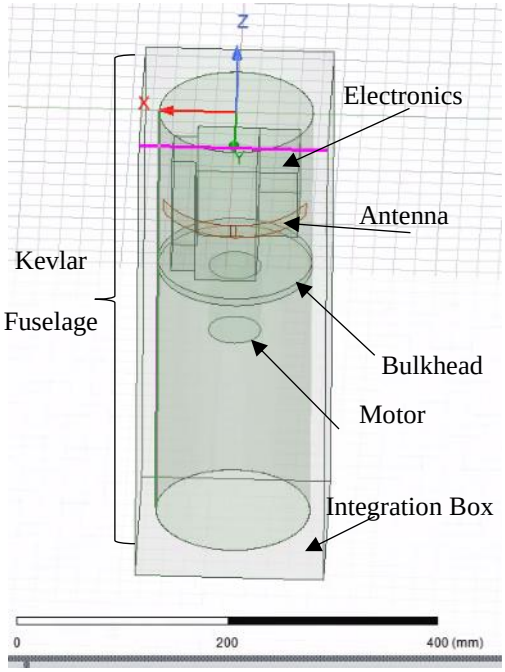

Figure 12.10 RHI*NO Modeled In HFSS

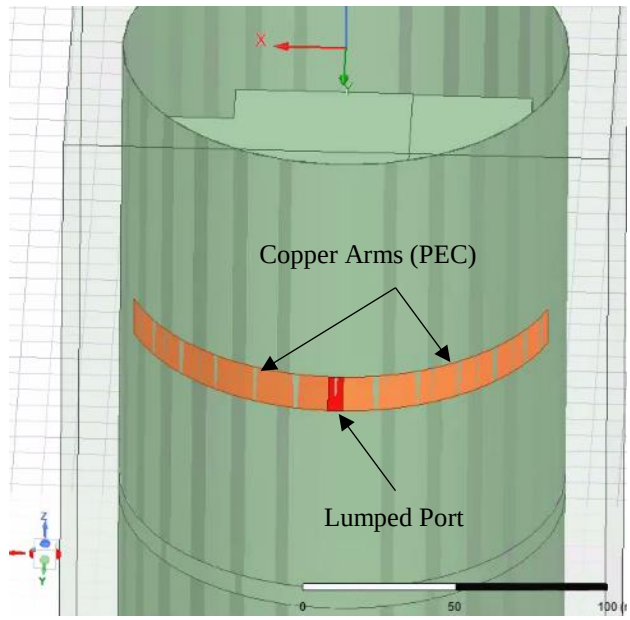

Figure 12.11 Antenna Integrated on Fuselage

The model was analyzed over the frequency range of 1 GHz to 3 GHz at a step size of 0.0025 GHz. This was done for multiple angles which corresponded to the arm lengths of the dipole. As it was found Kevlar and cardboard have different relative permittivity values, 3.6 and 1.8 respectively, a second simulation was created where the Kevlar was changed to cardboard properties. Analysis of the results yielded the Kevlar model and the cardboard model resonated at frequencies close to one another as shown in Figure 12.12 and Figure 12.13 and displayed numerically in Table 12.2. For this reason, the assumption of using cardboard for the physical test was justified. The dipole arm length was determined to be 7.97 cm for a total dipole length of 16.44 cm. This value is close to the results of the physical lab testing verifying the results.

Table 12.2 Resonate Frequencies and bandwidth results for HFSS Models

Angle (deg)	Material	Arm length (cm)	Resonant Frequency (GHz)	Bandwidth (GHz)
65	Kevlar-epoxy	8.35	2.32	2.25 – 2.41
62	Kevlar-epoxy	7.97	2.35	2.3 – 2.43
62	Cardboard	7.97	2.42	2.35 – 2.52

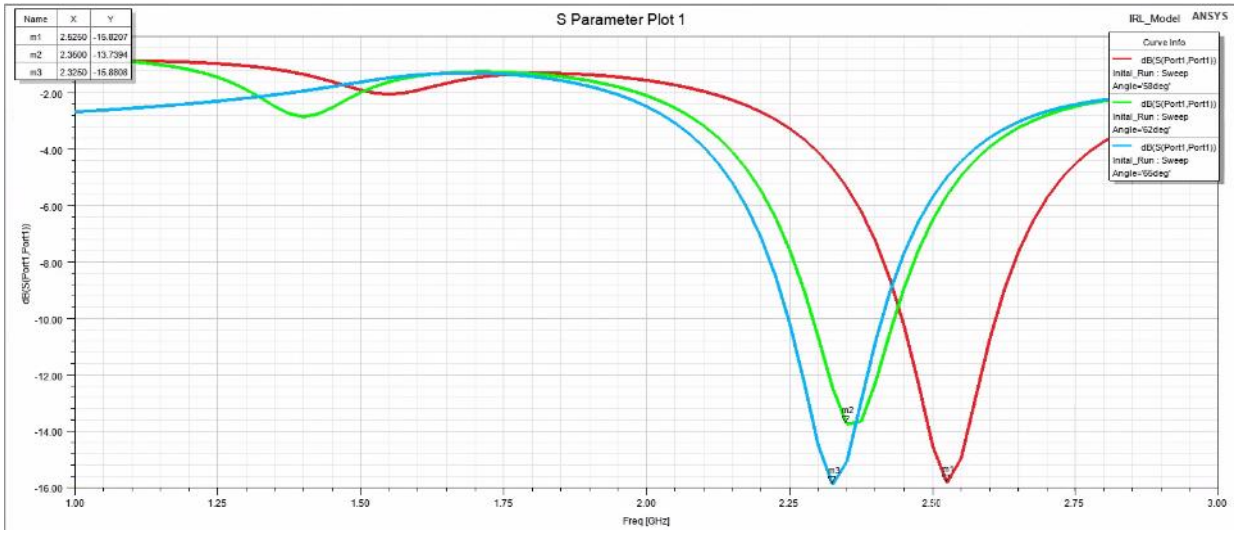

Figure 12.12 Arm Length Effect on Resonance Frequency in HFSS with Kevlar-epoxy Material Selection

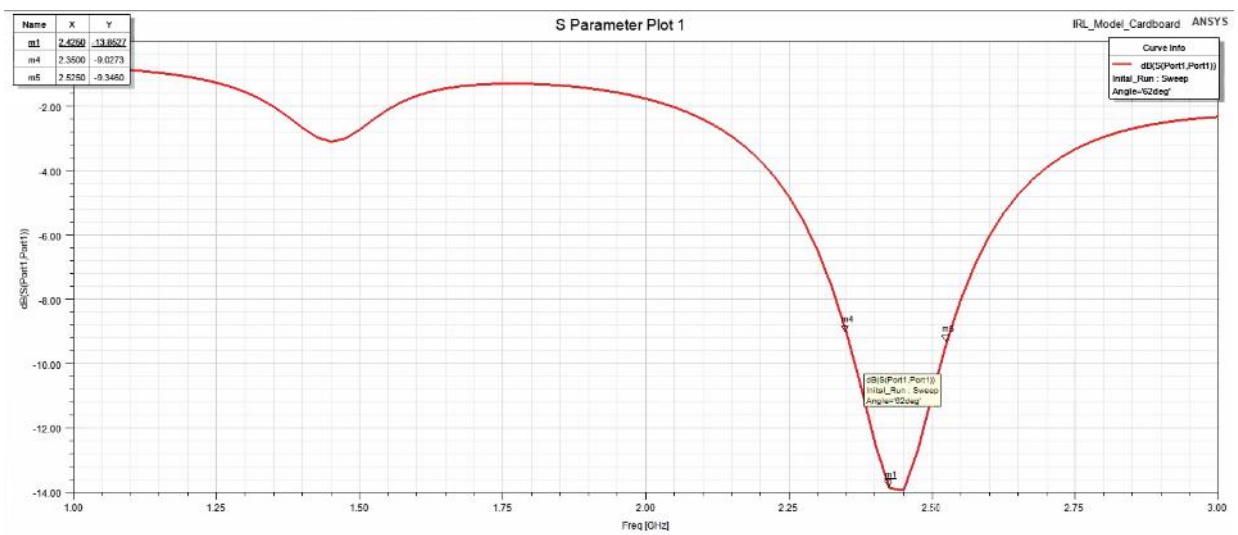

Figure 12.13 S_{11} Plot for Cardboard Material

The radiation pattern of the antenna is displayed in Figure 12.14 and Figure 12.15 while the realized gain which accounts for the efficiency of the materials is displayed in Figure 12.16. Figure 12.17 is provided for reference to the antenna design orientation.

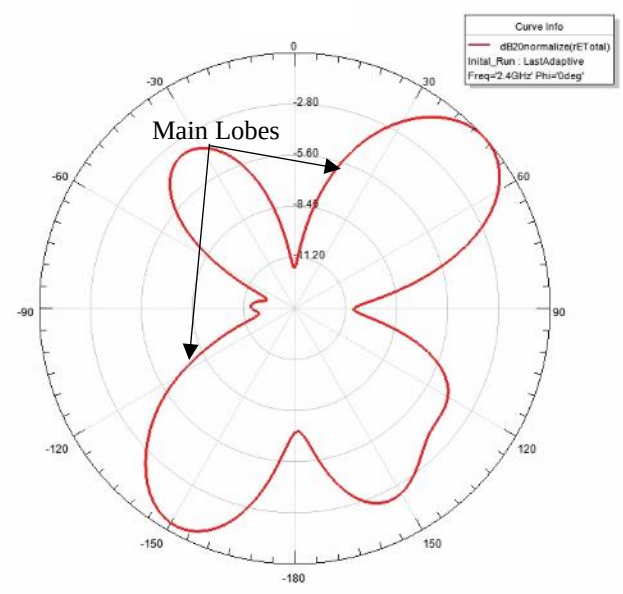

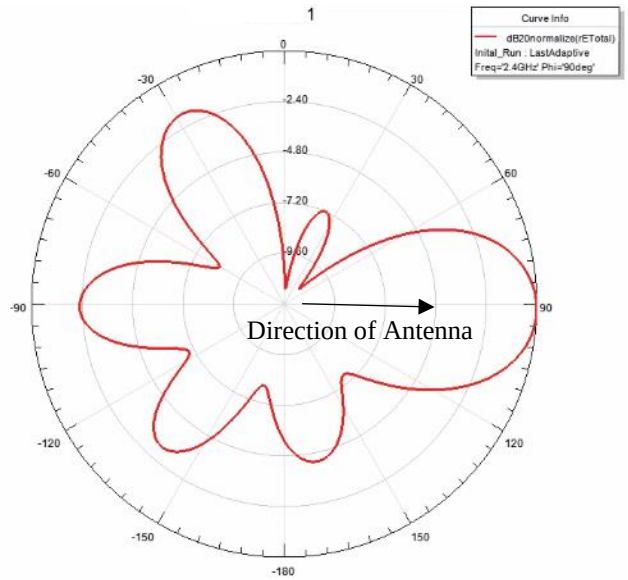

Figure 12.14 Electrical Radiation Plot When $\phi = 0°$ **Figure 12.15 Electrical Radiation Plot When $\phi = 90°$**

A 3D polar plot representation of the electrical radiation field and realized gain radiation field are shown in Figure 12.18 and Figure 12.19 respectively.

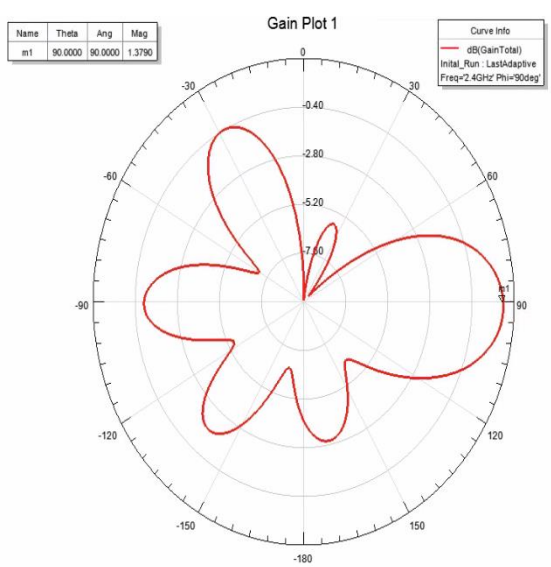

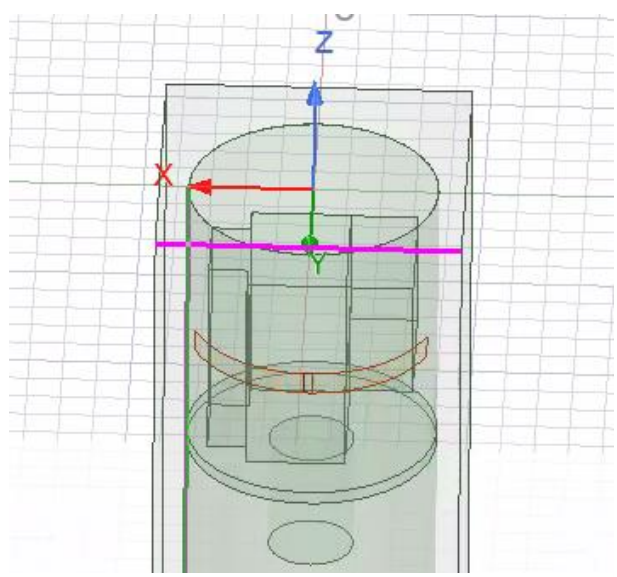

Figure 12.16 Realized Gain Pattern at $\phi = 90°$ **Figure 12.17 Antenna Placement Reference**

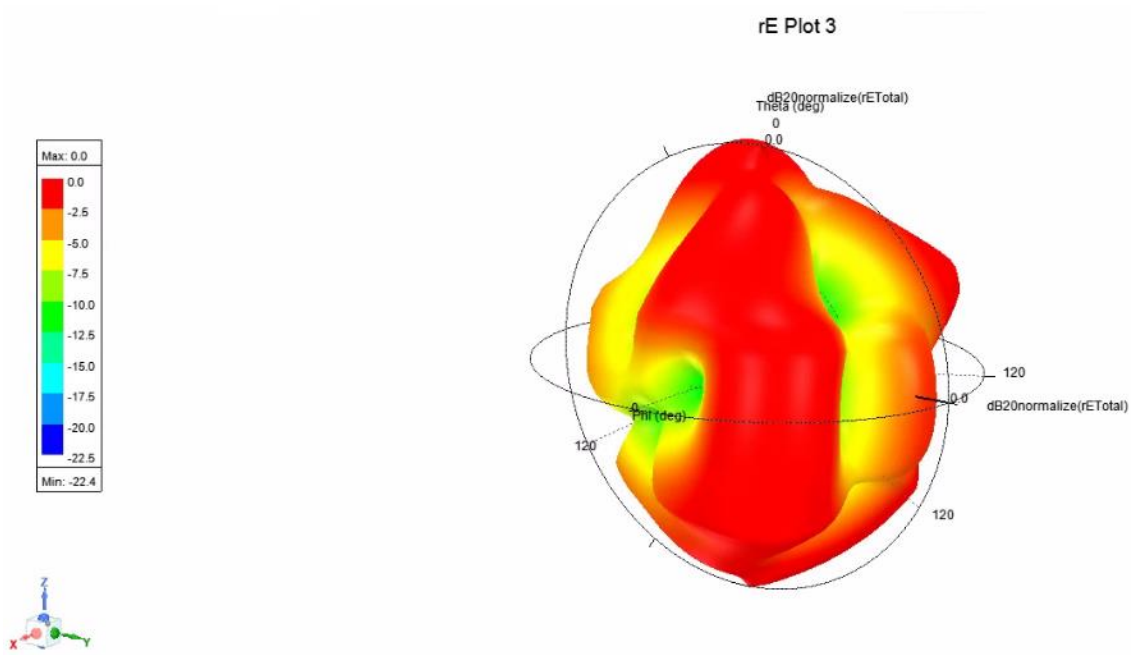

Figure 12.18 Electrical Radiation 3D Polar Plot View 1

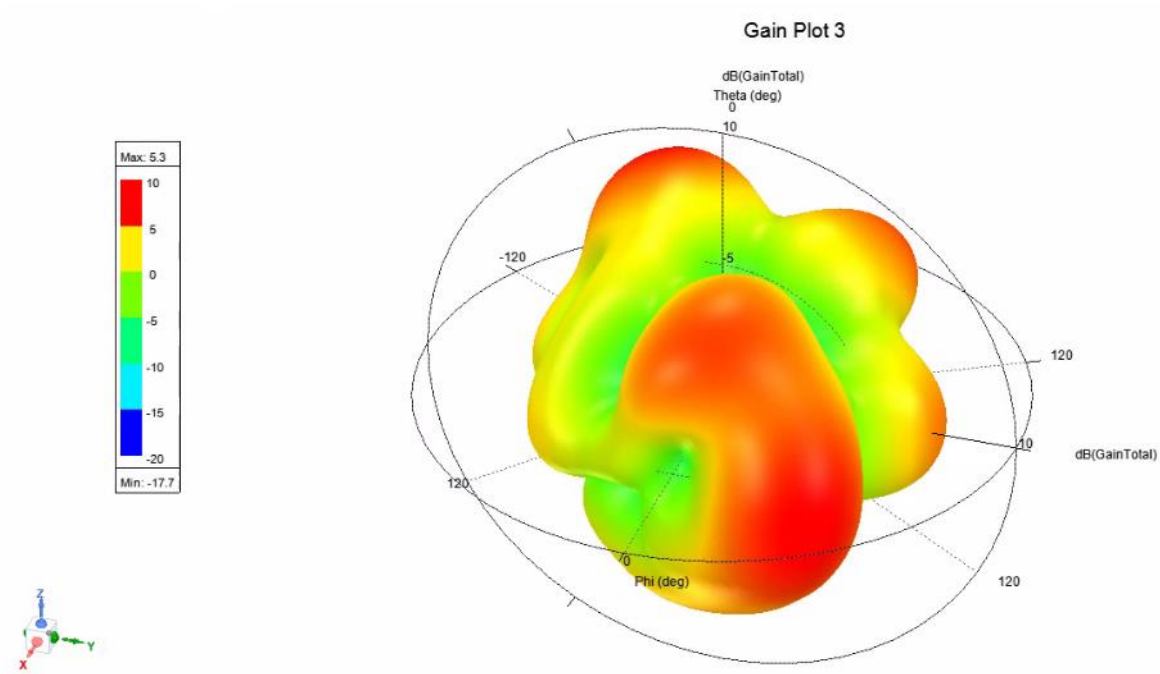

Figure 12.19 Realized Gain Radiation 3D Polar Plot

13. Performance Analysis

The following section covers the performance analysis of the RHI*NO.

13.1 Performance Overmatch Chart

Figure 13.1 illustrates how the flight envelope of the RHI*NO compares to the flight envelopes of potential target drones that the HMS will be sent out to engage. The DJI Phantom and the RQ-11 Raven are both group one drones, the Boeing ScanEagle and the Puma LE are both group two drones, the RQ-7 Shadow is a group three drone, the MQ-1 Predator is a group four drone, and then the MQ-9 Reaper is a group five drone. As mentioned previously, the RFP specifies that each design must be capable of intercepting group two drones, while he interception of group one drones is only an objective. This overmatch chart indicates that the HMS is not only capable of intercepting group one and two drones, but that it can intercept up to and including group five drones. This means that the market for the RHI*NO is far vaster than what was initially planned for; this design brings a reusable, more affordable option to the table which is capable of entirely replacing the current market options for higher drone classes.

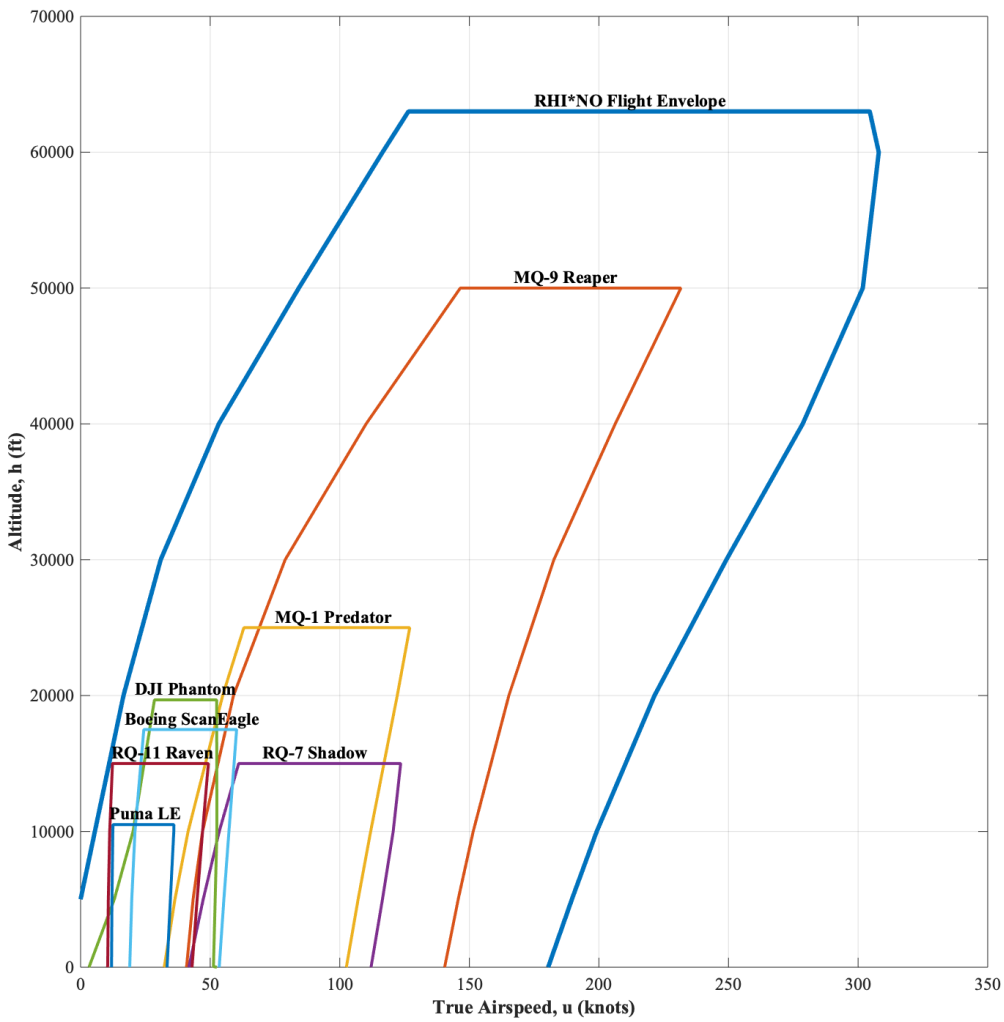

Figure 13.1: RHI*NO Flight Envelope Performance Overmatch Chart

13.2 Engagement Renderings

This section highlights operational scenarios the RHI*NO could expect to operate in. Figure 13.2 displays the ramming scenario of the missile and a DJI phantom drone. The missile would ram into the target and break one of the necessary flight controls, disabling it.

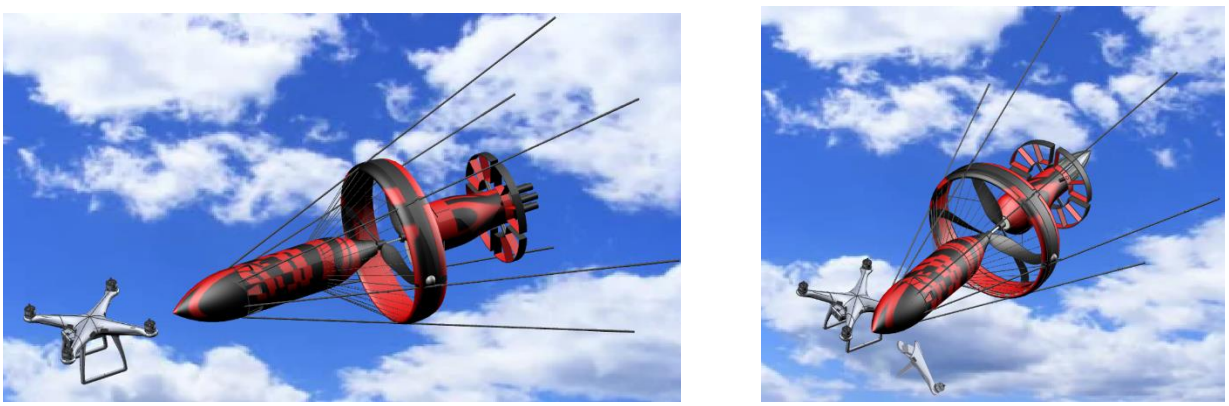

Figure 13.2: RHI*NO Interdiction with DJI Phantom Before (Left) and After Collision (Right) [71]

Another operational scenario the missile may use is the shotgun capabilities. Figure 13.3 depicts the missile overpassing the DJI Phantom and then shooting a standard shotgun shell. The target is neutralized, and pieces are broken off.

Figure 13.3: RHI*NO Interdiction with DJI Phantom Shotgun Engagement [71]

As the RHI*NO is able to reach altitudes of 60,000 ft it is also suspected to be able to combat against Class 4 drones such as the MQ-Predator. The concept involves the missile destroying the radome which houses the sensors with a shotgun blast. This concept is displayed in Figure 13.4. Another concept for intercepting drones of this size involves the RHI*NO diving from above to gain potential energy and ram the target drone's propeller or wing.

Figure 13.4: RHI*NO Interdiction with MQ-Predator Shotgun Engagement [72]

Figure 13.5 and Figure 13.6 present links to videos of the XQ-138 operational flights. These videos illustrate the landing and transition from a vertical takeoff to a dash condition for the HMS design. A typical mission was described in the mission profile presented in Figure 1.1. Based on the energy demands of the system the total flight time required for a complete mission is 4.2 minutes which encompasses a second engagement. With the current amount of 84 batteries the 12 lb. RHI*NO is able to operate for approximately 20 minutes. This would allow for multiple engagements over a period of 15 minutes with extra flight time available to ensure a safe return to base flight leg. To intercept 10 drones over the course of 60 minutes a minimum of 2 RHI*NO's would be fielded. The first would be launched to deal with the current threats for 15 minutes in which the second RHI*NO is deployed and the first has its batteries and shotgun shells replaced. This process would continue for the duration of the raid. For complete safety a third RHI*NO is recommended as it would allow for the unfortunate circumstance where one of the RHI*NO's sustained too much damage.

Figure 13.5: XQ-138 Landing [73]

Figure 13.6: XQ-138 Flight Video [74]

14. Economics Model

Minimizing the upfront cost of the counter UAV system is of large importance for HFB-WEB. Cost minimization methods include increasing the production rate and offering an entire family of counter-UAV systems that vary in size, application, and target range. All these ideas will help reduce the price by spreading the initial research cost across multiple models. Figure 14.1 illustrates this trend.

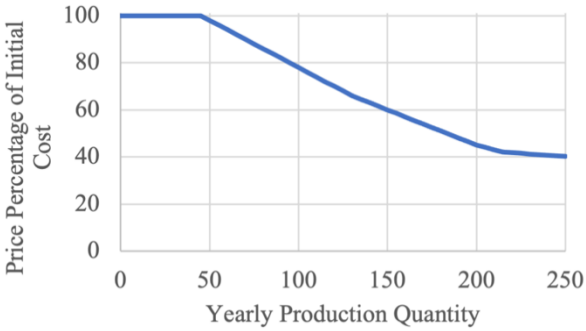

Figure 14.1 Production Cost Projections

Lifecycle costs should be considered as well. When in the market for a counter drone system, buyers should be aware that lifetime costs of multi-use systems are far lower than those of single-use systems. Therefore, a larger initial investment prevents the purchase of troublesome systems that can fail to perform as anticipated and use more time and resources than originally accounted for. Lifecycle costs include initial capital and a multiyear operating cost [75]. This system has a projected 10 UAV interception lifespan, with system maintenance being performed periodically to ensure optimal performance throughout the system's lifespan. Maintenance to the HMS includes patching damaged Kevlar sections of the body and assessing the airworthiness or electronic and control systems as well as batteries. This additional maintenance cost will be accounted for by adding an additional $965 to each

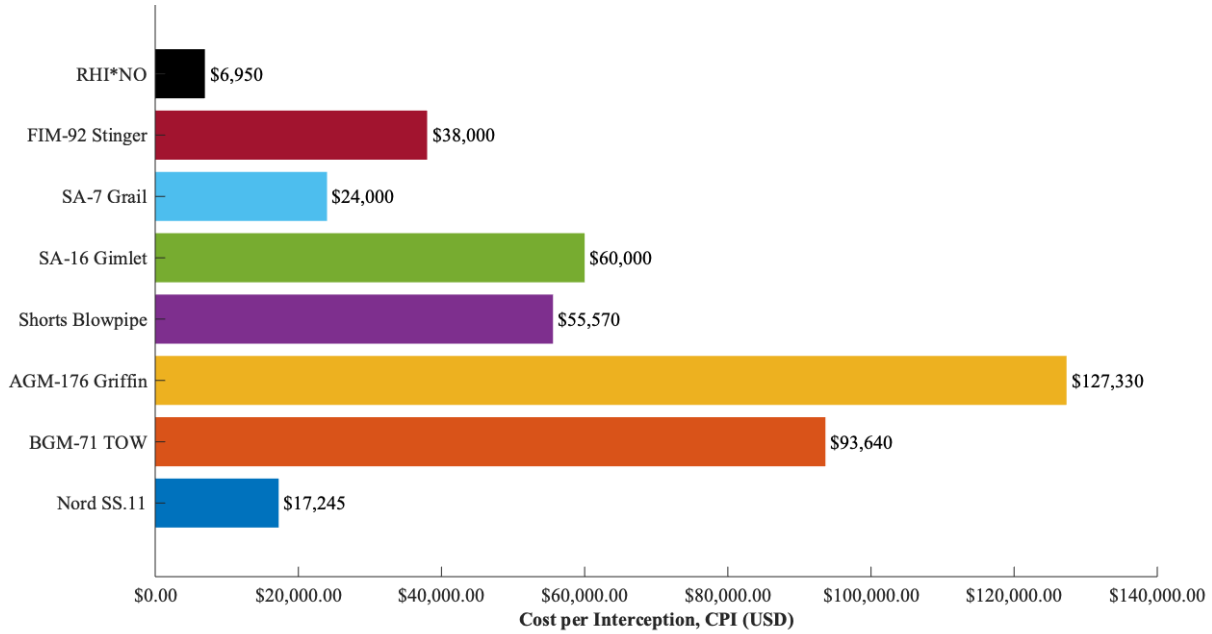

Figure 14.2 Cost Per Interception of Various Missile Systems

interception, bringing the total cost per interception (CPI) to $6,950. This is a very reasonable price compared to what is commonly used on the market today; the FIM-92 Stinger has a CPI of $38,000, BGM-71TOW has a CPI of $93,640, NORD SS.11 has a CPI of $17,245, AGM-176 Griffin has a CPI of $127,333, Blowpipe MANPAD Missile has a CPI of $55,570, SA-7 Grail has a CPI of $24,000, and SA-16 Grail has a CPI of $60,000 [9]. Therefore, 100 interceptions by the FIM-92 will cost $3,800,000, whereas the HMS will only cost $90,000 for the same number of interceptions. These can be seen in the following figure to visually represent the market for counter drone systems cost per interception.

The preliminary pricing of the RHI*NO research and development (R&D) is based off of the processes documented in Roskam's book 8 [74]. Using this method, the total cost for the research and development comes

out to $2,430,000. This includes airframe engineering and design costs, development support and design costs, flight test operations costs, test and simulation facilities costs, as well as financing the project. The values for all of these listed factors were calculated using equations 3.1 – 3.19 of Reference 74. With these equations, the actual cost for the cost per interception can be found based on different production rates to help cover R&D costs. The range of 50, 100, 150, and 200 models were looked at; at 50 produced, the cost per interception is $9,360; at 100 produced, cost per interception is $6,950; at 150 produced, cost per interception is $6,120; and lastly at 200 produced, cost per interception is $5,720. These numbers are based off a 10-interception lifetime of the RHI*NO. The following table includes the equations used and what variables were are solved for.

Table 14.1: RHI*NO Research and Development Costs

Abbreviation	What it stands for	Value	Equation
C_{aed_r}	Airframe Engineering and Design Costs	$4,487	Caedr=(Mhraedr)(Rer)
C_{dst_r}	Development Support and Design Costs	$217	Cdstr=0.008325(Wampr)*0.873(Vmax)*1.890(Nrdte)*0.346(CEF)*Fdiff
C_{fta_r}	Flight Test Aircraft Costs	$2,309,504	Cftar= C(e+a)r + Cmanr+ Cmatr + Ctoolr + Cqcr
C_{fto_r}	Flight Test Operations Cost	$380	ftor= 0.001244(Wampr^1.160)*(Vmax^1.371)*((Nrdte-Nst)^1.281)*CEF*Fdiff*Fob
C_{tsf_r}	Test and Simulation Facilities Cost	$115,729	Ctsft = Ftsf*Crdte
C_{pro_r}	RDT&E Profit	$231,459	Cpror = Fpror * Crdte
C_{fin_r}	Cost to Finance	$231,459	Cfinr = Finr*Crdte
MHR_{aed_r}	Work Hours for Airframe engineering and design	59	Mhrader= 0.0396*(Wampr)*0.791(Vmax)*1.526(Nrdte)*0.183(Fdiff)*(Fcad)
W_{ampr}	AMPR Weight	1.8	Wampr= We - Wi
V_{max}	Max Velocity	250	~~
N_{rdte}	Number of Test Products	10	~~
F_{diff}	Judgment Factor	1.5	~~
F_{cad}	Cumputer aided design modifier	1	~~
R_{e_r}	Dollar Engineering cost per hr	$76	~~
CEF	Cost Escalation Factor	7	~~
$C_{(e+a)_r}$	Cost of engine and avionics	$131,149	C(e+a)r= (Cer*Ne+Cpr*Np +Cavionicsr)(Nrdte-Nst)
C_{e_r}	Cost Per Engine	$54	~~
N_e	Number of Engines	2	~~
C_{p_r}	Cost Per Propeller	$79	~~
N_p	Number of Propellers	2	~~
$C_{avionics_r}$	Cost of Avionics	$25,964	~~
N_{st}	Number of Static Aircraft	5	~~
C_{man_r}	Manufacturing Price of FT Airplanes	$1,647,726	Cmanr = (MHRmanR)(Rmr)
MHR_{man_r}	number of manufacturing manhours	$41,193	MHRmanR = 28.984(WampR)*0.740*(Vmax)*0.543(Nrdte)*0.524(Fdiff)
R_{m_r}	Manufacturing Labor Rate	$40	~~
C_{mat_r}	Cost of Materials	$221,911	Cmatr=37.632(Fmat)((Wampr)^(0.689))*(Vmax)^(0.624)*(Nrdte)^(0.792)*CEF
F_{mat}	Cost Factor	$3	~~
C_{tool_r}	Tooling Costs	$94,514	Ctoolr=MHRtoolr*Rtr
MHR_{tool_r}	Tooling Mnhours	1890	Mhrtoolr=4.0127(Wampr)^0.764*Vmax^0.899*Nrdte^0.178*Nrr^.066*Fdiff
R_{t_r}	Toolong Labor Rate	$50	~~
N_{r_r}	Production rate	0.33	~~
C_{qc_r}	Quality Control Cost	$214,204	Cqcr = 0.13*Cmanr
F_{obs}	Observable	1	~~
F_{tsf}	Adjustment factor	0.05	~~
F_{pro_r}	Suggested 10% profit	0.1	~~
F_{fin_r}	Interet Rate	0.1	~~
Total Cost	Total Summative cost to do RND&T	$2,430,317	~~

15. Compliance Matrix

The following table provides the location in the report that each of the requirements laid out in the RFP [1] were either met or addressed.

RFP Requirement [1]	Demonstrated	Page No.
The system shall be capable of achieving a threshold range (parallel to ground) of 3.0 nautical miles and an objective range of 3.5 nmi.	35 nmi range	46
It shall be capable of achieving a threshold service ceiling of 3,000 ft above ground level (AGL) and an objective ceiling of 5,000 ft AGL.	Performance Ceiling of 63,000 ft	23
The entire launch system (launcher + one missile) when fired shall weigh less than 40 pounds. A single launcher and 10 missiles must weigh no more than 125 pounds	14.7 lb per HMS & 15 lb for RF sensor; Only 3 Systems Required per Mission	45
The system must be capable operating in a raid scenario. This requires the system to detect, acquire, target, and engage up to 10 UAVs in an hour.	2 RHI*NO's needed	69
The target system, including fuel and/or propellants, shall be compatible with safe storage, transportation, and handling requirements for at least 10 years without maintenance	Usage of Electric System Eliminates Safe Storage Concerns	6
A warhead (if used) shall not be armed within 200 ft of the launch location.	Not Used	9
The decibel noise level shall not exceed 120dBA within 100ft of the launch location.	Less than 70 dB within 100 ft	24
The missile shall not accelerate more than 2g's at launch to reduce personnel injury.	Vertical Takeoff in Hover Mode; Programmable 2g Launch Acceleration	30
If desired, a modular system may be designed with a common propulsion system and different types of anti-UAV payloads. Payloads shall be capable of being changed within 5 minutes.	Modular System; Shotgun Reloading in Under 5 minutes; Battery Changeout in Under 5 minutes	11, 31
Assume a production run of 200 missiles and 20 launchers a year for 10 years plus 15 missiles for developmental testing.	Minimum Production Run of 200 Systems per Year	69 - 70

16. HFB-WEB Group Member Contact Information

Jack Barkei: jackbar2299@gmail.com

Robert Bowes: bbowes41@gmail.com

Christopher Eavenson: eavensch@gmail.com

Samantha Friess: sfriess28@gmail.com

Alex Welicky: alexwelicky@hotmail.com

Brian Von Holtz: brianvonholtz.17@gmail.com

17. References

1. "2020-2021 Graduate Team Missile Design Competition – Shoulder-Launched Anti-UAV Missile System," *AIAA*, Oct. 2020, [https://www.aiaa.org/docs/default-source/uploadedfiles/membership-and-communities/university-students/design-competitions/aiaa-2021-graduate-team-missile-design_competition-rfp.pdf?sfvrsn=c6c3ad23_0]
2. Kemp, J., "Humvee (Operation Black Mesa)," *artstation.com*, [https://www.artstation.com/artwork/4rkAn], 22 March 2021.
3. Perlman, A., "DJI Firmware Update Automatically Disables Flights in D.C. and Across International Borders," *UAV Coach*, [https://uavcoach.com/dji-firmware-update/], 29 Jan. 2015.
4. Drone Defence, "What is the Paladyne E1000MP?," *dronedefence.co.uk*, [https://www.dronedefence.co.uk/paladyne-e1000mp/], 4 February 2021, 9:30 pm.
5. DroneShield, "DroneGun Tactical," *droneshield.com*, [https://www.droneshield.com/dronegun-tactical], 4 February 2021, 9:30 pm.
6. Drone Defence, "What is the Paladyne E1000MP?," *dronedefence.co.uk*, [https://www.dronedefence.co.uk/paladyne-e1000mp/], 4 February 2021, 9:30 pm.
7. Drone Defence, "What is SkyFence?," *dronedefence.co.uk*, [https://www.dronedefence.co.uk/skyfence/], 4 February 2021, 9:35 pm.
8. IXI Electronic Warfare, "Disable Drones in Seconds with Powerful, Hand-Held Software Defined Radio Technology," *ixiew.com*, [https://www.ixiew.com/products/dronekiller/], 4 February 2021, 9:40 pm.
9. Raytheon Missiles & Defense, "Stinger Missile," *raythonmissilesanddefense.com*, [https://www.raytheonmissilesanddefense.com/capabilities/products/stinger-missile], 4 February 2021, 10:00 pm.
10. Openworks, "SkyWall Patrol," *openworksengineering.com*, [https://openworksengineering.com/skywall-patrol/], 4 February 2021, 10:25 pm.
11. Savage Corp., "Counter-UAS Kinetic Weapon System," *savae-corp.com*, [http://savage-corp.com/index.html], 5 February 2021, 11:20 am.
12. New Atlas, "US Army Tests Drone-Killing 50 mm Cannon," *newatlas.com*, [https://newatlas.com/us-army-eads-anti-drone-system/39781/], 5 February 2021, 1:10 pm.

13. Lockheed Martin, "ATHENA Laser Weapon System Prototype," *Lockheed Martin Corporation*, [https://www.lockheedmartin.com/en-us/products/athena.html], 5 February 2021, 1:30 pm.
14. BBC News, "Drone Squad to be Launched by Tokyo Police," *bbc.com*, [https://www.bbc.com/news/technology-35070818], 12 February 2021, 3:00 pm.
15. Delft Dynamics, "DroneCatcher," *Delft Dynamics B.V.*, [https://dronecatcher.nl/#], 5 February 2021, 1:45 pm.
16. Barrett, R. M., "Hovering Missiles: New Tools for Target ID, Interior Precision Strike, Friendly Fire Mitigation and Persistent Suppression," *The University of Kansas Department of Aerospace Engineering*, [https://ndiastorage.blob.core.usgovcloudapi.net/ndia/2009/gunmissile/7948.pdf], 11 February 2009.
17. Humphries, M. (2017, March 14). US Air Force Orders Anti-Drone Net-Filled shotgun shells. Retrieved February 21, 2021, [https://www.pcmag.com/news/us-air-force-orders-anti-drone-net-filled-shotgun-shells].
18. Skynet Drone Defense. (n.d.). Retrieved February 21, 2021, [https://www.maverickdrone.com/products/skynet-drone-defense-3-pack?variant=32000607748142].
19. Kandaswamy, G., "Drone Based Sensor Platforms," *TATA Consultancy Services*, [https://www.itu.int/en/ITU-D/Regional]
20. "3DM-CX5-10 IMU," *Parker Lord*, [https://www.microstrain.com/inertial-sensors/3dm-cx5-10], 26 February 2021.
21. de Bree, H.E., "The Acoustic Vector Sensor, a Versatile Battlefield Acoustics Sensor," *The International Society for Optical Engineering*, 2011. 25 February 2021, 11:00 am.
22. Washington University in St. Louis: "Acoustic Vector Sensor Array Processing: Overview," [https://www.ese.wustl.edu/~nehorai/research/avs/avssensor.htm], 25 February 2021, 1:30 pm.
23. Bernardini, A., Bordoni, U., Capodiferro, L., Mangiatordi, F., Pallotti, E., "Drone Detection by Acoustic Signature Identification," *Society for Imaging Science and Technology*, 2017. 25 February 2021, 3:00 pm.
24. de Bree, H.E., "Acoustic Vector Sensors Increasing UAVs Situational Awareness," *Microflown Technologies*, 2009. 25 February 2021, 4:30 pm.
25. Nash, J., "Sensors Pinpoint Gunfire by Measuring Air Movement," *Scientific American*, 2013. [https://www.scientificamerican.com/article/acoustic-sensor-drone-surveillance-war/], 25 February 2021, 5:30 pm.

26. Roskam, J., "Airplane Design Part IV: Calculation of Aerodynamic, Thrust, and Power Characteristics," DARCorporation, KS, 2018, pp. 272,325-326
27. Dedrone, "RF-360," *dedrone.com*, [https://www.dedrone.com/products/hardware/rf-sensors/rf-360], 26 February 2021, 2:00 pm.
28. Dedrone, "RF-360," *dedrone.com*, [https://www.dedrone.com/products/hardware/rf-sensors/rf-360], 26 February 2021, 2:00 pm.
29. Orqa, "Orqa FPV.One," *orqafpv.com*, [https://orqafpv.com/fpvdetails/Z2lkOi8vc2hvcGlmeS9Qcm9kdWN0LzIxNjQwMDU0MDQ3NDU=], 14 March 2021, 5:30 pm.
30. Clark YM-18 Airfoil from UIUC Airfoil Coordinates Database. (n.d.). Retrieved March 13, 2021, from [http://airfoiltools.com/airfoil/details?airfoil=clarym18-il].
31. Barrett, Ronald., "AE522 Outline and Requirements," University of Kansas, 2021.
32. Barrett, R M., et al. "Acoustic Noise Suppressing Ducted Fan Propulsor Mounting Arrangement and Treatments," U.S. Patent Application No. 14/047,779, October 15, 2020.
33. Crispin, Michala., "AE 721 HW3," The University of Kansas, 2021.
34. Hobby King, "Turnigy SK8 6374-192KV Sensored Brushless Motor (14P)", *HobbyKing.com*, [https://hobbyking.com/en_us/turnigy-sk8-6374-192kv-sensored-brushless-motor-14p.html?queryID=75f18963106293166f401dcab3faadf7&objectID=74475], 8 March 2021.
35. Hobby King, "PROPDRIVE v2 5060 270KV Brushless Outrunner Motor", *HobbyKing.com*, [https://hobbyking.com/en_us/propdrive-v2-5060-270kv-brushless-outrunner-motor.html?queryID=9243e56cd3fb9b937dfc22dd527ecfd5&objectID=59214&indexName=hbk_live_magento_en_us_products], 8 March 2021.
36. Hobby King, "Turnigy RotoMax 50cc Size Brushless Outrunner Motor", *HobbyKing.com*, [https://hobbyking.com/en_us/turnigy-rotomax-50cc-size-brushless-outrunner-motor.html?queryID=9ed563e162bd5340a0ff8aacb1e31a6e&objectID=30335&indexName=hbk_live_magento_en_us_products], 8 March 2021.
37. Hobby King, "Turnigy SK8 6354-260KV Sensored Brushless Motor (14P)", *HobbyKing.com*, [https://hobbyking.com/en_us/turnigy-sk8-6354-260kv-sensored-brushless-motor-

14p.html?queryID=b8c8282f80f40a3124ec6c0544295d5a&objectID=74454&indexName=hbk_live_magento_en_us_products], 8 March 2021.

38. Hobby King, "Turnigy SK3 90mm (6S-8S 3000w) Fandrive Brushless EDF Motor - 3968-1500 KV", *HobbyKing.com*, [https://hobbyking.com/en_us/turnigy-sk3-90mm-8s-3000w-fandrive-brushless-edf-motor-3968-1500kv.html?queryID=b439df850d3ae2dcc2b5a44abeaba386&objectID=47159&indexName=hbk_live_magento_en_us_products], 8 March 2021.
39. Hobby King, "Turnigy XK-4074 2000KV Brushless Inrunner", *HobbyKing.com*, [https://hobbyking.com/en_us/turnigy-xk-4074-2000kv-brushless-inrunner.html?queryID=3fab8584387651ea19fd376d93e4f7bc&objectID=40529&indexName=hbk_live_magento_en_us_products], 8 March 2021.
40. Barrett, R. M., "AE522_HFB_Web_3_1_21," The University of Kansas Aerospace Engineering Department, 9:00 am – 10:30 am, 1 March 2021.
41. Kemp, J., "Humvee (Operation Black Mesa)," *artstation.com*, [https://www.artstation.com/artwork/4rkAn], 22 March 2021.
42. Barrett, R. M., "AE522_HFB_Web_4_28_21," The University of Kansas Aerospace Engineering Department, 9:00 am – 10:30 am, 28 April 2021.
43. Barrett, R. M., "University of Kansas MicroStator Ducted Fan Noise Comparison," The University of Kansas Aerospace Engineering, 28 April 2021.
44. In3DSpace. (n.d.). SpaceX Falcon 9 Grid Fin Model. Retrieved March 14, 2021, [https://www.etsy.com/listing/692343619/spacex-falcon-9-grid-fin-please-read].
45. Huang, C., Liu, Wen, and Yang, G., "Numerical Studies of aeroelastic effects on grid fin aerodynamic performances," Chinese Journal of Aeronautics, Aug. 2017, Vol. 30, Issue 4, p. 1300.
46. Roskam, J., "Airplane Design Part II: Preliminary Configuration Design and Integration of the Propulsion System," DARCorporation, KS, 2018, pp. 259-265
47. Apogee Rockets, "Highly Visible Apogee Nylon Parachute," *Apogee Components*, [https://www.apogeerockets.com/Building-Supplies/Parachutes/Larger-than-24in/48in-Printed-Nylon-Parachute], 2019.

48. Arnold, Emily, "Motor and Sensor Interference Technical Conference," The University of Kansas Aerospace Engineering Department, 2:15 pm – 3:10 pm, 17 March 2021.

49. Liang, Oscar., "The Different Frequencies For FPV," [https://oscarliang.com/fpv-frequency/], 21 March 2021.

50. Arnold, Emily, "Wire Insulation Technical Conference," The University of Kansas Aerospace Engineering Department, 2:15 pm – 2:20 pm, 17 March 2021.

51. Hobby Partz, "Solar Servo D220 0.11 @ 4.8v Digital 9 g Micro Servo," *HobbyPartz.com*, [Solar Servo D220 0.11@4.8v Digital 9g Micro Servo (hobbypartz.com)], 15 March 2021.

52. Hobby King, "YEP 100A (2~6S) SBEC Brushless Speed Controller", *HobbyKing.com*, [Hobbyking YEP 100A (2~6S) SBEC Brushless Speed Controller], 15 March 2021.

53. Amazon, "Adafruit 4480 LSM6DS33 6-DoF Accel + Gyro IMU- Stemma QT/Qwiic," *Amazon.com*, [Amazon.com: Adafruit 4480 LSM6DS33 6-DoF Accel + Gyro IMU - Stemma QT/Qwiic: Electronics], 15 March 2021.

54. Amazon, "GPS Module GPS NEO-6M(Ar duino GPS, Drone Microcontroller GPS Receiver) Compatible with 51 Microcontroller STM32 Ar duino UNO R3 with IPEX Antenna High Sensitivity for Navigation Satellite Positioning," *Amazon.com*, [Amazon.com: GPS Module GPS NEO-6M(Ar duino GPS, Drone Microcontroller GPS Receiver) Compatible with 51 Microcontroller STM32 Ar duino UNO R3 with IPEX Antenna High Sensitivity for Navigation Satellite Positioning: Electronics], 15 March 2021.

55. MicroFlown Technologies, "Small Yet Powerful, The PU MATCH Sound Intenisty Probe," *Mircoflown Techmologies*, [PU match | Miniaturized 1D Sound Intensity Probe - Microflown], 15 March 2021.

56. Run Cam, "RunCam Nano HD," *RunCam.com*, [RunCam Nano HD - RunCam FPV Store], 15 March 2021.

57. Amazon, "Flysight TX5812-SMA 1200mW Transmitter 5.8Ghz 32CH FPV Long Range Video Transmitter 6-16V Power Output FPV Transmitter 5.8 Litter Brother of Flysight Black Mamba 5.8Ghz 2W," *Amazon.com*, [https://www.amazon.com/Flysight-TX5812-SMA-1200mW-Transmitter-Brother/dp/B01GFPCSTY/ref=asc_df_B01GFPCSTY/?tag=bingshoppinga-20&linkCode=df0&hvadid=&hvpos=&hvnetw=o&hvrand=&hvpone=&hvptwo=&hvqmt=e&hvdev=c&hvdvcmdl=&hvlocint=&hvlocphy=&hvtargid=pla-4584001418822391&psc=1], 15 March 2021.

58. Amazon, "2PCS 7.4V 2700mAh 10C Drone LiPo Battery for X4 H501S H501C H501A H501M H501SW H501S pro Brushless Quadcopter Spare Parts(H501S-14) with 2in1 Charger," *Amazon.com*,

[https://www.amazon.com/2700mAh-Battery-Brushless-Quadcopter-H501S-14/dp/B08NFP212J/ref=sr_1_1_sspa?dchild=1&hvadid=78408986171398&hvbmt=be&hvdev=c&hvqmt=e&keywords=drone+battery+lipo&qid=1615833134&sr=8-1-spons&psc=1&spLa=ZW5jcnlwdGVkUXVhbGlmaWVyPUExRUpKS0gzOFVTOTBEJmVuY3J5cHRlZElkPUEwMjc2ODk5MUszVzIxM0sxSEU0MSZlbmNyeXB0ZWRBZElkPUEwMjUzNzQ5MkhSSFA0TFZYQlZKUSZ3aWRnZXROYW1lPXNwX2F0ZiZhY3Rpb249Y2xpY2tSZWRpcmVjdCZkb05vdExvZ0NsaWNrPXRydWU=], 15 March 2021.

59. Getfpv, "Dragon Link Advanced 915 MHz 1000 mW Radio Modem Reciever," *Getfpv.com*, [https://www.getfpv.com/dragon-link-advanced-915-mhz-1000-mw-radio-modem-receiver.html], 15 March 2021.
60. Andraši, P., Ivošević, J., Muštra, M., Radišić, T., "Night-Time Detection of UAVs Using Thermal Infrared Camera," *University of Zagreb Faculty of Transport and Traffic Sciences*, [https://www.sciencedirect.com/science/article/pii/S2352146517311043], 19 February 6:00 pm.
61. Barrett, Ronald., "AE 522 HFBWEB Lecture 3-8-2021," University of Kansas, 2021.
62. Barrett, R. M., "AE522_HFB_Web_4_28_21," The University of Kansas Aerospace Engineering Department, 9:00 am – 10:30 am, 7 April 2021.
63. Park, D., "Resistance Man,", *artstation.com*, [https://www.artstation.com/artwork/QZwlZ], 22 March 2021.
64. Park, D., "Girl,", *artstation.com*, [https://dohyun.artstation.com/projects/D1PVR], 22 March 2021.
65. Brelje, Ben., "Deriving the Modified Breguet Range Equation For a Hybrid-Turboelectric Aircraft," [https://brelje.net/blog/deriving-modified-breguet-range-equation-hybrid-turboelectric-aircraft/], 17 September 2017.
66. Inspire 2 - product information - dji. (n.d.). Retrieved February 28, 2021, from https://www.dji.com/inspire-2/info#specs.
67. Matrice 600 Pro - product information - DJI. (n.d.). Retrieved February 28, 2021, from https://www.dji.com/matrice600-pro/info#specs.
68. Roskam, Jan. *Airplane Flight Dynamics and Automatic Flight Controls*. DARcorporation, 2018, Lawrence, KS.
69. Arnold, Emily, "Material Properties Table," The University of Kansas Aerospace Engineering Department, 1 October 2020.

70. Liang, Oscar., "The Different Frequencies For FPV," [https://oscarliang.com/fpv-frequency/], 21 March 2021.

71. Egun, Agun., "Predator MQ-1B," GrabCad.com, [predator MQ - 1B | 3D CAD Model Library | GrabCAD], 19 April 2021.

72. Williamson, Grant., "DJI Phantom Drone (custom)," GrabCad.com, [https://grabcad.com/library/dji-phantom-drone-custom-1], 21 January 2020.

73. Barrett, R. M., "XQ-138_RedstoneFlying3J," The University of Kansas Aerospace Engineering, 28 April 2021.

74. Barrett, R. M., "XQ-138_Short_Movie_9_12a," The University of Kansas Aerospace Engineering, 28 April 2021.

75. Maintenance and Engineering. (2018, February 13). "Lifecycle Cost Analysis," Retrieved February 15, 2021, [https://www.maintenanceandengineering.com/2018/02/13/lifecycle-cost-analysis/].